Vibrations in C_{60} and Amorphous Silicon

A Dissertation Presented

by

Jaroslav Fabian

to

The Graduate School

in Partial Fulfillment of the Requirements

for the Degree of

Doctor of Philosophy

in

Physics

State University of New York
at
Stony Brook

August 1997

State University of New York
at Stony Brook

The Graduate School

Jaroslav Fabian

We, the dissertation committee for the above candidate for the Doctor of Philosophy degree, hereby recommend acceptance of the dissertation.

Philip B. Allen,
Professor, Department of Physics and Astronomy, Stony Brook

Jainendra K. Jain,
Professor, Department of Physics and Astronomy, Stony Brook

Laszlo Mihaly,
Professor, Department of Physics and Astronomy, Stony Brook

Donald J. Weidner,
Professor, Mineral Physics Institute, Stony Brook

This dissertation is accepted by the Graduate School.

Graduate School

Abstract of the Dissertation
Vibrations in C_{60} and Amorphous Silicon

by

Jaroslav Fabian

Doctor of Philosophy

in

Physics

State University of New York at Stony Brook

1997

This Dissertation reports on theoretical studies of vibrational properties of C_{60} and amorphous silicon. When molecules C_{60} form a solid, their infrared spectrum displays many weak vibrational modes. Among possible activation mechanisms for these modes are ^{13}C isotopic impurities and anharmonicity. By performing a Monte Carlo simulation and comparing its results with experiment, the isotopic activation mechanism is excluded. Anharmonicity can activate combination (with frequencies ω equal to $\omega_i + \omega_j$, the sum of two fundamental frequencies ω_i, ω_j) and difference (with $\omega = \omega_i - \omega_j$) vibrational modes through either anharmonic interatomic forces (mechanical anharmonicity) or a nonlinear dipole-moment

expansion in normal mode coordinates (electrical anharmonicity). By modeling both types of anharmonicity it is shown that the majority of the experimentally seen weak modes are caused by electrical anharmonicity only.

Vibrational modes in amorphous silicon are studied by using a realistic semiempirical model with 216 and 1000 silicon atoms interacting via the Stillinger-Weber potential. In contrast to a recent experiment and previous theoretical views, it is shown that the vibrational modes decay on picosecond time scales and their decay rates increase with increasing frequency. According to the fracton model the interactions between three localized modes do not play any role in the decay of localized modes. Simple scaling arguments and a numerical realization of the fracton model as a one-dimensional random-spring atomic chain prove that the interaction between three localized modes is, in fact, the most relevant interaction for the decay of high-frequency localized modes in glasses with low mobility edge. Finally, the mode Grüneisen parameters γ and temperature dependent coefficient of linear thermal expansion $\alpha(T)$ are calculated. The resulting values of γ differ from the crystalline case in having all diversity suppressed, except for a minority of high-frequency localized and low-frequency resonant modes. The latter have very large, mostly negative γ (up to -30), caused by volume driven internal strain.

To Janka

Contents

[1] M. C. Martin, J. Fabian, J. Godard, P. Bernier, J. M. Lambert, L. Mihaly, Phys. Rev. B **51**, 2844 (1995); J. Fabian, Phys. Rev. B **53**, 13 864 (1996).

[2] J. Fabian and P. B. Allen, Phys. Rev. Lett. **77**, 3839 (1996).

[3] J. Fabian, Phys. Rev. B **55**, R3328 (1997).

[4] J. Fabian and P. B. Allen, Phy. Rev. Lett. (in press)

[5] J. Fabian and J. L. Feldman (unpublished).

[6] J. Fabian and J. L. Feldman (unpublished).

[7] J. Fabian and P. B. Allen (unpublished).

List of Figures

List of Tables

Preface

This Dissertation is a summary of the research I have done as a graduate student in SUNY at Stony Brook (1993-97) with my advisor Philip Allen. The Dissertation has two chapters which deal with vibrations in molecular and solid-state systems. More specifically, the concept of anharmonicity (or interaction between fundamental vibrational modes) is exploited to yield various observable properties of the molecule C_{60} and amorphous silicon.

Chapter 1 is devoted to our theory of the infrared spectrum of C_{60}. This project started in 1994 with the goal to explain what Michael Martin and Laszlo Mihaly observed: a plenitude of weak features in the infrared spectrum of a single-crystal C_{60}. These features were puzzling at the time (section 1.1 explains why). We had to develop several models before it became clear what is the origin of the observed spectrum. In Sec. 1.2 I show how a combination of experimenting and numerical modeling ruled out the isotope effect as a possible activation mechanism for the weak features. (The isotopic symmetry breaking was then the most popular hypothesis for the weak features.) Anharmonicity came next. First we tried anharmonic forces between carbon atoms (Sec. 1.3). Unsuccessfully. The resulting theoretical spectrum was much weaker than the

experimental one. Eventually we developed an anharmonicity model in which light couples directly to two vibrational modes (Sec. 1.4). This mechanism turned out to be the right one: the model spectrum has almost all the features seen experimentally.

Chapter 2 is concerned primarily with the vibrations in amorphous silicon (though many of the conclusions of this part are valid for glasses in general). Theory of glasses is not yet developed and we have to rely on computer simulations to get an insight into the physics of these structurally complex materials. The work presented here started in 1995 and is a natural extension of the work of Allen and Feldman on diffusive vibrational transport of energy in glasses. Section 2.2 is an introduction to the subject. The model is described and the properties of its vibrational eigenstates are discussed in harmonic approximation. Experiments by Scholten and Dijkhuis indicated that vibrational relaxation in amorphous silicon is much smaller than in crystalline silicon. This was not surprising for the fracton model. Using a few reasonably sounded assumptions, this analytically tractable model was able to fit the experimental curves. We took a different approach: using a realistic computer-generated model of amorphous silicon we calculated the vibrational decay rates numerically. The method and results of our calculation are described in Sec. 2.3. Our numerical results showed that the experiment was misinterpreted. Moreover, simple scaling arguments and a one-dimensional example of the fracton model in Sec. 2.4, show that a very important premise of the fracton model (the negligibility of the interactions involving three localized modes) is wrong. In effect, almost all the conclusions of the fracton model regarding transport are incorrect.

Thermal expansion of glasses is a topic of enormous practical importance. Experiments at low temperatures showed that the standard "tunneling" model (STM) of Anderson, Halperin, Varma, and Phillips, has to be revised. Several schemes going beyond the STM model have been devised to explain the experimental results. In Sec. 2.5 I report on the first realistic calculation of thermal expansion and Grüneisen parameters in a glass—amorphous silicon. Many interesting properties of vibrational modes (e.g., global indistinguishability) have been revealed by this calculation. In addition, section 2.5 proposes a likely explanation of the observed low-temperature behavior of the thermal expansion and Grüneisen parameters in glasses.

Chapter 2 is concluded with a brief account of unfinished work ("work in progress"). Many questions in the physics of glasses are open (the liquid-to-glass transition being, perhaps, the most prominent one). The choice of the topics in Sec. 2.6 therefore reflects our curiosity rather than anything else. For example, the connection between random matrix theory and diffusons seems to be purely academical (although it may initiate creation of an analytical model for the vibrations in glasses). On the other hand, our treatment of internal friction and sound attenuation in glasses may have practical applications.

Bibliography is included after each chapter.

To conclude the preface I wish to thank my collaborators and friends. My gratitude goes first to Phil Allen who has patiently guided me through complexities of physics research since I came to Stony Brook. Perhaps the most valuable lesson I have learned from Phil is that theoretical considerations should be closely related to experiment (past or future). Laszlo Mihaly and

Michael Martin helped me to understand the physics of buckyballs through our conversations in their lab where many discoveries in this field were made. Joe Feldman shared with us various models of amorphous silicon. Together with Scott Bickham, Joe is thanked for many inspiring discussions and collaboration (and also for his hospitality during my stay in the Naval Research Laboratory). I am also grateful to Herbert Schober for sharing his views on the physics of glasses and for his hospitality during my stay in Jülich. In my first years in Stony Brook I was fortunate to discuss various aspects of many-body physics with Jainendra Jain; the conversations have continued sporadically in the later years too. Finally, the following is a list (in alphabetical order) of my friends that have made my stay in Stony Brook enjoyable: Thanos Bardas, Adam Halasz, Rajiv Kamilla, Vladimir Kostur, Chinmong Leung, Ilary Maasilta, Guilherme Nunes, Alexander Rylyakov, Werner Schulz, and Kevin Wu.

List of Publications

[1] J. Fabian, *Ground-State Energy of the Hubbard Model in the BCS approximation*, Czechoslovak Journal of Physics **43**, 1136 (1993).

[2] J. Fabian, *High Temperature Effects in the Hubbard Model*, International Journal of Modern Physics B **8**, 1065 (1994).

[3] J. Fabian, *Optical Conductivity of the Hubbard Model in the Strong Coupling Regime*, Physics Letters A **186**, 269 (1994).

[4] M. C. Martin, J. Fabian, J. Godard, P. Bernier, J. M. Lambert, and L. Mihaly, *Vibrational Study of ^{13}C-Enriched C_{60} Crystals*, Physical Review B **51**, 2844 (1995).

[5] J. Fabian, *Theoretical Investigation of C_{60} IR Spectrum*, Physical Review B **53**, 13 864 (1996).

[6] J. Fabian and P. B. Allen, *Anharmonic Decay of Vibrational States in Amorphous Silicon*, Physical Review Letters **77**, 3839 (1996).

[7] J. Fabian, *Decay of Localized Vibrational States in Glasses: A One-Dimensional Example*, Physical Review B **55**, R3328 (1997).

[8] J. Fabian and P. B. Allen, *Thermal Expansion and Grüneisen Parameters of Amorphous Silicon: A Realistic Model Calculation*, to appear in Physical Review Letters **79** (1997).

Chapter 1

Theory of the Infrared Spectrum of C_{60} [1]

1.1 Introduction

There has been a great deal of progress in revealing chemical and physical properties of fullerenes. Much of the discussion on the subject was ignited by the discovery of superconductivity in alkali-metal-doped C_{60} [1]. It seems that the current understanding is that superconductivity in these materials is caused by a coupling between electrons and intra-molecular vibrations [2]. (For a competing model stressing strong electron-electron correlations, see Ref. [3].) The intra-molecular vibrations in fullerenes are the subject of this chapter. But rather than their coupling to conduction electrons, we will consider their interaction with light. This interaction is experimentally accessible by Raman and infrared (IR) spectroscopy [4, 5, 6, 7, 8, 9, 10].

The icosahedral (I_h) symmetry of C_{60} allows 46 distinct vibrational modes,

[1] M. C. Martin, J. Fabian, J. Godard, P. Bernier, J. M. Lambert, L. Mihaly, Phys. Rev. B **51**, 2844 (1995); J. Fabian, Phys. Rev. B **53**, 13 864 (1996).

out of which four are IR active (T_{1u}) and ten are Raman active ($2A_g \bigoplus 8H_g$). It is customary to denote the triply-degenerate IR modes at frequencies 527, 576, 1182, and 1427 cm^{-1}, as $T_{1u}(i)$, i=1,2,3,and 4, respectively. 32 optically inactive (silent) modes are $1A_u, 3T_{1g}, 4T_{2g}, 5T_{2u}, 6G_g, 6G_u$, and $7H_u$. Higher-order modes can be seen experimentally by increasing the optical depth of a sample. In principle there are 380 second-order combination modes IR allowed by the I_h symmetry [8]. Second-order overtones are IR forbidden.

Several authors reported observation of weak modes in Raman [10, 11] and IR [7, 8, 9, 12] spectroscopy. Wang *et al.* [7], Martin *et al.* [8], and Kamarás *et al.* [9] analyzed the weakly active features in conjunction with Raman [10] and neutron measurements [13] to extract the 32 fundamental frequencies of the silent modes. The frequencies differ significantly among the authors, leaving the question of the assignment of fundamentals open.

Possible mechanisms of activating the weak modes include crystal field effects, ^{13}C isotopic impurities, and anharmonicity. Impurities, dislocations and electric field gradients at surface boundaries can be excluded due to their sample dependence. It is believed that the fcc crystal field activates a few of the weak modes. The crystal field reduces the I_h symmetry of C_{60} and activates some of the silent modes. However, above 260 K the C_{60} molecules freely rotate and the time-averaged crystal field perturbation is zero. As a result, the silent modes should disappear. This was indeed experimentally observed by Mihaly and Martin [14] (and appropriately named "motional diminishing").

The isotope effect is examined in Sec. 1.2. This effect is based on the fact that not all the carbon atoms that form the molecule C_{60} are isotopes ^{12}C;

about 1% of carbon atoms found in nature are isotopes ^{13}C. A small mass difference between the two isotopes breaks the I_h symmetry and makes all the vibrational modes of C_{60} infrared active. How can one decide whether this mechanism is present in the observed spectrum? Martin *et al.* [15] compared the infrared spectra of a C_{60} sample with 8% of ^{13}C present, and a sample with the natural abundance ($\sim$ 1%) of ^{13}C. Except for a trivial broadening and softening of the transmission peaks, the spectra were identical! In Sec. 1.2 we show that if the silent modes were activated through isotopic symmetry breaking, the IR intensity of these modes in the 8%-enriched sample would be (on average) at least 4 times greater than that in the natural abundance sample. In the calculation we use the bond-charge model of Sanguinetti *et al.* [16] and known intensities of the four IR-allowed modes. The enrichment of the sample by either 1 or 8% is modeled in a Monte Carlo cycle. The comparison of our calculation with experiment shows that the isotope effect is not the cause for the weak active IR modes.

In the remaining sections we study the effect of anharmonicity in the IR spectrum of C_{60}. (General formalism of anharmonic effects on IR activity is given in [17, 18, 19, 20, 21, 22].) There are two ways in which anharmonicity can display itself in an optical spectrum. It is driven either by anharmonic interatomic forces (mechanical anharmonicity) or by an anharmonic coupling of a photon field to two or more vibrational modes (electrical anharmonicity). Although the two mechanisms are not independent, each has its own characteristic absorption intensity pattern. When compared with an experimental spectrum one can decide which of the two kinds of anharmonicity prevails in

the IR spectrum of C_{60}. Although the spectrum may contain cross contributions from both phenomena, here they are treated separately.

Several models have been used to calculate absorption intensities in harmonic approximation. Tight-binding models [23, 24] are in complete disagreement with the experimental results. The bond-charge model [16] fits very well with frequency positions of fundamentals but the IR intensity pattern disagrees with basic trends in the observed spectrum. The same is true for a Hubbard-type model stressing electronic correlation effects [25]. Relative intensities are best reproduced by the local density approximation (LDA) [24, 26]. However, due to its computational complexity, the LDA scheme is not convenient for computing second order intensities. We therefore propose a semiempirical model which is satisfactory for a qualitative comparison with experiment. Figure 1.1 summarizes the performance of various models in calculating the absorption intensities.

Some characteristics of the experimental IR spectrum [8] are shown in Fig. 1.2. Combination (difference) modes are higher-order modes with frequency ω equal to $\omega_i \pm \omega_j$, the sum (difference) of fundamental frequencies ω_i. Their intensities are temperature dependent according to $(n_i+\frac{1}{2})\pm(n_j+\frac{1}{2})$, where n_i is the Bose factor, $n_i + \frac{1}{2} = \frac{1}{2}\coth(\hbar\omega_i/2k_BT)$, with a temperature T and the Boltzmann constant k_B. The following features can be observed in the spectra: (i) besides four first-order peaks (at 527, 575, 1182, and 1427 cm^{-1}), there are more than 180 weak absorptions; (ii) no difference peaks are resolved (i.e., no temperature dependence of intensities except a trivial improvement in the frequency resolution at lower temperatures); (iii) most of the spectral weight is

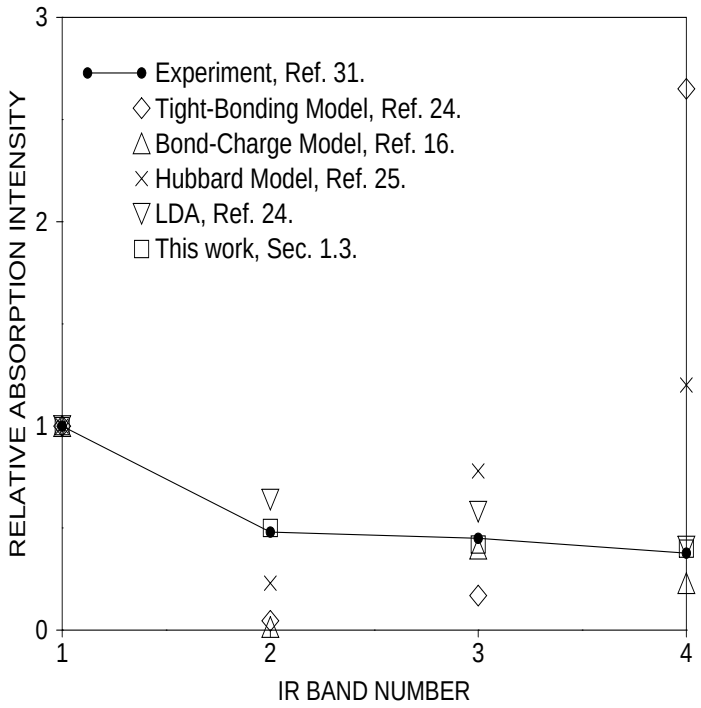

Figure 1.1: Comparison of calculated relative absorption intensities of IR-allowed $T_{1u}(i)$, i=1, 2, 3, and 4, modes with experiment. Intensities of the band $T_{1u}(1)$ are taken to be unity.

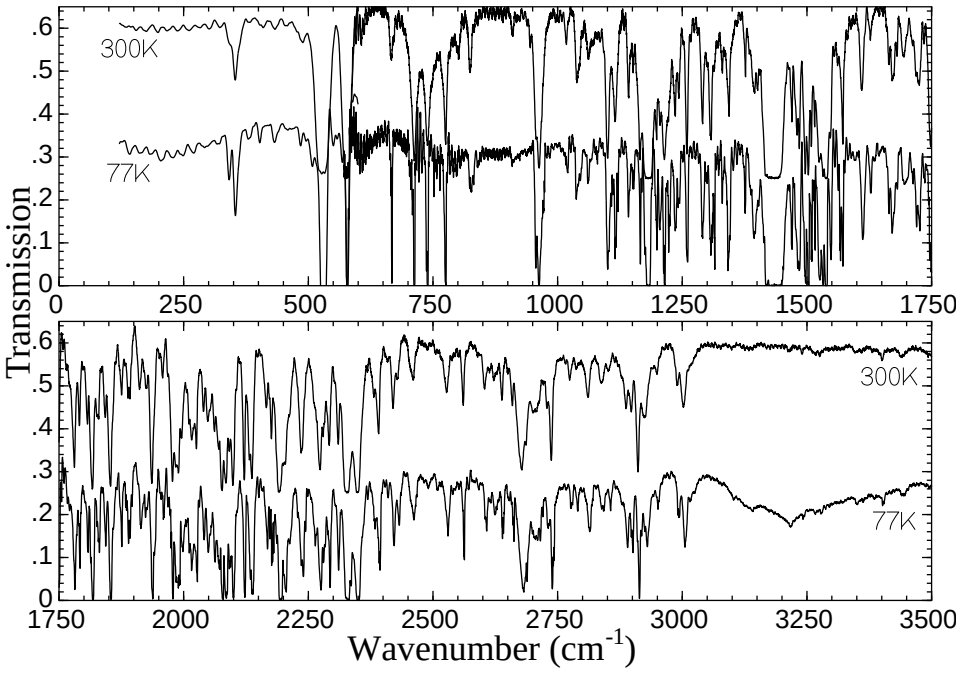

Figure 1.2: C_{60} single-crystal IR transmission spectra at 300 and 77 K by M. Martin *et al.* [8].

in the high-frequency regime (1000 - 3000 cm^{-1}); and (iv) weak modes around four first-order bands are not enhanced through a resonance effect.

We treat the frequency positions and absorption intensities independently. Normal modes and frequencies are calculated using a simple force-constant model proposed by Weeks [27]. This model fits IR data reasonably well but is not expected to give especially realistic eigenfrequencies for the silent modes. The dipole moment which arises due to the coupling between electrons and vibrational modes, determines the absorption intensities [28]. Only second-order combination and difference modes are considered. Section 1.3 deals with the mechanical anharmonicity problem with the Morse function used for the interatomic bond-stretching potential [27]. A linear relation between the dipole moment and ionic coordinates is proposed in this section. The relation contains parameters fittable to the relative harmonic absorption intensities. Second-order modes are computed using a perturbation method ignoring possible resonances. We find that the intensity pattern of the second-order modes fails to reproduce experimental features. An electrical anharmonicity model is therefore introduced in Sec. 1.4. Normal frequencies and normal modes are again taken to be those of the Weeks model. A semiempirical model for an electronic configuration on a distorted C_{60} is presented, which allows the electronic coordinates to depend in a nonlinear fashion on positions of ions. This gives rise to an intensity pattern very similar to the experimental one. Finally, conclusions are drawn in Sec. 1.5.

1.2 The Isotope Effect

This section examines the role of isotopic symmetry breaking in the activation of the weak modes seen in the C_{60} IR spectrum. Several works [7, 8, 9] argued that ^{13}C isotope substitution is a likely agent for activating silent modes since for the natural abundance of ^{13}C, about one-half of all C_{60} molecules would have at least one ^{13}C which would break the I_h symmetry and activate all the vibrational modes. One way to decide whether the isotope effect activates the weak modes, is to compare the spectra of samples with different isotopic substitutions: the more ^{13}C-enriched the sample is, the more intense the weak modes should be. Martin *et al.* [15] measured the IR spectrum of 8% ^{13}C-enriched C_{60} crystals. Figure 1.3 presents the data.

The uppermost curve is the transmission of a natural abundance C_{60} single crystal. The four IR-active T_{1u} vibrational modes are observed to be completely saturated around their known positions of 527, 576, 1182, and 1427 cm^{-1}. All other observed absorptions are due to IR-forbidden fundamental vibrations or second- (or higher-) order modes. The middle curve of Fig. 1.3 displays the IR spectrum of an 8% ^{13}C-enriched C_{60} crystal. When comparing this spectrum with that of the natural abundance crystal (top curve of Fig. 1.3), the primary changes observed are that all of the visible modes have broadened and slightly softened. However, the relative intensities of the weakly active modes do not change significantly. Nearly all the features of the transmission spectrum of the 8% enriched sample can be modeled by simply broadening the spectrum obtained for the natural abundance crystal assuming

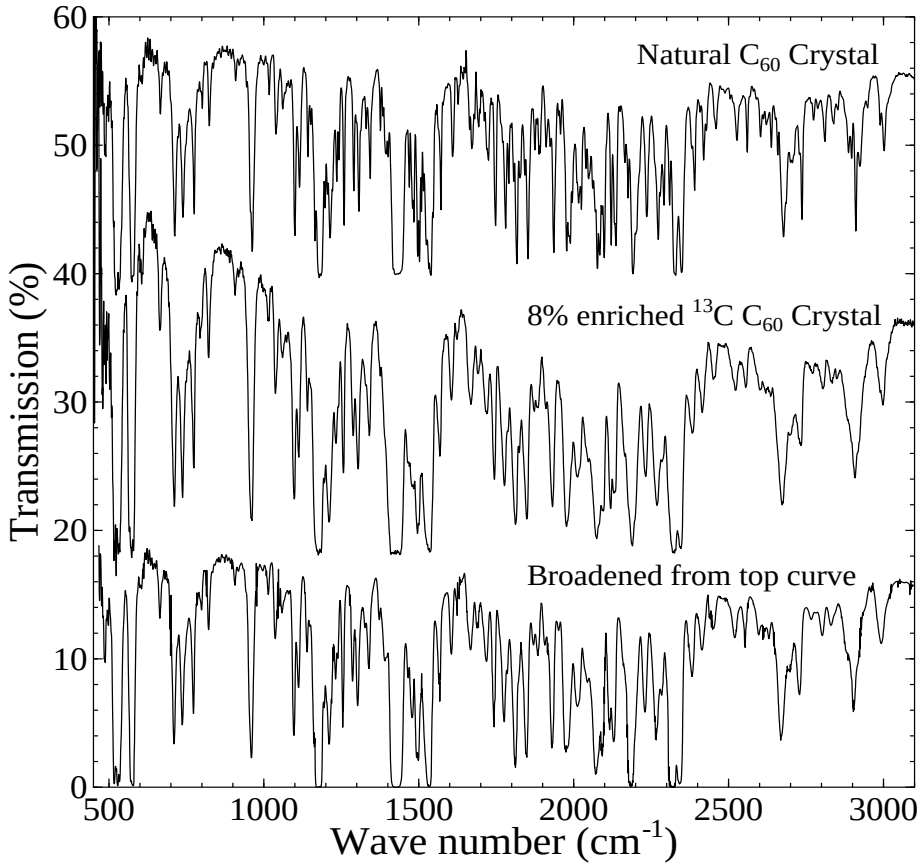

Figure 1.3: Infrared spectra of C_{60} single crystals [15]; the two upper curves have been vertically offset for clarity. The top spectrum is for a crystal made from natural abundance ^{13}C C_{60}. The middle curve is the spectrum of an 8% ^{13}C-enriched C_{60} crystal. The bottom curve is generated from the top curve using a simple model of frequency shift and the mass distribution representing the 8% enrichment.

the vibrational frequency is proportional to $1/\sqrt{m}$, m being the isotope mass. The bottom curve of Fig. 1.3 is obtained by this method. A careful comparison of the measured 8%-enriched spectrum and the spectrum generated from the broadening reveals that they are indeed very well matched, indicating that ^{13}C substitutions change the frequency of the mode, but do not influence the intensity.

If the fundamental modes are being activated by symmetry breaking due to isotopic substitutions, one would expect the ^{13}C-enriched samples to have greater symmetry breaking, and therefore greater IR activity for originally silent modes. To demonstrate this, we used a theoretical model of C_{60} based on the bond-charge model of Onida and Benedek [29] (the only change was to use the better experimental values [30] of 1.4 Å for the hexagon-hexagon bond length and 1.45 Å for the pentagon-hexagon bond-length). The vibrational frequencies calculated with this model are within 3% of the experimental IR and Raman mode frequencies.

The calculation of the IR intensity of a given mode requires, in principle, the knowledge of the electronic eigenstates of the deformed molecule. To avoid the numerical complexity of such an approach we used an approximate procedure, based on the experimentally known IR intensities of the four allowed T_{1u} modes and on the calculated vibrational eigenvectors of the isotopically changed molecule. When expanded in terms of the original eigenvectors of the pure ^{12}C C_{60} molecule, some or all of the new eigenvectors had components in the directions of the original T_{1u} eigenvectors. Each degenerate species of the unperturbed T_{1u} eigenvectors are chosen to carry their dipole moments in the

Cartesian x, y, and z directions. The intensity of each of the four IR-active T_{1u} modes was then taken from experiment [31] and are denoted A_1, A_2, A_3, and A_4. The IR intensity of mode l is then calculated using

$$I_l = \sum_{i=1}^{3} \left(\sum_{j=1}^{4} \sqrt{A_j} \tilde{Q}_{jl}^{i} \right)^2 , \tag{1.1}$$

where $\tilde{Q}_{jl}^{i}$ is the component of eigenmode l in the direction of the ith degenerate mode of the original $T_{1u}(j)$ eigenvector; i sums over the triple degeneracies and j sums over the four T_{1u} modes. The isotopic content is modeled by a Monte Carlo simulation: each of the 60 carbon atoms is given a ^{13}C or a ^{12}C mass with appropriate probabilities representing the natural abundance or ^{13}C enrichment (1.108% and 8% ^{13}C, respectively). The dynamical matrix for the resultant molecule was then diagonalized to calculate the eigenvectors, and Eq. 1.1 was applied . For a given isotope concentration, this process is repeated until a general sampling of all possible ^{13}C configurations is calculated and the results are averaged together. For the natural abundance case, there are relatively few possible configurations, but for the 8% ^{13}C-enriched case, there are a huge number of configurations. We sampled over 15,000 possible configurations for the 8% case, which should suffice to obtain the correct trends.

We plot the resultant calculated IR intensity for 1.108% and 8% ^{13}C C_{60} molecules in Fig. 1.4. The Lorentzian widths of all modes have been taken to be uniformly 3 cm^{-1}. The four T_{1u} modes in Fig. 1.4 have peak heights of approximately 2000, so the intensities of the weakly activated modes are approximately a factor of 10^4 smaller. This is in contrast to the experimentally

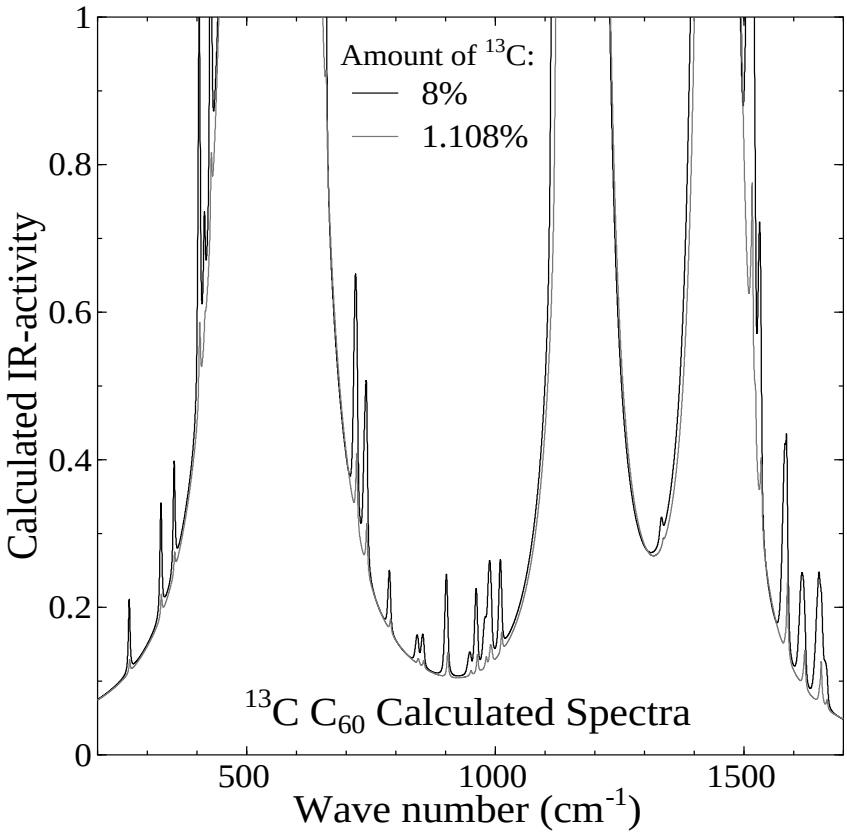

Figure 1.4: Calculated IR intensities of vibrational modes in C_{60} with 1.108% and 8% isotopic substitution. The four IR-active T_{1u} modes have intensities of ~ 2000 which are well off scale; the scale is chosen so that the weakly activated symmetry-forbidden modes can be seen.

observed intensity ratio of only a factor of ~ 10. Furthermore, the average intensity of the weakly activated modes increases by a factor of 4.45 in the 8% enriched calculation compared to the natural abundance calculation, but no similar increase was seen in the experiment.

We must therefore conclude that isotopic activation of previously silent modes is not the symmetry-breaking mechanism in C_{60}.

1.3 Mechanical Anharmonicity Model

Considering the C_{60} molecule as a system of oscillating ions with electrons moving adiabatically in their field, the ionic dynamics is governed by the following potential:

$$V = \frac{1}{2}\sum_{i=1}^{46}\sum_{q=1}^{g_i} m{\omega_i}^2 Q_{iq}^2 + \frac{1}{6}\sum_{i,j,k=1}^{46}\sum_{q,r,s=1}^{g_i,g_j,g_k} C_{iq,jr,ks} Q_{iq} Q_{jr} Q_{ks}. \tag{1.2}$$

Here m is the ion mass, Q_{iq} is the qth normal mode coordinate belonging to the frequency ω_i, i=1,..,46, q=1,..,g_i, and g_i is the degeneracy of the ith band. Higher-order terms are neglected. The anharmonicity coefficients $C_{iq,jr,ks}$ are given by

$$C_{iq,jr,ks} = \frac{\partial^3 V}{\partial Q_{iq}\partial Q_{jr}\partial Q_{ks}} \tag{1.3}$$

with the derivatives taken at $Q = 0$. Light couples to the system via the term

$$V_1 = -\mu(Q)\cdot\ \mathbf{E}, \tag{1.4}$$

where $\mathbf{E}$ is the externally applied electric field and μ stands for the dipole moment of the system. The latter is generally a nonlinear function of normal

coordinates

$$\mu = \sum_{i=1}^{46} \sum_{q=1}^{g_i} \mathbf{M}_{iq} Q_{iq} + \frac{1}{2} \sum_{j,k=1}^{46} \sum_{r,s=1}^{g_j,g_k} \mathbf{M}_{jr,ks} Q_{jr} Q_{ks}. \tag{1.5}$$

Again, higher-order terms are not included and the following formulas determine the expansion parameters $\mathbf{M}_{iq}$ and $\mathbf{M}_{jr,ks}$:

$$\mathbf{M}_{iq} = \frac{\partial \mu}{\partial Q_{iq}}, \tag{1.6}$$

and

$$\mathbf{M}_{jr,ks} = \frac{\partial^2 \mu}{\partial Q_{jr} \partial Q_{ks}}. \tag{1.7}$$

The vectors $\mathbf{M}_{iq}$ are nonzero only when the Q_{iq} mode is IR allowed.

Anharmonic dynamics ($C_{iq,jr,ks} \neq 0$) and a linear coupling of light to vibrational modes ($\mathbf{M}_{kr,ls} = 0$) characterize the mechanical anharmonicity (MA) phenomenon.

Several force-constant models for C_{60} have been presented [27, 32, 33]. To calculate normal coordinates and the anharmonicity coefficients $C_{iq,jr,ks}$, we use the model suggested by Weeks [27], which is a refined model of Weeks and Harter [34]. This model contains two parameters which were fitted to selected IR and Raman frequencies. Ionic dynamics is governed by two types of interactions: (i) the Morse potential producing anharmonic terms

$$V_m = \sum_{i=1}^{90} D\{1 - \exp[-\alpha(r_i - r_{eq})]\}^2, \tag{1.8}$$

controls bond stretching. Here D, α, r_{eq}, and r_i are, respectively, the dissociation energy, Morse anharmonicity, equilibrium and instantaneous length of the ith bond. Summation runs over all bonds. The dissociation energy is

estimated as the average of the dissociation energies of a single and a double C_2 bond, $D = 5.0$ eV, the equilibrium length is taken to be 1.4 Å, and the parameter α was fitted to the value 1.6 Å^{-1}. (ii) The bond-bending harmonic potential is given by

$$V_b = \sum_j \eta(\theta_{eq} - \theta_j)^2, \tag{1.9}$$

where the summation is over the 60 pentagonal angles with the equilibrium angle of $3\pi/5$ and the 120 hexagonal angles with the equilibrium angle of $2\pi/3$. The potential does not distinguish between hexagonal and pentagonal angles and the best fit yields $\eta = 12.48$ eV/rad.

The bond-stretching potential in the harmonic approximation together with the bond-bending potential give normal coordinates and frequencies. The coefficients $C_{iq,jr,ks}$ come from the expansion of the Morse function to the third order in ionic distortions from equilibrium and from the transformation of the Cartesian coordinates to the normal mode ones computed numerically. Qualitative behavior of the normal modes of the model (with the bond-stretching potential in the harmonic approximation) is discussed in the original papers [27, 34]. Here it suffices to note that lower-frequency normal modes exhibit mostly radial distortions while the motion of higher-frequency ones is tangential.

The IR intensity of a given mode is proportional to the square of a dipole moment associated with this mode. If ionic charges of the same value were put on the vertices of C_{60}, the resulting dipole moment would be zero due to the center-of-mass conservation. The dipole activity is therefore caused by

changes in the electronic configuration.

Carbon valence electrons fall into two classes. The first class consists of σ electrons positioned with the highest probability in the middle of bonds. These electrons have fixed charges and do not contribute to the dipole moment (due to the center-of-mass conservation). In the following the notion of a bond charge will include also a contribution from ions in some effective way. The sign of such an effective bond charge will not be important; it can be either positive or negative. Allowing the bond charges to acquire a charge with dependence on the bond lengths or by some other mechanism leads to a spectrum where the $T_{1u}(2)$ mode is hardly visible instead of having the second largest activity [16, 35].

The second class consists of π electrons, which can be considered as vertex electrons moving in the field of their parent ions. Let these electrons interact further only with the three nearest ions. We model the positions of the π electrons in the following way. Let $\mathbf{r}_i$ denote the radius vector of the ith electron measured from the vertex i with the position $\mathbf{R}_i$. $\mathbf{R}_i$ and $\mathbf{R}_j^{(i)}$, $j = 1, 2, 3$, the nearest ions positions, are relative to the center of C_{60}. The direction of $\mathbf{r}_i$ is taken to be the direction of the normal vector $\mathbf{n}_i$ to the plane given by three nearest ions with a rescaled position of the one making the double bond with the vertex. This condition,

$$\mathbf{n}_i \cdot (\mathbf{R}_1^{(i)} - \mathbf{R}_2^{(i)}) = \mathbf{n}_i \cdot (\mathbf{R}_1^{(i)} - c_1 \mathbf{R}_3^{(i)}) = 0, \tag{1.10}$$

introduces a fitting parameter c_1, effectively measuring the ratio of the double- and single-bond charge (here the bond $\mathbf{R}_i - \mathbf{R}_3^{(i)}$ is the double one). Single

bonds are bonds connecting a hexagon with a pentagon and double bonds are connecting two hexagons. When there is more charge on the double bond than on the single one, the parameter c_1 is greater than unity. If the bond charge is negative, the direction is out of the sphere and if it is positive, the direction is inwards.

Consider the distance d of the vertex ion to the plane given by its three nearest ionic neighbors (with the double bond neighbor rescaled as explained above). Denote as d_{eq} the distance for the equilibrium configuration. Let, for a moment, the effective bond charge be negative. If a distortion of the ionic positions occurs such that $d > d_{eq}$ the vertex electron will be pushed "out" of the C_{60} sphere and vice versa. If the net bond charge is positive, the situation is inverse. This phenomenology reflects a Coulomb repulsion (attraction) of the vertex electron by (to) adjacent bonds. When these bonds move closer together the vertex electronic cloud is deformed such that the mean electronic position will be as far (close) as possible from (to) the bonds. The effective rate of the deformation will be the second free parameter c_2 (the same for each vertex due to symmetry). The relation between the electronic position and the distance between the vertex ion and the plane given by its nearest neighbors can then be expressed as follows :

$$\mathbf{r}_i = \{1 + c_2[d_i(c_1) - d_{eq}(c_1)]\}\mathbf{n}_i(c_1), \tag{1.11}$$

where the dependence on the parameter c_1 is indicated. The dipole moment is then

$$\mu = \sum_{i=1}^{60}[1 + c_2(d_i - d_{eq})]\mathbf{n}_i. \tag{1.12}$$

The normalization in both formulas is not important for calculating relative values. The distances d_i depend for small distortions linearly on normal coordinates, so only the linear term is kept here because the mechanical anharmonicity couples this linear displacement to two normal modes.

There are two parameters in this model, c_1 and c_2. In the harmonic approximation the intensity of the jth mode is [28]

$$I_{\omega_j}^{(1)} = \sum_{q=1}^{g_j} \mathbf{M}_{jq}^2. \tag{1.13}$$

Experimentally obtained relative intensities are 1., 0.48, 0.45, and 0.378 for the modes $T_{1u}(1)$, $T_{1u}(2)$, $T_{1u}(3)$, and $T_{1u}(4)$, respectively [31]. The best fit to these intensities yields the values $c_1 = 1.59$ and c_2=0.67 Å^{-1}. The IR spectrum obtained with this fit (all peaks in this and following figures have the Lorentzian widths taken to be uniformly 2 cm^{-1}) along with an experimental one is shown in Fig. 1.5. Agreement is excellent.

For the frequencies that are not in the immediate neighborhood of the frequencies of the four IR-allowed fundamentals, the following formulas were obtained by Szigetti [19] for the second-order intensities of combination and difference modes:

$$I_{\omega_k+\omega_l}^{MA} = \frac{\hbar}{2m^3}\frac{\omega_k+\omega_l}{\omega_k\omega_l}(1+n_k+n_l)\sum_{r,s=1}^{g_k,g_l}\left(\sum_{j\in IR}\frac{\langle \mathbf{M}_j|C_{j,kr,ls}\rangle}{{\omega_j}^2-(\omega_k+\omega_l)^2}\right)^2, \tag{1.14}$$

and

$$I_{\omega_l-\omega_k}^{MA} = \frac{\hbar}{2m^3}\frac{\omega_l-\omega_k}{\omega_k\omega_l}(n_k-n_l)\sum_{r,s=1}^{g_k,g_l}\left(\sum_{j\in IR}\frac{\langle \mathbf{M}_j|C_{j,kr,ls}\rangle}{\omega_j^2-(\omega_l-\omega_k)^2}\right)^2, \tag{1.15}$$

respectively. The summation in brackets is over four IR-active bands and the

Figure 1.5: First-order IR-allowed intensities calculated in Sec. III and experimentally obtained spectrum (inset) by Hare *et al.* [6].

inner-product notation stands for the sum over a degenerate set:

$$\langle \mathbf{M}_j | C_{j,..} \rangle \equiv \sum_{q=1}^{g_j} \mathbf{M}_{jq} C_{jq,..}. \tag{1.16}$$

When the frequency of a combination (difference) mode is near the frequency of an IR-allowed mode (the Fermi resonance effect), a perturbation leads to a mixing of the two modes and spreads out their frequencies [17]. The second-order modes are enhanced, conserving the original spectral weight so the integrated absorption intensity of the band is unchanged by the anharmonic perturbation. If the spectral resolution is not enough to resolve the two modes the resulting picture is similar to the original one without a perturbation. The Fermi resonance effect has not been seen in C_{60}.

Figure 1.6 shows the results of the numerical calculations based on the Eqs. 1.13-1.15. Some trends in the spectrum are clear already from the equations. First of all the second-order intensities are relatively weak compared to the experimental spectrum in Fig. 1.2 (the experimental picture here is somewhat misleading due to the saturation of first-order peaks). Most intense modes have frequencies close to the four IR bands, leaving high-frequency combination modes practically invisible. Moreover there are relatively intense difference modes (identified by their strong temperature dependence) in the lower part of the spectrum. These features are in contradiction to experiment, thus excluding mechanical anharmonicity as the mechanism for activating the observed weak modes. In matching the combination modes to experimental data, authors in Ref. [8] did not find any evidence for a significant deviation of the frequencies of these modes from the values of $\omega_i + \omega_j$. This supports the

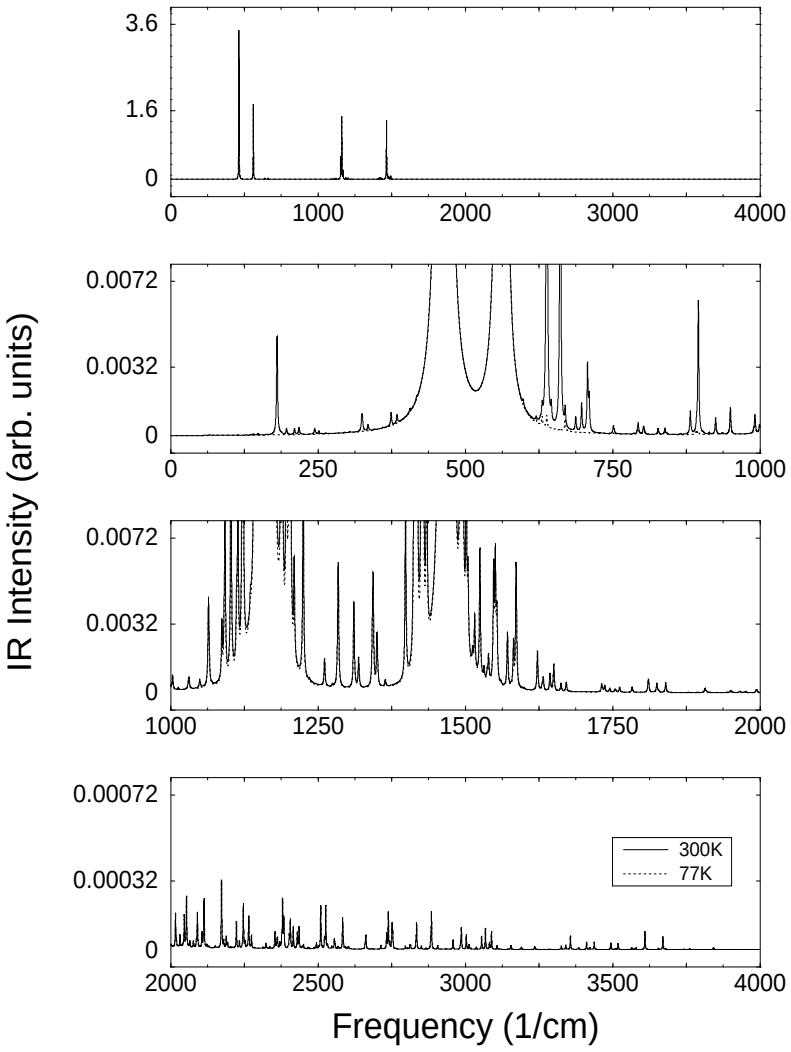

Figure 1.6: IR spectra at 300 and 77 K computed using the mechanical anharmonicity model. Difference modes are easily identified by their strong temperature dependence, while combination modes show no such trends.

above conclusion that mechanical anharmonicity is not producing significant effects in the C_{60} IR spectrum, since the relative frequency shift as a consequence of mechanical anharmonicity only is of the same order of magnitude as the relative intensities of the second-order modes.

1.4 Electrical Anharmonicity Model

The electrical anharmonicity (EA) is a less studied phenomenon of molecular physics than the mechanical one. It is based on the fact that the dipole moment is generally a nonlinear function of normal modes. In view of Eqs. 1.2 and 1.5, electrical anharmonicity arises from the second term in Eq. 1.5, while the ionic dynamics is harmonic ($C_{iq,jr,ks}$=0). Selection rules for the second-order modes are reflected in the elements of the matrix $\mathbf{M}_{jr,ks}$, and are the same as in the case of the mechanical anharmonicity. Since the ionic dipole moment is linear in ionic positions it is clear that the nonlinear contribution stems from a nonlinear response of electronic positions to a change in ionic configuration. A harmonic treatment now suffices for the ionic displacements; the Weeks model [27] is used.

The nonlinear electronic response is modeled in the following way. Consider again a π electron in the field of its parent ion and adjacent bond charges. The interaction with its nearest-neighbor ions is governed by the Coulomb potential

$$V_{e-i}(\mathbf{r}_i) = -\kappa_i \sum_j \frac{1}{|\mathbf{R}_i - \mathbf{R}_j^{(i)} + \mathbf{r}_i|} \tag{1.17}$$

and similarly the interaction with adjacent bond electrons is given by

$$V_{e-be}(\mathbf{r}_i) = \kappa_{be} \sum_j \frac{1}{|(\mathbf{R}_i - \mathbf{R}_j^{(i)})/2 + \mathbf{r}_i|}. \tag{1.18}$$

The summations are over the three nearest ions j and $\mathbf{R}_i$ is the position of the vertex ion. Note that while $\mathbf{R}$'s are measured from the mass center of C_{60}, $\mathbf{r}_i$ is measured from the position of the ith vertex ion ($\mathbf{R}_i$). The strengths of the interactions are measured by some effective charges κ_i and κ_{be} for neighbor ions and adjacent bond electrons, respectively. Only the ratio κ_i/κ_{be} is a relevant fitting parameter. The motion of the π electron in the field of its vertex ion is simplified by restricting it to a sphere around the ion with a radius R, which will be the second fitting parameter:

$$\mathbf{r}_i = R\mathbf{n}_i. \tag{1.19}$$

This gives a simple two-dimensional minimization scheme: for each vertex and a pair of fitting parameters $(R, \kappa_i/\kappa_{be})$ find a unit vector $\mathbf{n}_i$ such that the function

$$V_{e-i}(\mathbf{n}_i) + V_{e-be}(\mathbf{n}_i) \tag{1.20}$$

is minimal. The electrical dipole moment is then computed and resulting first-order intensities (Eq. 1.13) compared with corresponding experimental values. The best fit corresponds to values of $R = 0.06$Å and $\kappa_i/\kappa_{be} = 4.80$. For some range of the parameters there are two electron positions for which the potential in Eq. 1.20 has a local minimum. In such cases the global one was considered. The best fit lies in the region with one minimum. It is obvious that the best fits have no physical justification. To support the model we did simulations

with different, more physical values of the free parameters obtaining the same qualitative picture as will be shown later. It is also appropriate to remark that a feedback from the adiabatic changes in electronic positions to ionic motion is implicitly considered in the harmonic level in the force-constant model.

Second-order absorption intensities of combination and difference modes now have simple forms [19]:

$$I^{EA}_{\omega_k+\omega_l} = \frac{\hbar}{2m}\frac{\omega_k+\omega_l}{\omega_k\omega_l}(1+n_k+n_l)\sum_{r,s=1}^{g_k,g_l}\mathbf{M}^2_{kr,ls}, \tag{1.21}$$

$$I^{EA}_{\omega_k-\omega_l} = \frac{\hbar}{2m}\frac{\omega_k-\omega_l}{\omega_k\omega_l}(n_l-n_k)\sum_{r,s=1}^{g_k,g_l}\mathbf{M}^2_{kr,ls}. \tag{1.22}$$

Figure 1.7 shows the spectrum obtained from Eqs. 1.21 and 1.22. The following features can be extracted. The overall intensity of the weak modes is higher (in relative sense) than in the case of the mechanical anharmonicity. Spectral weight is shifted towards higher frequencies. This is a consequence of high sensitivity of electronic positions to tangential distortions, which are characteristic for higher-frequency modes. The sensitivity of electrons to the tangential ionic motion is also the reason that difference peaks have relatively very small intensity (the difference peaks are most intense in the region of 600 - 1000 cm^{-1}, however, the intensities are much smaller than those of combination modes in the region 1000 - 3500 cm^{-1}). There is obviously no resonance effect since the two terms in the Eq. 1.5 are independent. The frequency distribution in the Weeks model differs from that in C_{60} so a closer comparison with experiment is not possible. One consequence is that in Fig. 1.7 weak features up to 4000 cm^{-1} are visible, while experimentally weak peaks above 3500 cm^{-1}

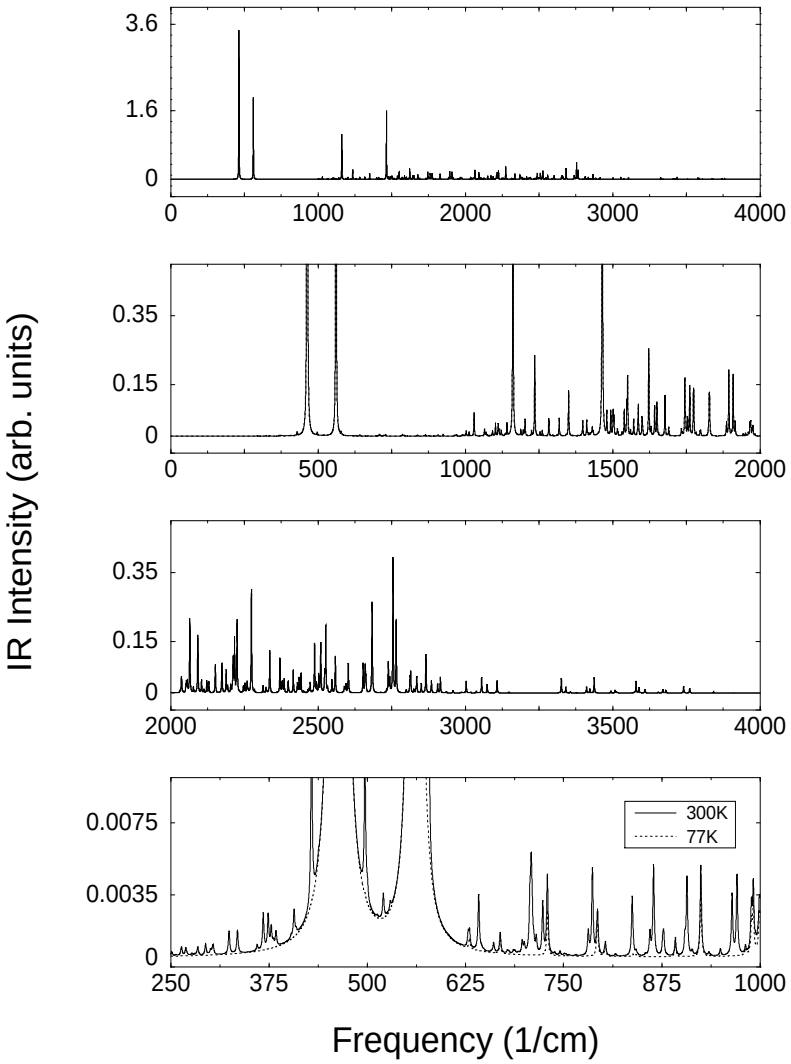

Figure 1.7: The electrical anharmonicity model produces absorption spectra which show similar trends as experimental ones. Difference peaks carry very little spectral weight compared to high-frequency combination ones.

have not been resolved. This difference in the frequency distribution may be a part of the reason why our model has so little activity in the region 600-1000 cm^{-1}. Note that almost all of the peaks experimentally observed in this region were associated with modes IR forbidden in the second-order [7, 8] and their appearance must be accounted for by other mechanisms.

1.5 Conclusions

We studied the possibility that the weak modes seen in the IR spectrum of C_{60} are activated by either isotope symmetry breaking or anharmonicity (or both). If the modes were activated by the isotope effect, their intensities would be enhanced by an additional ^{13}C enrichment, as calculated in Sec. 1.2. Such an enhancement was not seen experimentally. We therefore concluded that the isotope effect does not activate the weak modes.

Anharmonicity can enter an IR spectrum as either mechanical or electrical. We have proposed simple semiempirical models of the two phenomena. The main features of our models are (i) separation of ionic dynamics and mechanism of optical activation (the models can be used for any set of normal modes), and (ii) emphasis on the π-electronic system rather than on bond charges. Both models give a spectrum of combination and difference modes which is compared with IR measurements. It is found that mechanical anharmonicity exhibits features different from those observed. These features can be already expected from basic formulas (e. g., those of Eqs. 1.14 and 1.15) and the model described in Sec. 1.3 only helps to visualize them. As a by-product

the intensities of four first-order IR-allowed bands are well reproduced.

The electrical anharmonicity model introduced in Sec. 1.4 is based on a nonlinear response of π electronic configuration to ionic distortions. Now the absorption spectrum has fewer characteristics given *a priori* by a theoretical formula and is more model dependent. The main feature of the model, which leads to a quite successful comparison of its spectrum with experiment, is that electronic positions are much more sensitive to tangential ionic motions than to radial ones.

The separation of mechanical and electrical anharmonicity is posteriorly justified by the dominance of the latter. However, the IR activity around four first-order peaks is caused by mechanical anharmonicity due to resonance effects, as discussed in Sec. 1.3. There is still a region of optical activity (600-1000 cm^{-1}) that this simple model cannot explain. Although trial assignments exclude most of the observed peaks in the region as combination modes, the question is still an open one and more sophisticated quantum-mechanical treatment can yield more authoritative results.

The possibility that the crystal field arising from the fcc environment can break the I_h symmetry and activate some of the silent modes was not considered in this chapter. There is, however, an experimental evidence [14], that this effect is visible in the spectrum. Namely, the evidence comes from the fact that some of the modes disappear above 260 K, where C_{60} start to rotate. It is difficult to qualitatively assess this mechanism. Mostly because the van der Waals forces acting between two C_{60} molecules in a crystal environment are at least 100 times smaller than the covalent forces between the C atoms. A

naive estimate would lead to the crystal field perturbation that yields modes with the intensities by a factor of 0.0001 smaller than the first order intensities, while experimentally seen weak modes have intensities of the order of 0.1 to 0.001 of the first-order modes. Nevertheless, a realistic calculation (e. g., with the intermolecular potential of Lu *et al.* [36]) is required to conclude on the role of the crystal environment in the IR spectrum of C_{60}.

Bibliography

[1] A. F. Hebard, M. J. Rosseinsky, R. C. Haddon, D. W. Murphy, S. H. Glarum, T. T. M. Palstra, A. P. Ramirez, and A. R. Kortan, Nature **350**, 600 (1991).

[2] M. Schlüter, M. Lannoo, M. Needels, G. A. Baraff, and D. Tománek, J. Phys. Chem. Solids **53**, 1473 (1992); M. Schlüter, M. Lannoo, M. Needels, and G. A. Baraff, Phys. Rev. Lett. **68**, 526 (1992); C. M. Varma, J. Zaanen, and K. Raghavachari, Science **254**, 989 (1991).

[3] S. Chakravarty, M. Gelfand, and S. Kivelson, Science **254**, 970 (1991); S. Chakravarty and S. Kivelson, Europhys. Lett. **16**, 751 (1991).

[4] W. Kratschmer, K. Fostiropoulos, and D. R. Huffman, Chem. Phys. Lett. **170**, 167 (1990).

[5] D. S. Bethune, G. Meijer, W. C. Tang, H. J. Rosen, W. G. Golden, H. Seki, C. A. Brown, and M. S. de Vries, Chem. Phys. Lett. **179**, 181 (1991).

[6] J. P. Hare, J. Denis, H. W. Kroto, R. Taylor, A. W. Allaf, S. Balm, and D. R. M. Walton, J. Chem. Soc. Chem. Comm. **1**, 412 (1991).

[7] K.-A. Wang, A. M. Rao, P. C. Eklund, M. S. Dresselhaus, and G. Dresselhaus, Phys. Rev. B **48**, 11 375 (1993).

[8] M. C. Martin, X. Q. Du, J. Kwon, and L. Mihaly, Phys. Rev. B **50**, 173 (1994).

[9] K. Kamarás, L. Akselrod, S. Roth, A. Mittelbach, W. Hönle, and H. G. von Schnering, Chem. Phys. Lett. **214**, 338 (1993).

[10] Z.-H. Dong, P. Zhou, J. M. Holden, P. C. Eklund, M. S. Dresselhaus, and G. Dresselhaus, Phys. Rev. B **48**, 2862 (1993).

[11] P. H. M. van Loosdrecht, P. J. M. van Bentum, M. A. Verheijen, and G. Meijer, Chem. Phys. Lett. **198**, 587 (1992); P. H. M. van Loosdrecht, P. J. M. van Bentum, M. A. Verheijen, and G. Meijer, Phys. Rev. Lett. **68**, 1176 (1992).

[12] B. Chase, N. Herron, and E. Holler, J. Phys. Chem. **96**, 4262 (1992).

[13] C. Coulombeau, H. Jobic, P. Bernier, C. Fabre, D. Schütz, and A. Rassat, J. Phys. Chem. **96**, 22 (1992); J. R. D. Copley, D. A. Neumann, R. L. Cappelletti, and W. A. Kamitakahara, J. Phys. Chem. Solids **53**, 1353 (1992).

[14] L. Mihaly and M. C. Martin, in *Proceedings of the 1995 International Winterschool on Electronic Properties of Novel Materials: Fullerides and Fulleroids*, edited by H. Kuzmany, J. Fink, M. Mehring, and S. Roth (World Scientific, Singapore, 1995).

[15] M. C. Martin, J. Fabian, J. Godard, P. Bernier, J. M. Lambert, and L. Mihaly, Phys. Rev. B **51**, 2844 (1995).

[16] S. Sanguinetti, G. Benedek, M. Righetti, and G. Onida, Phys. Rev. B **50**, 6743 (1994).

[17] G. Herzberg, *Infrared and Raman Spectra of Polyatomic Molecules* (van Nostrand, New York, 1966).

[18] M. Lax and E. Burstein, Phys. Rev. **97**, 217 (1955).

[19] B. Szigeti, Proc. Roy. Soc. A **252**, 217 (1959); B. Szigeti, Proc. Roy. Soc. A **258**, 377 (1960).

[20] B. Szigeti, in *Lattice Dynamics*, edited by R. F. Wallis (Pergamon, New York, 1963), p. 405.

[21] D. L. Mills, C. J. Duthler, and M. Sparks, in *Dynamical Properties of Solids*, edited by G. K. Horton and A. A. Maradudin (North Holland, Amsterdam, 1980), Vol. 4, p. 377, and references therein.

[22] M. Sparks, Phys. Rev. B **10**, 2581 (1974).

[23] B. Friedman, Mol. Cryst. Liq. Cryst. **256**, 251 (1994).

[24] G. F. Bertsch, A. Smith, and K. Yabana, Phys. Rev. B **52**, 7876 (1995).

[25] M. I. Salkola, S. Chakravarty, and S. Kivelson, Int. J. Mod. Phys. **7**, 2859 (1993).

[26] P. Giannozi and S. Baroni, J. Chem. Phys. **100**, 8537 (1994).

[27] D. Weeks, J. Chem. Phys. **96**, 7380 (1992).

[28] E. B. Wilson, J. C. Decius, and P. C. Cross, *Molecular Vibrations* (Dover, New York, 1980), p. 162.

[29] G. Onida and G. Benedek, Europhys. Lett. **18**, 403 (1992); Erratum, *ibid.* **99**, 343 (1992).

[30] K. Hedberg, L. Hedberg, D. S. Bethune, C. A. Brown, H. C. Dorn, R. D. Johnson, and M. de Vries, Science **254**, 410 (1991).

[31] M. C. Martin, D. Koller, and L. Mihaly, Phys. Rev. B **47**, 14607 (1993).

[32] Z. C. Wu, D. A. Jelski, and T. F. George, Chem. Phys. Lett. **137**, 291 (1987); S. J. Cyvin, E. Brendsdal, B. N. Cyvin, and J. Brunvoll, *ibid.* **43**, 377 (1988).

[33] R. A. Jishi, R. M. Mirie, and M. S. Dresselhaus, Phys. Rev. B **45**, 13 685 (1992); J. L. Feldman, J. Q. Broughton, L. L. Boyer, D. E. Reich, and M. D. Kluge, *ibid.* **46**, 12 731 (1992); D. W. Snoke and M. Cardona, Sol. State Cmm. **87**, 121 (1993); D. Inomata, N. Kurita, S. Suzuki, and K. Nakao, Phys. Rev. B **51**, 4533 (1995).

[34] D. E. Weeks and W. G. Harter, Chem. Phys. Lett. **144**, 366 (1988); D. E. Weeks and W. G. Harter, Chem. Phys. Lett. **176**, 209 (1991).

[35] J. Fabian (unpublished).

[36] P. Lu, X.-P. Li, and R. M. Martin, Phys. Rev. Lett. **68**, 1551 (1992).

Chapter 2

Vibrational Properties of Amorphous Silicon

2.1 Introduction

This chapter examines vibrational states in glasses (the term glass will be used to denote amorphous solids in general, though in experimental literature this term is reserved for amorphous solids quenched from melt). In the absence of any unifying principles in the physics of vibrations in glasses, our approach is to investigate a model system—amorphous silicon.

Amorphous silicon is an important electronic material (e.g., when enriched with hydrogen atoms it is used for solar cells). Its modeling is attractive for several reasons. (1) There are relatively strict constraints on its structure. The majority of atoms form tetrahedrons (as in silicon crystals) with randomized bond angles, but almost unvaried bond lengths. The structure factor of amorphous silicon has been measured and can be compared with a calculated one to support or reject a model. In fact, there already exists a numerical recipe (the Wooten-Winer-Weaire algorithm [1]) for creating a realistic glassy structure

with tetrahedral coordination. (2) Many empirical potentials simulating the covalent bonding between silicon atoms have been suggested. One can choose according to one's needs. We use the Stillinger-Weber potential [2] which is simple and realistic. This potential (a) is short ranged, (b) anharmonic, and (c) its defects are well established [3, 4, 5] (e.g., the frequencies of the optic modes are overestimated by 15%). (3) Amorphous silicon is an elemental system. Qualitative analysis of numerical results is therefore easier than for more complex materials. In addition, models of amorphous silicon can be extended to describe glassy alloys like Si_xGe_{1-x}, to study, for example, the role of extrinsic mass disorder in the vibrations of glasses. Once the qualitative analysis is made, one can conjecture about its generalization to other glasses as well. We have good reasons to believe that many of the results in this chapter are valid for other semiconducting and insulating glasses (in metallic glasses the interatomic forces are long ranged so it would not be appropriate to extend our results there). (4) Crystalline silicon is a well studied material both experimentally and theoretically. It provides a benchmark when analyzing numerical data on amorphous silicon. When possible, calculations are performed in parallel for both crystalline and amorphous cases, to explicitly show the correlation between structure and vibrational dynamics.

There are also disadvantages in considering amorphous silicon. Many experimental data are still lacking. For example, the thermal expansivity of amorphous silicon has been measured only once and only at one temperature. Sound attenuation has not been measured at all. The reason is that amorphous silicon can be prepared in thin films only (e.g., by ion-beam sputtering); it

is difficult to measure on thin films. Also, at very low temperatures (less than 1 K) amorphous silicon behaves differently from other glasses. Excessive degrees of freedom (in comparison with crystals) have been measured for the majority of glasses in this temperature range. A generally accepted (but not understood) idea is that there are local double-well-like potentials with random parameters, distributed throughout a glass. These excessive degrees of freedom have not been observed in amorphous silicon (a little excess in specific heat is caused by dangling spins). In any case, the finite size of our models does not allow us to explore such low temperatures.

Complex structure should be reflected in complex vibrational dynamics. At very low frequencies the vibrational states have large enough wavelengths to not see (microscopic) structural defects. The modes are acoustic-like phonons (sound waves). Scattering of the phonons from (hypothetical) tunneling states of the double-well potentials seems to explain many unusual properties of glasses at low temperatures. At higher frequencies the phonons interact with defects. If the interaction is resonant (i.e., the phonon frequency matches the frequency of a particular defect), it leads to a new type of modes—resonance modes. If the interaction is elastic (Rayleigh scattering), the modes maintain their wave character until their mean free path ℓ becomes comparable to their wavelength λ. The "$\ell \approx \lambda$" is the Ioffe-Regel limit [6], beyond which one cannot speak of waves any more. Wave vector and polarization become invalid concepts. Instead, the corresponding modes have zero group velocity and transfer energy diffusively rather than ballistically. We call the modes diffusons. At very high frequencies, in the tail of the spectrum, modes be-

gin to localize. Numerical calculations confirm that only a few percent of vibrational modes are localized (we call them locons). Section 2.2 introduces the above spectrum of vibrations for amorphous silicon. A clear connection between structure and spatial characteristics of different modes is made. In particular, the correlation between resonant (localized) modes and groups of under(over)coordinated atoms is established.

Based on the above picture, Allen and Feldman [7, 8] have developed a theory of heat transport in glasses (see also [9]). In crystals heat is carried by ballistically propagating phonon wave packets. The coefficient of heat conductivity is finite due to anharmonic interactions between phonons (umklapp processes). This mechanism does not work for glasses since ballistic propagation is restricted to low-frequency phonons. Instead, the majority of modes are nonpropagating—their group velocity is zero. Wave packets created from these modes only diffusively spread out (from here the name diffusons). Heat is therefore transferred by diffusion. The heat conductivity coefficient is finite even at harmonic level; the role of anharmonicity is to achieve a steady state with a local temperature, by redistributing vibrational energies among the states. Allen and Feldman used a Kubo formula for heat transport to show that heat conductivity κ can be written as

$$\kappa = \frac{1}{V} \sum_i C_i(T) D_i, \tag{2.1}$$

where C_i is the heat capacity of the ith mode and D_i is the "mode diffusivity." The mode diffusivity is an intrinsic property of the ith normal mode; it can be calculated by using only harmonic eigenstates. In addition D_i provides an

unambiguous criterion for localization. Locons have $D_i = 0$ and thus make no contribution to κ. To support their theory Feldman et al. [8] have calculated κ for models of amorphous silicon. The results are in agreement with experiment.

The present work goes beyond harmonic approximation. It is an extension of the work of Allen and Feldman in that various properties where anharmonicity is explicitly manifested are calculated. Section 2.3 introduces the concept of vibrational relaxation times in glasses. Relaxation times are needed to know how fast a system of (almost independent) vibrational modes achieves a steady state. A small perturbation (such as a monochromatic laser pulse) shifts the population of a particular mode from its equilibrium value. Perturbation theory gives a recipe how to evaluate the time needed for the mode to return back to equilibrium. We apply the perturbation formula for our model of amorphous silicon. The relaxation times are evaluated for different modes and different temperatures. The results show that vibrations in glasses decay on picosecond time scales and the times decrease with increasing frequency. This is independent of the character of the modes under consideration. Locons, diffusons, and low frequency phonons have similar relaxation times. This is little surprising. Decay mechanism must be different for different modes. Locons are spatially localized so the probability, for example, of a locon to decay to two other locons is very small. Indeed, the fracton model [10] used this as an assumption that such three-locon decay processes can be neglected. The resulting picture then seemed to be in accord with the experiment of Scholten et al. [11, 12] that indicated nanosecond time scales for the relaxation times and an exponential increase of the times with frequency. Our realistic calcula-

tion shows that the experiment has been misinterpreted. Unfortunately we do not have a plausible explanation for the experimental observations. As for the fracton model, Sec. 2.4 explicitly shows that three-locon interactions cannot be neglected. To consider decay rates, in addition to the probability of a process to occur one has to consider the magnitude of the corresponding matrix element. Simple scaling shows that if the probability is small the magnitude is large. This is why different modes have similar decay rates.

There is much to be learned about the modes from the study of individual decay processes (not summed over final states continuum). In Sec. 2.3 we show that in contrast to propagating phonons, diffusons do not have other selection rules than energy conservation. On the other hand the decay mechanics of locons is much more complex. Decay of a locon to two others is selective in that the three modes must spatially overlap. If a locon decays to another locon and a low-frequency phonon, the situation can be described as a "phonon assisted hopping." If the phonon in the decay is not of a low frequency, the two participating locons can overlap and we cannot speak of "hopping." Such a decay has different rules. Consequencies of the complex decay mechanics in transport process are yet to be explored.

Another interesting anharmonic property is thermal expansion. Although there exist plenty of experimental data on the subject, little is known about the physics behind this phenomenon (again, in crystals the situation is well understood due to the simplicity of their vibrational spectrum). Thermodynamics

relates thermal expansivity α with mode Grüneisen parameters γ_i:

$$\alpha \sim \sum_i \gamma_i C_i. \tag{2.2}$$

The Grüneisen parameters measure how sensitive vibrational frequencies are to volume change ($\gamma_i = -\partial \ln \omega_i / \partial \ln V$). To the lowest approximation γ_i are T independent and α follows temperature dependence of specific heat. It is constant above Debye temperature and in crystals varies as T^3 at low temperatures. In glasses the low temperature behavior depends on glass. It can be negative or positive, typically with linear T dependence. Such a behavior cannot be explained in terms of the tunneling model and several schemes have been devised to explain it. The Grüneisen parameters of low-frequency modes have been conjectured to have anomalously large negative values. Again, there is no agreement in the literature about the origin of these values. More important is the room temperature behavior of α. It has been found that α is very sensitive on preparation method. In Sec. 2.5 we try to explain this. We use perturbation theory to evaluate γ_i for the modes in amorphous silicon. We observe that resonance modes have unusually large negative γ_i (up to -30; typical "phonon" value is around 1). This may explain some of the low-temperature properties of α. In addition, different models give slightly different α. This is related to internal strain. If volume changes, the new "rescaled" positions will not, in general, be the new equilibrium positions (in crystals with atoms at centers of symmetry they would be). At the new volume the atoms further relax. This causes large changes in the frequencies of the resonant modes. Different samples have different concentrations of soft regions where resonant

modes have largest amplitude. This leads to the measured sample dependence of α.

The chapter is concluded by a brief account of our current projects. The topics in Sec. 2.6 have little in common (besides that they deal with vibrations in glasses). First we try to establish a connection between random matrix theory and diffusons. It is shown that diffusons can be indeed described as eigenstates of a random matrix (with a proper symmetry), indicating a possibility to develop an analytical model for these states. On the other hand, locons show no sign of "random-matrix" behavior. Their neighboring frequencies are almost uncorrelated. This is well known: neighboring locons spatially repel each other. The repulsion then inhibits spectral correlations. Next we evaluate the sensitivity of vibrational frequencies to boundary conditions. Thouless showed that this sensitivity is connected (via a kind of uncertainty principle) to mode diffusivity. What Thouless showed for electrons we try to establish for vibrations. The last topic in Sec. 2.6 deals with sound attenuation. Only a draft of a general theory of the vibrational contribution to sound wave damping is presented. We start from a Kubo formula and a kinematic expression for the momentum-current operator to arrive at a perturbation result suitable for numerical calculations. Surprisingly, in contrast to heat conductivity, sound attenuation of glasses is a purely anharmonic effect. Sound energy is dissipated in the relaxation process where vibrations and equilibrium atomic positions try to find a local steady state at a given value of (sound wave determined) strain.

2.2 Model of Amorphous Silicon

2.2.1 Structure

Our model is based on the algorithm developed by Wooten, Winer, and Weaire (WWW) in 1985 [1]. The WWW algorithm applied to silicon, starts with atoms arranged in a diamond cubic lattice (silicon crystal with the lattice constant 5.431 Å, see Fig. 2.1). A random-network structure of amorphous silicon is obtained in two steps. First, bond transpositions are performed on randomly chosen pairs of second-neighbor bonds. In the transposition, two bonds are "cut" and a new pair of bonds, each containing atoms from both original bonds, is formed. The resulting configuration is relaxed to a nearest local minimum of an interatomic potential (usually of the Keating type with periodic boundary conditions applied). This step is repeated many times (of the order of N, the number of atoms in the sample). In the second step, simulated annealing brings the sample to an energy corresponding to a temperature $T \approx 0$ K. (The first step treats the sample as if it were at $T = \infty$; structures of different energies have equal probability to occur.) The annealing proceeds via topological relaxations: two bonds are transposed at random on a trial basis, and the energies of the old and new structures are compared. If the new structure has a lower energy, it is accepted; if the energy is higher by ΔE, the new structure is accepted with the probability $\exp(-\Delta E/k_B T)$, where k_B is the Boltzmann constant.

To make the WWW structure suitable for realistic calculations, we have to

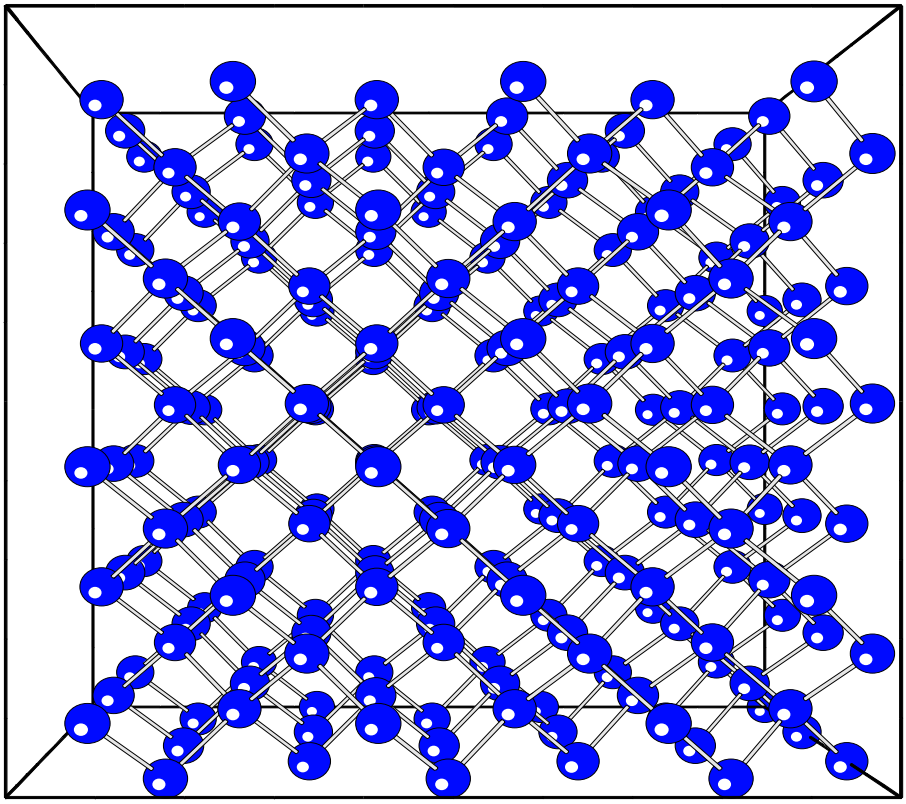

Figure 2.1: Input to the WWW algorithm: 216 silicon atoms in a diamond cubic structure.

add realistic interatomic potentials. From more than 30 potentials suggested in literature, we take the Stillinger-Weber (SW) potential V_{SW} [2], suggested originally for silicon liquid. The SW potential is relatively simple and contains relevant physics. It consists of two- and three-body terms. The two-body (bond-stretching) term is

$$V_2(r) = ef(r/s), \tag{2.3}$$

where $e = 2.1675$ eV, $s = 2.0951$ Å, and the function $f(x)$ is defined as

$$f(x) = A(Bx^{-p} - 1)\exp\left(\frac{1}{x-q}\right), \tag{2.4}$$

with the parameters $A = 7.05$, $B = 0.60$, $p = 4$, and $q = 1.80$. Potential $V_2(r)$ has minimum at $r \approx 2.35$ Å, the interatomic distance in silicon crystal. The three-body (bond-bending) term between atoms a, b, and c, that form angle θ with the vertex at a, has the form

$$V_3(r_{ab}, r_{ac}, \theta) = ef(r_{ab}/s, r_{ac}/s, \theta). \tag{2.5}$$

The distance from a to b (c) is denoted as r_{ab} (r_{ac}), and the function $f(x, y, \theta)$ is given by

$$f(x, y, \theta) = l\left(\cos\theta + \frac{1}{3}\right)^2 \exp\left(\frac{g}{x-q} + \frac{g}{y-q}\right). \tag{2.6}$$

The parameters $l = 21.0$ and $g = 1.2$. The three-body 2.5-2.6 term ensures stability of tetrahedral coordination (in a tetrahedron $\cos\theta = -1/3$). After the WWW network is built, a relaxation is made to a nearest local minimum of the SW potential. To minimize pressure, the sample length L is allowed

to change. Typically a pressure below atmospheric was achieved, but we also performed calculations with a model under 1 kbar of negative pressure. The calculations show that some of the modes (namely the resonance ones, see Sec. 2.2.2) are very sensitive to pressure (and structure in general). We will show that this behavior of resonance modes is responsible for considerable sample sensitivity of thermal expansion (Sec. 2.5) and sound attenuation (Sec. 2.6) of glasses.

The resultant WWW random network preserves the bond length (≈ 2.35 Å), but randomizes the bond angles ($\approx 109°$). This is a requirement of experiment: neutron diffraction measurements showed that in amorphous materials with covalent bonding the bond length fluctuations are weak. On the other hand, the bond angles fluctuate by up to 20% around their crystalline values.

In the following sections we use the random-network models with 216 and 1000 atoms (occasionally also with 4096 atoms [13]). Table 2.1 lists selected properties of these models and of the crystalline silicon with the SW interatomic potential. The table shows that the 216-atom model is more "crystalline" than the 1000-atom model. This is because the latter was built to be topologically less constrained: it contains occasional fourfold rings. Both models are less dense than silicon crystal. Also, bulk modulus is lower in the amorphous case. The reason for this is internal strain: under volume change, atoms in amorphous silicon (as opposed to crystalline silicon) further relax to a new potential minimum corresponding to the new volume. We will show in Sec. 2.5 that internal strain has similar consequencies for thermal expansion.

Figure 2.2 visualizes the 216-atom model. The bond-angle randomness is

Model	N/V (10^{28}/m^3)	Energy/atom (meV)	B (10 GPa)	ω_{max} (meV)	ω_{min} (meV)	ω^c_{min} (meV)
216	4.942	-4.123	9.97	78.34	7.18	12.25
1000	4.785	-4.102	8.86	82.19	4.13	7.43
crystal	4.994	-4.334	10.0	73.60	-	-

Table 2.1: Selected characteristics of the amorphous silicon models and silicon crystal with the SW potential. N/V is number density, B bulk modulus, ω_{max} maximum vibrational frequency, ω_{min} minimum vibrational frequency, and ω^c_{min} minimum vibrational frequency of a crystal with the same N.

evident, as is the preservation of the bond length. It is, however, difficult to answer the question of how realistic our models are, based on the figure alone. We therefore compare in Fig. 2.3 the structure factor $S(Q)$ and the pair correlation function $g(R)$ of the 1000-atom model with the neutron diffraction measurement by Kugler *et al.* [14]. The agreement is excellent. All the peaks in $S(Q)$ are reproduced and the distribution of the first- and second-neighbors displayed in $g(R)$ matches the experiment. The third- and higher-neighbors are not well resolved. This is typical of glasses: the long-range order is lost.

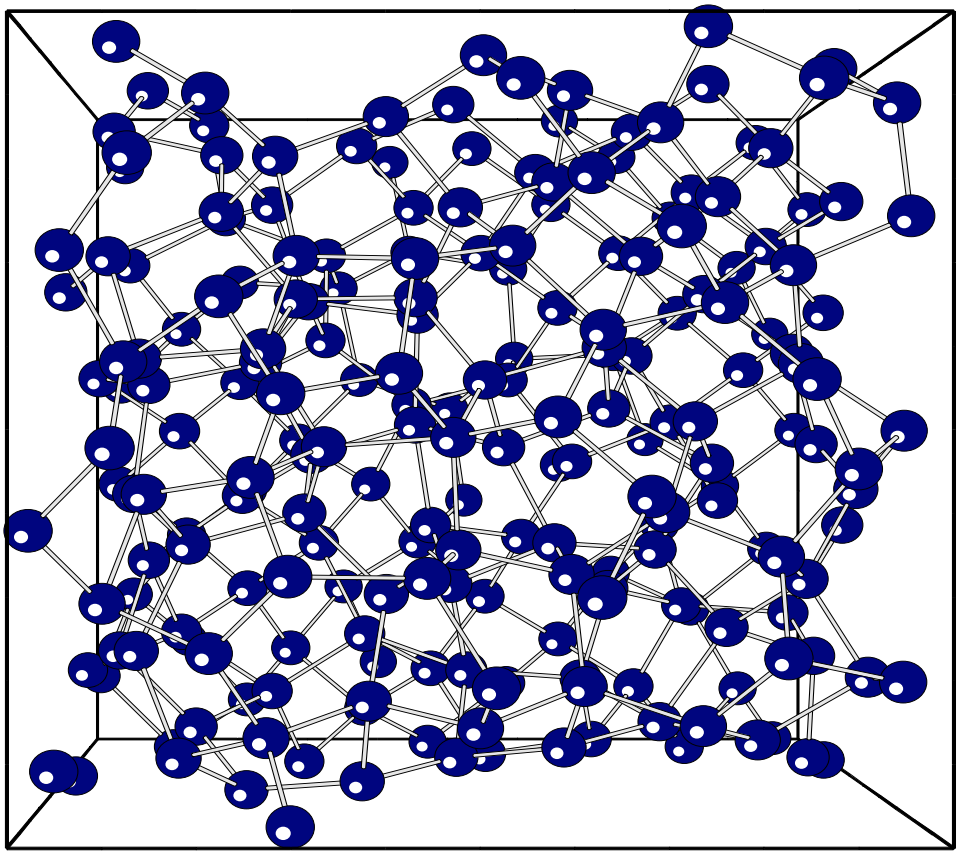

Figure 2.2: The WWW output structure relaxed to a nearest local minimum of the SW potential: a 216-atom model of amorphous silicon.

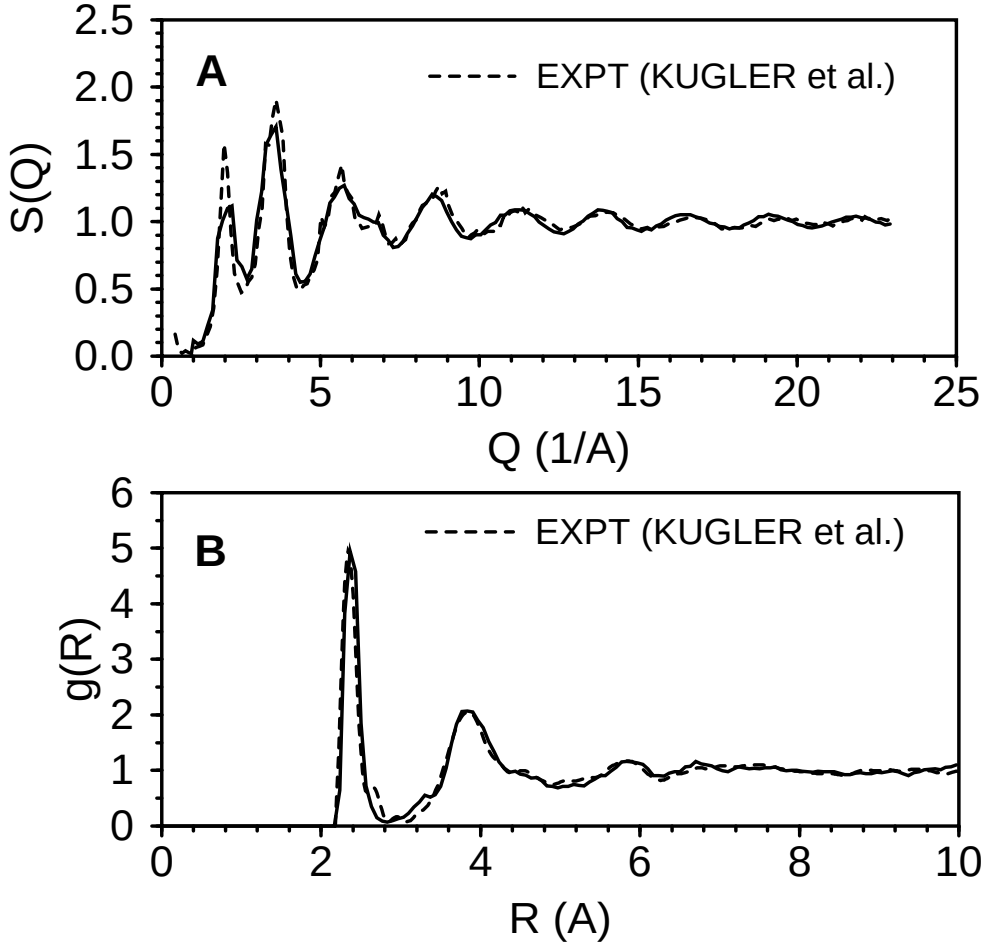

Figure 2.3: (A) Structure factor $S(Q)$ and (B) pair-correlation function $g(r)$ as calculated by using the 1000-atom model (solid line) and measured by neutron diffraction [14] (dashed line).

2.2.2 Vibrations in Glasses: Fundamentals

This subsection is a brief discussion of some of the properties of the harmonic vibrational states found in our models. Vibrational frequencies and eigenstates were obtained by numerical diagonalization of the $3N \times 3N$ force-constant matrix $F_{a\alpha,b\beta}$. Here a denotes atom and α a Cartesian direction x, y, or z. The matrix $F_{a\alpha,b\beta}$ is formed from the second derivatives of the SW potential with respect to atomic displacements $u_{a\alpha}$ around equilibrium:

$$F_{a\alpha,b\beta} = \frac{\partial V_{SW}}{\partial u_{a\alpha} \partial u_{b\beta}}. \tag{2.7}$$

The matrix equation

$$F_{a\alpha,b\beta} e^i_{b\beta} = \omega_i^2 e^i_{a\alpha} \tag{2.8}$$

then defines the frequencies ω_i and vibrational displacement pattern $e^i_{a\alpha}$ of mode i. There are N eigenstates for a model with N atoms. The eigenstates $e^i_{a\alpha}$ are normalized to unity:

$$\sum_a \left| \mathbf{e}^i_a \right|^2 = 1. \tag{2.9}$$

Because of periodic boundary conditions, the three lowest frequencies vanish; they correspond to uniform displacements along the three Cartesian coordinates. In crystals it suffices to take instead of N the number of atoms in a primitive cell. Phase coherence allows to find solution everywhere else. In glasses this is not possible. There is no phase coherence and one must diagonalize matrices with N being the total number of atoms.

Figure 2.4 shows the calculated vibrational density of states (DOS) for the 1000-atom model of amorphous silicon, and for crystalline silicon. The latter

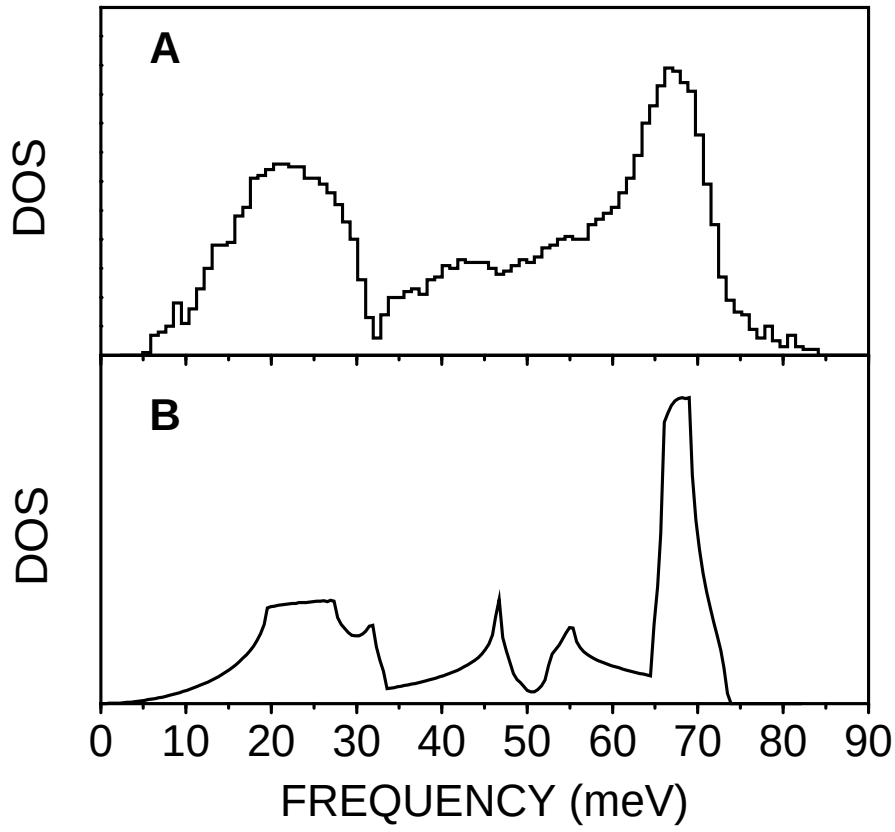

Figure 2.4: Calculated vibrational density of states (DOS) (A) for the 1000-atom model of amorphous silicon and (B) for silicon crystal with the SW potential.

DOS was calculated by using the SW interatomic potential and the tetrahedron method with 1772 tetrahedra in the irreducible wedge of the Brillouin zone. The two spectra are very similar. This is because the interatomic forces forming the force-constant matrix $F_{a\alpha,b\beta}$ are short ranged, so they reflect local atomic arrangements more than global structure. And both amorphous and crystalline silicon have tetrahedral coordinations. The absence of a long-range order in the amorphous case is reflected in the broadening of the van Hove singularities. Another difference between the two spectra is that the maximum frequency ω_{max} (see also table 2.1) is higher in the amorphous case. We will see that this is because the high-frequency modes in amorphous silicon are localized at overcoordinated atoms that form a stiffer environment. The vibrational spectrum has a finite lower limit ω_{min}, since we are dealing with finite-size models. In a finite crystal the lower limit ω^c_{min}, corresponding to the $(1,0,0)2\pi/L$ transverse acoustic phonons, would be higher: $\omega^c_{min} > \omega_{min}$ (see table 2.1). Again, this is because there are topological defects in amorphous structure. But now the defects are "soft," formed by undercoordinated atoms.

An important issue in the physics of vibrations in glasses is localization (in Anderson's sense [15]) that arises due to topological imperfections. What portion of vibrational eigenstates is localized is still a matter of discussion. For example, the fracton model [10] postulates that the *majority* of the states are localized. This model suggests that $\omega_c \approx 5$ meV [1] for amorphous silicon, where

[1]It is customary to call the frequency that separates the region of localized from the region of extended states, the mobility edge ω_c.

maximum vibrational frequency ω_{max} is above 70 meV. On the other hand, realistic model calculations indicate that the majority of modes are extended. For instance, our calculations give $\omega_c \approx 71$ meV, i.e., only 3% of the modes are localized. This value of ω_c has been confirmed in the 4096-atom model [13], and similar results were obtained with other models of glasses as well [16, 17].

A good indicator of localization is the inverse participation ratio $1/P$. For mode i it is defined as

$$1/P^i = \sum_a \left|\mathbf{e}_a^i\right|^4. \tag{2.10}$$

If i is localized at M atoms, the normalization condition 2.9 gives $e_a^i \sim 1/\sqrt{M}$ and $1/P \sim 1/M$. For extended modes ($M \sim N$) one gets $1/P \sim 1/N$, while modes localized at one atom have $1/P \sim 1$. Figure 2.5 shows $1/P$ for the 1000-atom model. The localization transition is clear. The mobility edge is $\omega_c \approx 71$ meV and the comparison with DOS reveals that localization occurs for only 3% of the states. Figure 2.5 suggests that vibrations are localized also at the lower part of the spectrum. We will show that the corresponding modes are actually extended, but have unusually large amplitudes at certain regions. An example of a (genuinely) localized mode is shown in Fig. 2.6. Shown are atoms a such that $|\mathbf{e}_a|^2 > 0.2\,|\mathbf{e}_{max}|^2$, where $|\mathbf{e}_{max}|^2 = \max_a\left(|\mathbf{e}_a|^2\right)$.

What makes modes localize? We already mentioned (and Fig. 2.6 seems to confirm) that localization is correlated with topological defects. As an attempt to quantify this correlation we introduce the *mode average coordination number* z_i. For each atom a we calculate its coordination number z_a as the

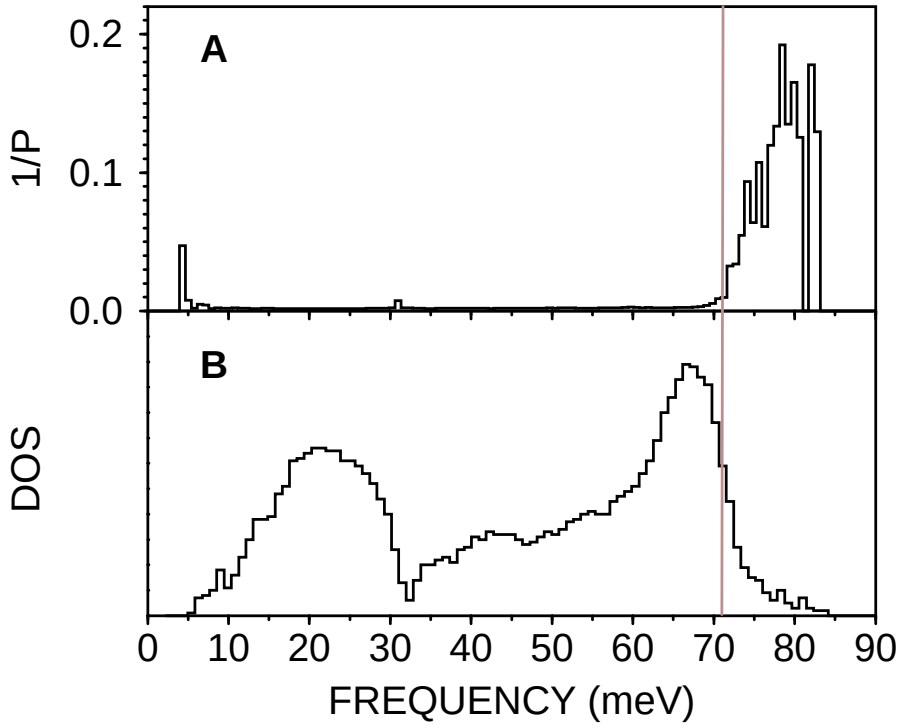

Figure 2.5: Calculated (A) inverse participation ratio $1/P$ and (B) DOS for the 1000-atom model of amorphous silicon. The vertical line is the mobility edge ω_c: modes with $\omega > \omega_c$ are localized.

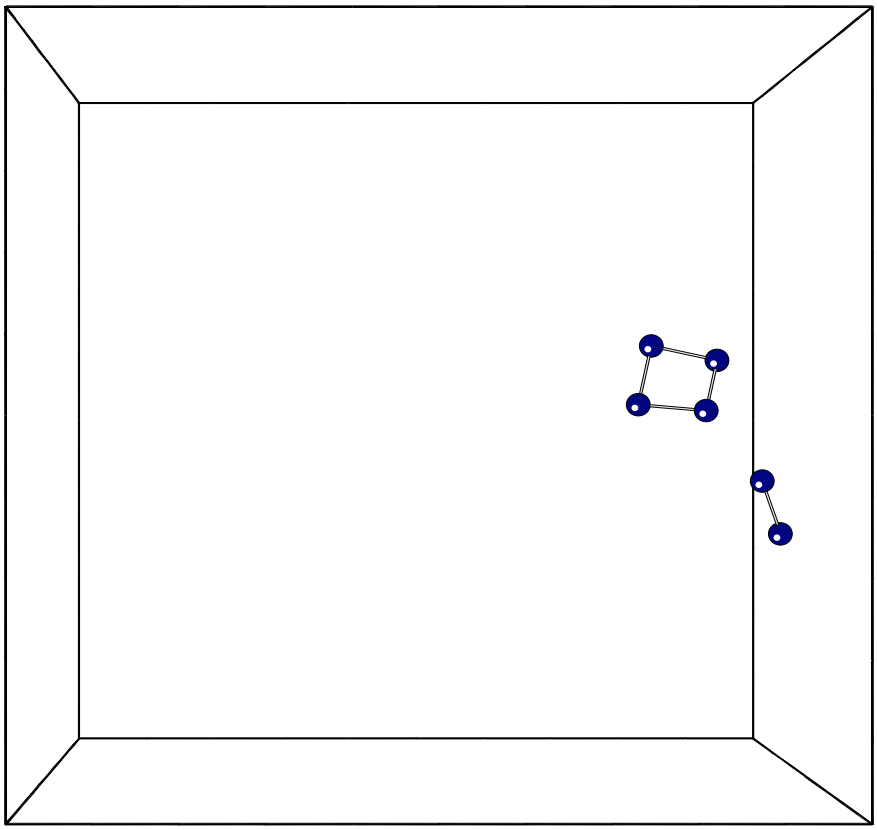

Figure 2.6: The highest-frequency vibrational mode in the 1000-atom model of amorphous silicon. The mode is localized around the fourfold ring—a topological defect not found in silicon crystal. Only the atoms with the largest (see text) vibrational amplitudes are shown.

sum

$$\sum_b w(|\mathbf{r}_a - \mathbf{r}_b|). \tag{2.11}$$

The function $w(x)$ has the value one for $0 < x < r_1$, is linearly decreasing as $(r_2 - x)/(r_2 - r_1)$ for $r_1 \leq x < r_2$, and is zero for $x \geq r_2$. We choose as r_1 and r_2 the nearest neighbor (2.35 Å) and the second nearest neighbor (3.84 Å) distance in crystalline silicon. Then

$$z_i = \sum_a z_a \left|\mathbf{e}_a^i\right|^2. \tag{2.12}$$

If a localized mode i sits at a defect whose atoms have typically different z_a than average, its z_i will also deviate from normal. The result is in Fig. 2.7. The majority of modes have coordinations (as defined by Eq. 2.12) between 4.6 and 4.8. The localized modes, however, are formed at atoms with coordinations greater than 5. This result shows that modes are indeed localized at defects whose atoms are more packed together than on average. Different characters of defects then cause the dispersion of values of z^i. Such a dispersion will be also seen in the mode Grüneisen parameters calculated in Sec. 2.5.

What happens at the lower part of the spectrum is currently an active area of research. There is no doubt that the majority of these modes are like low-frequency acoustic phonons with a wave vector and polarization (after all, glasses do transmit sound waves). Here we are interested rather in the modes that have unusually large P, comparable to high-frequency localized modes. Several works (including ours) suggested that the peculiar modes at the lower part of the spectrum are resonance (or quasi-localized) modes; they

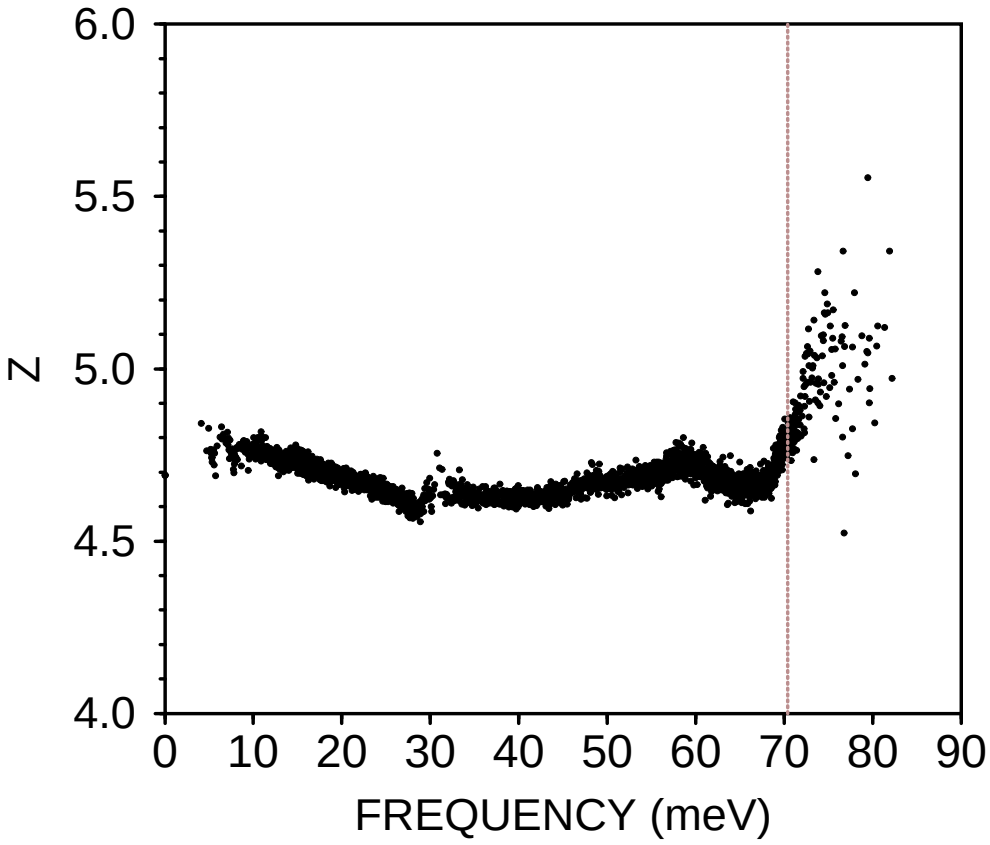

Figure 2.7: Mode average coordination number z_i for the 1000-atom model of amorphous silicon. The increase and dispersion of z^i above ω_c shows that vibrational modes are localized mainly at overcoordinated atoms.

are extended, but have an unusually large amplitude at a particular group of atoms. The resonance modes were first described by Kagan and Iosilevskii [18], Brout and Visscher [19], and Takeno [20] in the studies of vibrations of a heavy impurity in a crystal lattice. The impurity vibration (of a very low frequency) resonantly couples with similar-frequency phonons of the host lattice. The physical picture is similar to the one of a quantum-mechanical particle in a finite potential well: the probability to find the particle in the well is much greater than finding it outside the well, but there is still a finite probability to find it at infinity. The role of potential well (or heavy impurity) is in glasses played by groups of undercoordinated atoms. And how do we know that our finite-size models give resonance (as opposed to localized) modes? Figure 2.8 shows the scaling of P with N for the 216-, 1000-, and 4096-atom model. From Eq. 2.10 one gets $P \sim N$ for extended modes, and P is N independent for localized modes. Figure 2.8 plots P/N versus ω for different N. The graph confirms that P/N does not depend on the sample size for the shown frequencies. The corresponding modes are therefore extended. And because $1/P$ reveals the high amplitude of these modes at a small number of atoms, the modes must be resonant.

A nice way to see the connection between undercoordinated (overcoordinated) groups of atoms and resonance (localized) modes, is to calculate $g(R)$ with origin atoms ($R = 0$) having the largest amplitudes for a given mode. The result of such a calculation is in Fig. 2.9. The solid lines indicate both $g(R)$ and the number of atoms within R from origin (the distinction should be clear: the latter is steadily increasing) for (A) localized modes and (B)

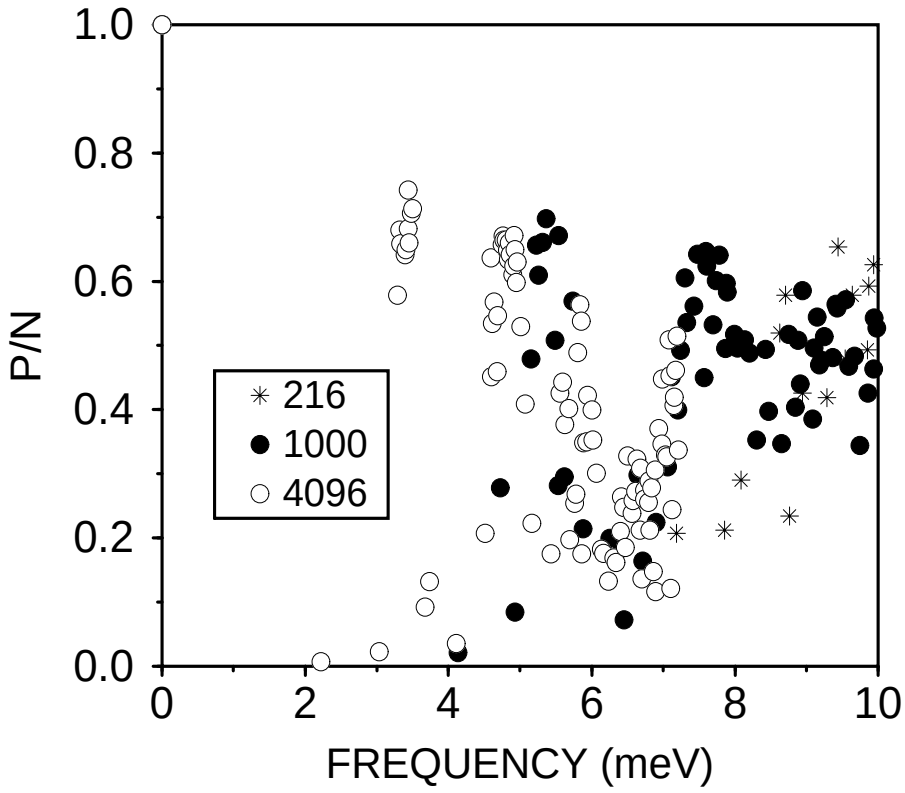

Figure 2.8: Scaling of the mode participation ration P with N (in the legend) for the low-frequency modes.

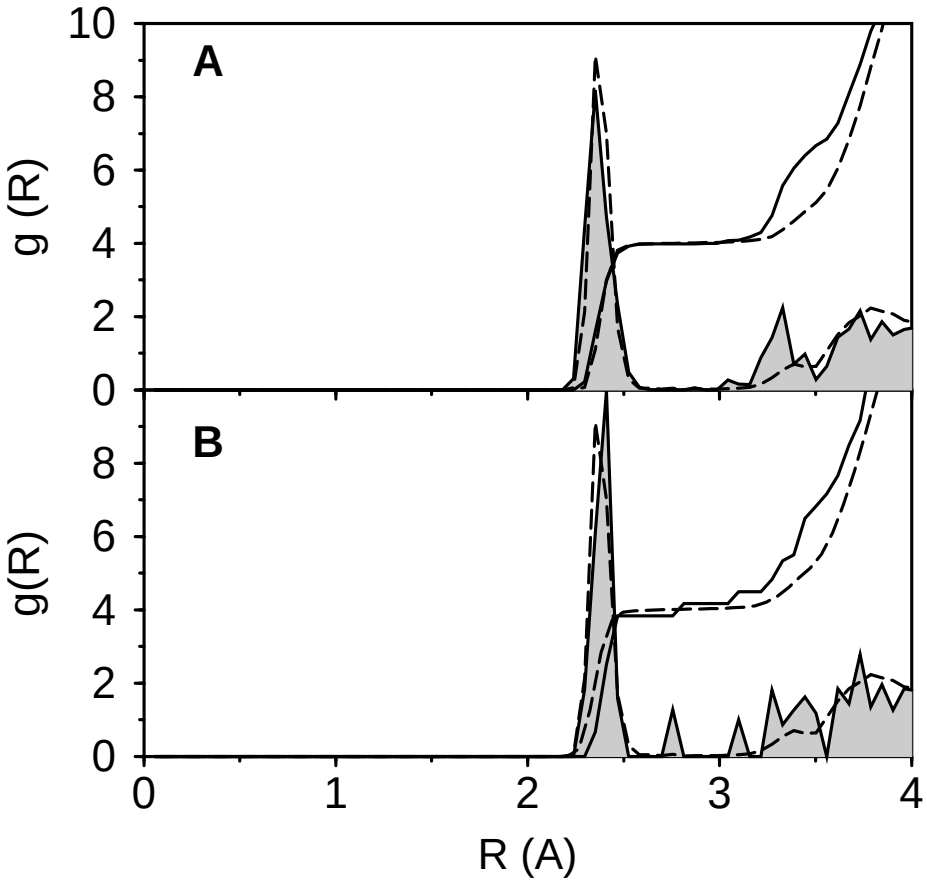

Figure 2.9: Calculated $g(R)$ for localized modes (A) and resonance modes (B). In each case only the atoms with the largest vibrational amplitude were taken as the origin atoms $R = 0$. The dashed lines show the case where all the atoms are considered.

resonance modes. The dashed lines denote the same, but averaged over the whole sample. Figure 2.9 (A) shows that the first neighbor lies closer than on average. The coordination is therefore higher for the atoms that trap localized states. For resonance states, Fig. 2.9 (B) indicates undercoordination. The first neighbor is farther than on average. However, the gap between the first and second neighbor is now partially filled. The solid line shows that the number of neighbors up to second is larger than on average. The deficiency in the distance to first neighbor is thus compensated by the number of the neighbors. This is also the reason why the undercoordination is not seen in the graph of z_i, Fig. 2.7.

Finally, the majority of vibrational eigenstates in our models are modes that are neither localized nor propagating (nor resonant). They occupy the part of the spectrum roughly between 15 meV and $\omega_c \approx 71$ meV. The properties of these modes are quite uncommon. They have no wave vector or polarization. Wave packets formed by the superposition of these modes spread out diffusively rather than ballistically. The center of the wave packet does not move: the group velocity is zero. Atomic vibrational displacements point in random directions and there is no coherence connecting the displacements in different regions of space. Locally, however, the displacements are correlated (there is still frequency distinguishing between different modes). A good measure of the short-range correlations is the *phase quotient*, introduced by Bell and Hibbins-Butler [21]

$$PQ(i) = \frac{\sum_{<a,b>} \mathbf{e}_a^i \mathbf{e}_b^i}{\sum_{<a,b>} |\mathbf{e}_a^i \mathbf{e}_b^i|}. \tag{2.13}$$

The summation is over all nearest neighbors $< a, b >$, that we take the atoms within the distance of 2.5 Å (roughly the end of the first-neighbor peak in the pair-correlation function $g(R)$ in Fig. 2.3) from each other. If the displacement of the atoms a and b is close to parallel (acoustic-like vibration), PQ would be close to 1. On the other hand, for an antiparallel displacement (optic-like vibration), PQ approaches -1. Figure 2.10 displays this behavior. Low-frequency modes have "acoustic" properties, while high-frequency modes are like optic phonons. If not for the discontinuous jump at 30 meV and the dispersion of PQ values above the mobility edge, there would be an almost linear decrease of PQ with increasing frequency. The dispersion of values for localized modes has the same origin as the dispersion of their z_i values, Fig. 2.7. As for the jump at 30 meV, this is less clear. DOS (Fig. 2.4) has a dip in this region and $1/P$ (Fig. 2.5) indicates the corresponding modes might be resonant. PQ increases by about 0.5 after the dip; the slope seems unchanged.

To simplify further discussion, we propose an improved nomenclature for the vibrational states in glasses. In a crystal, vibrations are "phonons," which are extended and propagating. Although it is common to use the term "phonon" in glasses, there is no agreement as to whether the term should be restricted to propagating states, so we prefer the generic term "vibrons" (v). Vibrons can be either localized or delocalized (in Anderson's sense [15]). For localized states we use the term "locon" (l), and for delocalized (extended) "extendon" (e). Finally, the extended acoustic-phonon-like vibrations at low energies can be assigned wavelengths, wave vectors, and velocities, and we call them "propagons" (p), as opposed to extended vibrations called "diffusons"

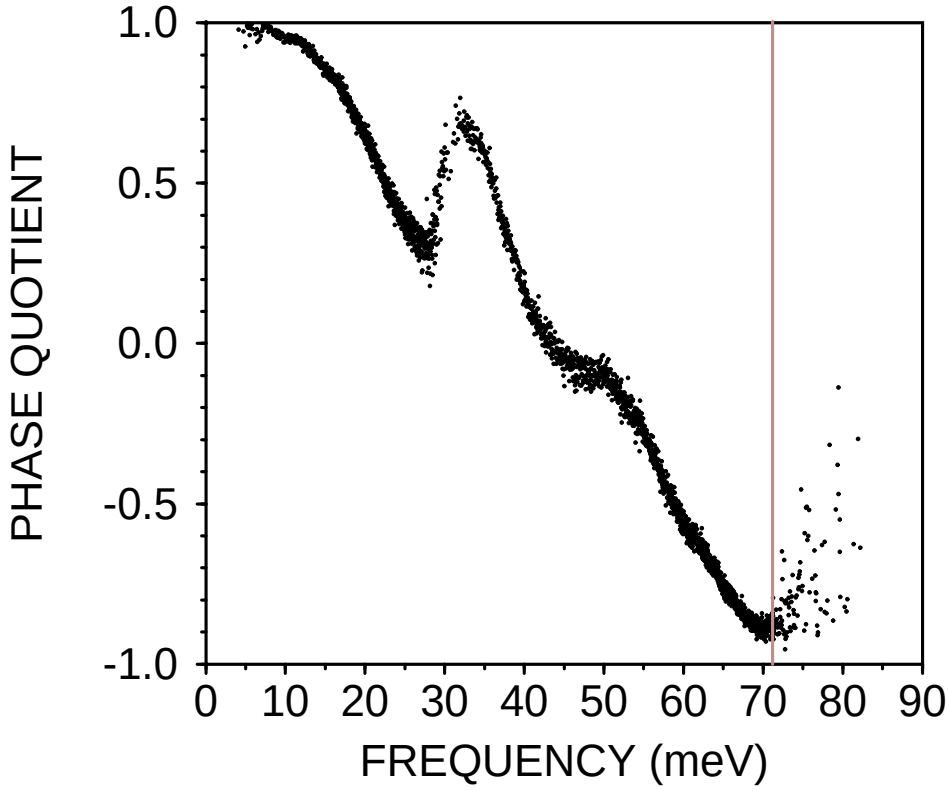

Figure 2.10: Calculated PQ for the 1000-atom model of amorphous silicon. The vertical line is the mobility edge ω_c.

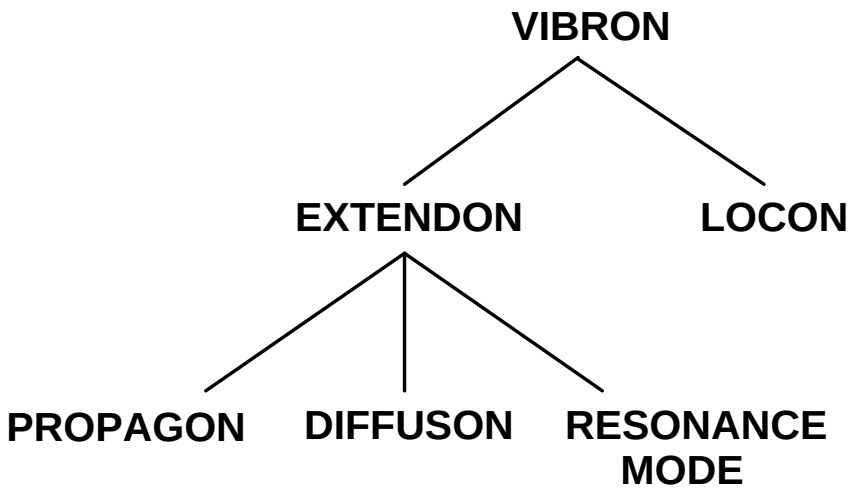

Figure 2.11: Family tree of harmonic vibrational eigenstates in glasses.

(d), which have none of these. We also include resonance modes among extendons. Resonance modes are extended with a large amplitude at groups of a small number of atoms. This nomenclature is also shown in Fig. 2.11.

Vibrational profile of selected vibrons is in Fig. 2.12. We plot the quantity $U^2(R)$, defined for mode i as

$$U_i^2(R) = \frac{\sum_a |\mathbf{e}_a^i|^2 \, \delta\left(R - |\mathbf{r}_a - \mathbf{r}_0|\right)}{\sum_a \delta\left(R - |\mathbf{r}_a - \mathbf{r}_0|\right)}. \tag{2.14}$$

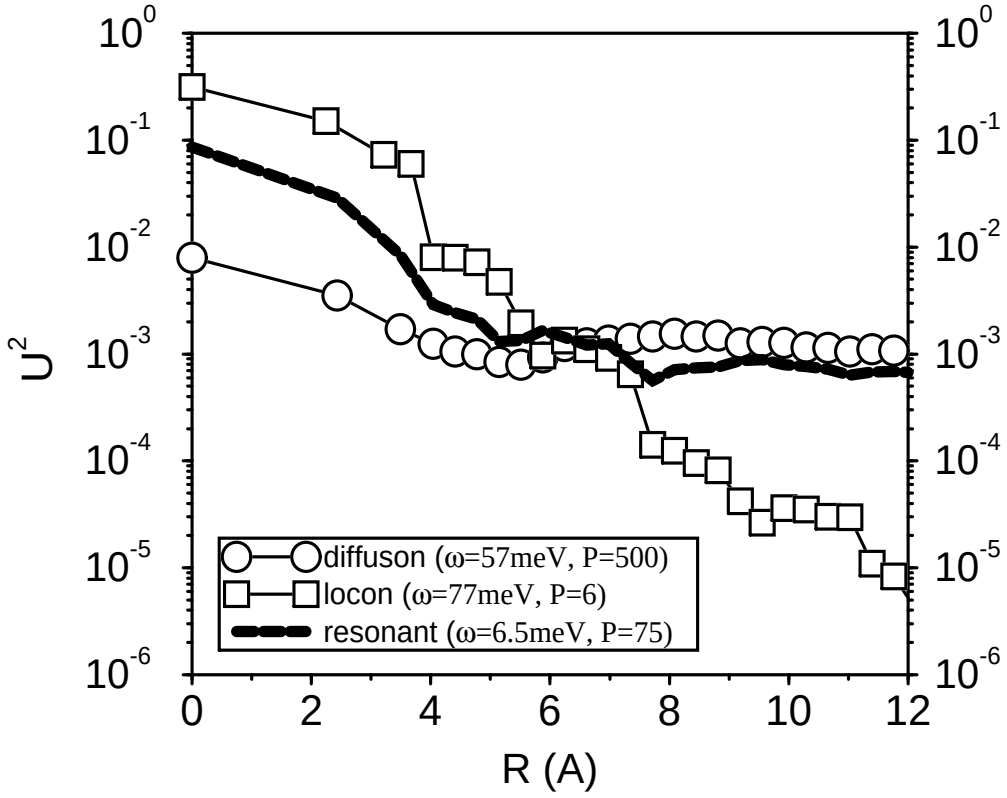

Figure 2.12: Calculated amplitude profile of selected vibrons for the 1000-atom model. The extendons (diffuson and resonance mode) have typical amplitude of $U^2 \sim 1/N \sim 10^{-3}$. The locon's amplitude decays exponentially with distance. The participation ratio P indicates at how many atoms the vibrational amplitude is highest. The lines are eye guiding only, they do not have a special meaning (our structure is discreet: there is certainly no vibrational activity between the origin and the first-neighbor atom at 2.35 Å).

Here $\mathbf{r}_0$ is the radius vector of an atom with maximum amplitude $|\mathbf{e}^i|^2$. Equation 2.14 gives an average square amplitude of a vibration at distance R from $\mathbf{r}_0$. For extendons one expects roughly constant U^2 at the value of $1/N$, while locons should have their square amplitude decaying exponentially with increasing R. This is indeed seen in Fig. 2.12. The profile of the resonance mode at ω=6.5 meV reveals that this mode has a very large amplitude at the origin atom, while its amplitude does not exponentially decay as in the case of locons.

2.3 Anharmonic Decay of Vibrational States [2]

Scholten *et al.* [11, 12] have found long relaxation times of vibrational states (VS) in amorphous silicon and hydrogenated amorphous silicon, at liquid He temperatures. Hot charge carriers produced by laser pulses excite VS during their thermal relaxation towards the conduction band edges, and the time dependence of the VS populations is measured by anti-Stokes Raman spectroscopy. Their main observations are (a) the populations of high frequency VS live about 10 ns, and (b) the relaxation times increase as the frequency increases. The situation in crystals is very different: optic phonons decay on picosecond time scales and the lifetimes of phonons typically decrease with frequency, as new decay channels become available.

Several models of atomic vibrations in glasses exist. (i) The "soft potential" model [22, 17] introduces a system of random soft anharmonic atomic

[2] J. Fabian and P. B. Allen, Phys. Rev. Lett. **77**, 3839 (1996).

potentials and accounts well for low temperature and frequency properties of glasses. (ii) The "fracton model" [10] emphasizes an assumption that, except at low frequencies, the VS in glasses are localized. (iii) The "diffuson" model [7, 8] exploits atomistic calculations which have the property that, except for at low frequencies and at very high frequencies, VS are neither localized nor propagating, but are intrinsically diffusive (see also Ref. [16]).

Until now there has been no careful numerical study of anharmonic decay in glasses. The present paper offers such a calculation which applies most directly to model (iii), but which is extended to cover model (ii) as well. It has been argued that the simplest explanation of the inhibited thermalization seen in refs. [11, 12] comes from model (ii) via an inhibition of anharmonic decay of localized states. Our calculations show that, contrary to this argument, both models (ii) and (iii) give anharmonic decay rates comparable to or faster than in crystals. There is little likelihood that model (i) can inhibit thermalization, so the experiments [11, 12] remain unexplained.

The decay rate (inverse lifetime) $2\Gamma(j)$ of the mode j with the frequency $\omega(j)$, at a temperature T, is given by [23]

$$\begin{aligned} 2\Gamma(j) &= \frac{\hbar^2\pi}{4\omega(j)}\sum_{k,l}\frac{|V(j,k,l)|^2}{\omega(k)\omega(l)}\left(\frac{1}{2}[1+n(k)+n(l)]\delta[\omega(j)-\omega(k)-\omega(l)]\right. \\ &+ \left.[n(k)-n(l)]\delta[\omega(j)+\omega(k)-\omega(l)]\right) \end{aligned} \tag{2.15}$$

Here $V(j,k,l)$ are the coefficients of the cubic terms in the expansion of the interatomic potential in normal mode coordinates, and $n(j)$ are the Bose-Einstein occupation factors $[\exp(\hbar\omega(j)/kT)-1]^{-1}$. Because of the lack of translational invariance, the VS in amorphous systems can be labeled by their

frequency only. For phonons in crystals, j denotes both the band index λ and the wave vector $\mathbf{Q}$, and the wave vector conservation up to a reciprocal lattice vector is a selection rule in $V(j,k,l)$. Two different processes are contained in this equation: (a) processes $v \rightarrow v'v''$ where a vibron splits into two with temperature factor $1+n'+n''$, and (b) processes $vv' \rightarrow v''$ where vibron v absorbs a thermal vibron v' with temperature factor $n'-n''$. Delta functions ensure energy conservation. At zero temperature only the (a) decay exists and at high temperatures the decay grows proportionally to the temperature.

As a test for the SW potential we have carried out the calculation of the decay rates $2\Gamma(\mathbf{Q}=\mathbf{0},\lambda)$ of the zone-center optic phonons in crystalline silicon. In this case only processes (a) contribute (frequencies of the **Q=0** phonons are the highest in the vibrational spectrum). The state j in Eq. 2.15 is ($\mathbf{0}$,λ), state k is ($\mathbf{q}$,λ'), and by crystal momentum conservation, not found in glasses, state l is $(-\mathbf{q},\lambda'')$. The sum goes over ($\mathbf{q}\lambda'\lambda''$) for N $\mathbf{q}$ vectors in the Brillouin zone. The matrix element $V(j,k,l)$ can be written as [23]

$$V(j,k,l)=\sum_{a,b,c}\sum_{\alpha\beta\gamma}\frac{\partial^3 V}{\partial u_{a\alpha}\partial u_{b\beta}\partial u_{c\gamma}}\frac{e^j_{a\alpha}}{\sqrt{m_a}}\frac{e^k_{b\beta}}{\sqrt{m_b}}\frac{e^l_{c\gamma}}{\sqrt{m_c}}, \tag{2.16}$$

where V is the potential energy of the system expressed in terms of the displacements from equilibrium $u_{a\alpha}$, where α identifies components and a identifies atoms, which are of mass m_a. $e^k_{b\beta}$ are normalized ($\sum_{b\beta}|e^k_{b\beta}|^2=1$) vibrational eigenvectors. For crystalline phonons $e^k_{b\beta}=\hat{e}^{\lambda'}_{b\beta}e^{i\mathbf{q}\cdot\mathbf{R}_b}/\sqrt{N}$, $\mathbf{R}_b$ being equilibrium atomic positions and $\hat{e}^{\lambda'}_{b\beta}$ polarization vectors. Since interatomic interactions are short ranged, the sum over atoms a,b,c has $\sim O(N)$ terms, with phase factors $e^{i\mathbf{q}\cdot\mathbf{R}_b}$ multiplying to 1 and adding coherently. This gives

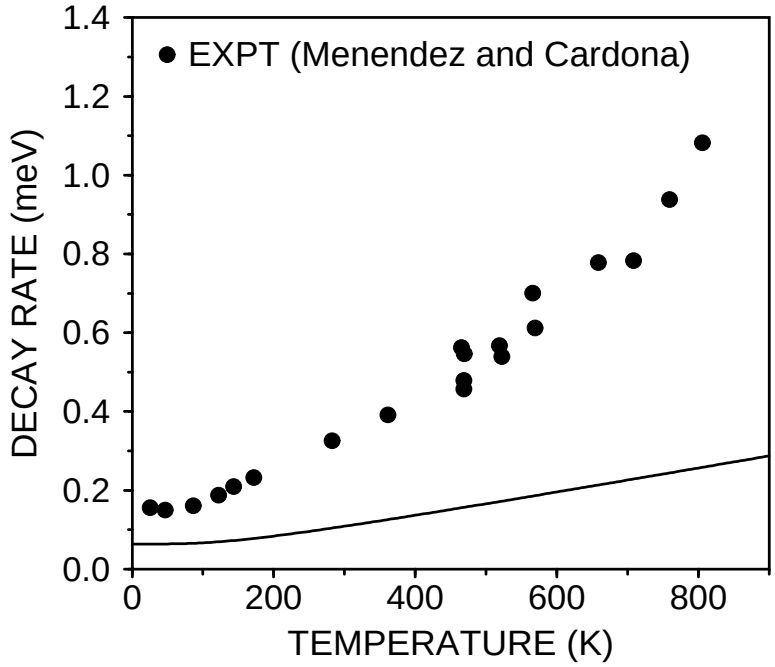

Figure 2.13: Decay rate of the zone-center optic phonons in crystalline silicon from the SW potential as a function of absolute temperature. The filled circles are the experimental points from Ref. 10.

$|V(j,k,l)|^2 \sim 1/N$ and the factor of $1/N$ cancels with the N terms in the Brillouin zone sum, giving a rate 2Γ independent of N.

To sum over the $\mathbf{q}$ points in Eq. (1) we use the tetrahedron method with 1772 tetrahedra in the irreducible wedge of the Brillouin zone. Figure 2.13 shows the temperature dependence of the decay rate along with the experimental values from Raman scattering [24]. At zero temperature our calculated decay rate is 0.064 meV, as compared to 0.153 meV obtained experimentally [24], and 0.059 meV [25] and 0.183 meV [26] obtained using the local density

approximation. Calculated decay rates are by a factor of 3 smaller than experimental values, in line with calculations of the high temperature thermal expansion [3] and pressure dependence of elastic constants [5], which are underestimated by the SW potential by less than a factor of 2. We believe that these discrepances are a quantitative detail, not important to our qualitative conclusions.

Information about the relative importance of the spectral regions to the total decay rate can be obtained from the spectral density of the decay rate. It is given in Fig. 2.14 for the off-diagonal (different polarizations of the decay products) decay processes, along with the vibrational density of states. Shown is the spectral density of the decay rate of the zone-center optic phonons. The dominant decay mechanism involves one LA and one TA mode ($\approx$93%), while the diagonal LA + LA (Klemens) channel gives a relatively small contribution ($\approx$7%). This follows from the trends in the vibrational density of states, as observed earlier [25, 26].

Because diffusons dominate the spectrum, the decay rate 2Γ is dominated by $d \rightarrow d'd''$ and $dd' \rightarrow d''$. The number of contributing terms in the sum in Eq. 2.15 is $\sim N^2$ rather than $\sim N$ as in crystals. But the extra factor of N is compensated by a matrix element $V(j,k,l)$ in Eq. 2.16 which is smaller by $1/\sqrt{N}$. This happens because the coordinates of $\mathbf{e}^j$ have the same magnitude as in crystals, but the relative phases of $\mathbf{e}^j$, $\mathbf{e}^k$, and $\mathbf{e}^l$ are random. The sum is now incoherent and thus smaller by $1/\sqrt{N}$. To confirm this incoherence, we show in fig. 2.15 the calculated distribution of anharmonic matrix elements, which is a perfect Gaussian in accord with the central limit theorem for the

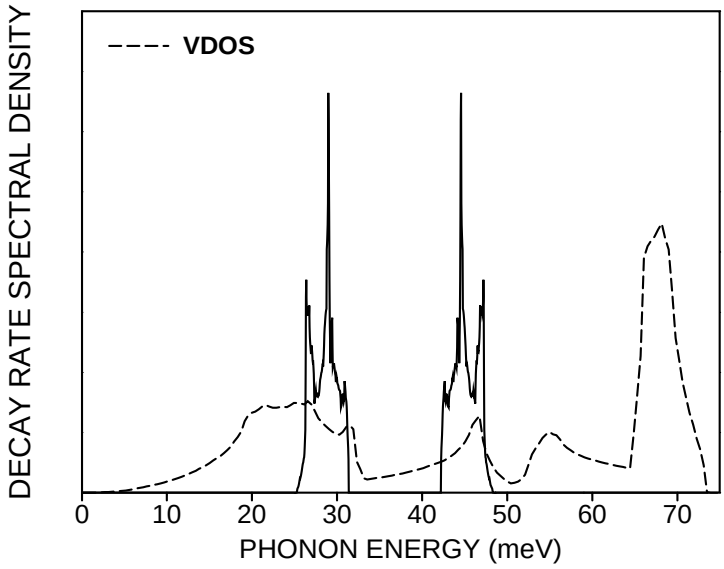

Figure 2.14: Calculated off-diagonal spectral density of the decay rate of the zone-center optic phonons in c-Si (solid line), and the vibrational density of states (dashed line).

addition of random numbers (compare with the crystalline case Fig. 2.14).

Because of the discreteness of the vibrational energy levels in our finite system, we represent the delta functions in the Eq. 2.15 by normalized rectangles of the widths 0.4 meV, centered at the frequencies $\omega(j)$. On average there are 3.6 modes in a rectangle. An increase of the rectangle widths increases the computation time without a notable change in results. Smaller values enhance the noise. In Fig.2.16 we show the calculated decay rates as frequency functions at 10 and 300 K. The curves were convolved with rectangles to suppress the remaining noise. The decay rates $2\Gamma(j)$ are of order 0.01 $\omega(j)$, which confirms the applicability of lowest order perturbation theory. For lifetimes one thus obtains picoseconds in contrast to the experimentally claimed nanoseconds [$\hbar/(1\text{ meV}) \approx 0.7$ ps]. The decay rate follows the joint two-mode density of states [$\sum_{j,k} \delta(\omega - \omega(j) - \omega(k))$] curve, even beyond the mobility edge (indicated by the vertical line). At higher temperatures the midfrequency region becomes more pronounced due to the appearance of processes (b). The high temperature shape of the decay rate frequency dependence can be shown to follow a combination of the joint and difference two-mode density of states. Compared with the decay of the optic phonons in crystalline silicon, the decay rates of the amorphous silicon VS just below the mobility edge are larger by a factor of 3. Considering the bond angle and other structural disorder in amorphous silicon, this seems reasonable.

The locons in our system kinematically decay mostly to two diffusons, $l \rightarrow d'd''$. If N_j atoms participate in the vibration of locon j, the incoherent sum Eq. 2.16 contains $O(N_j)$ terms. Since the locon eigenvector scales as

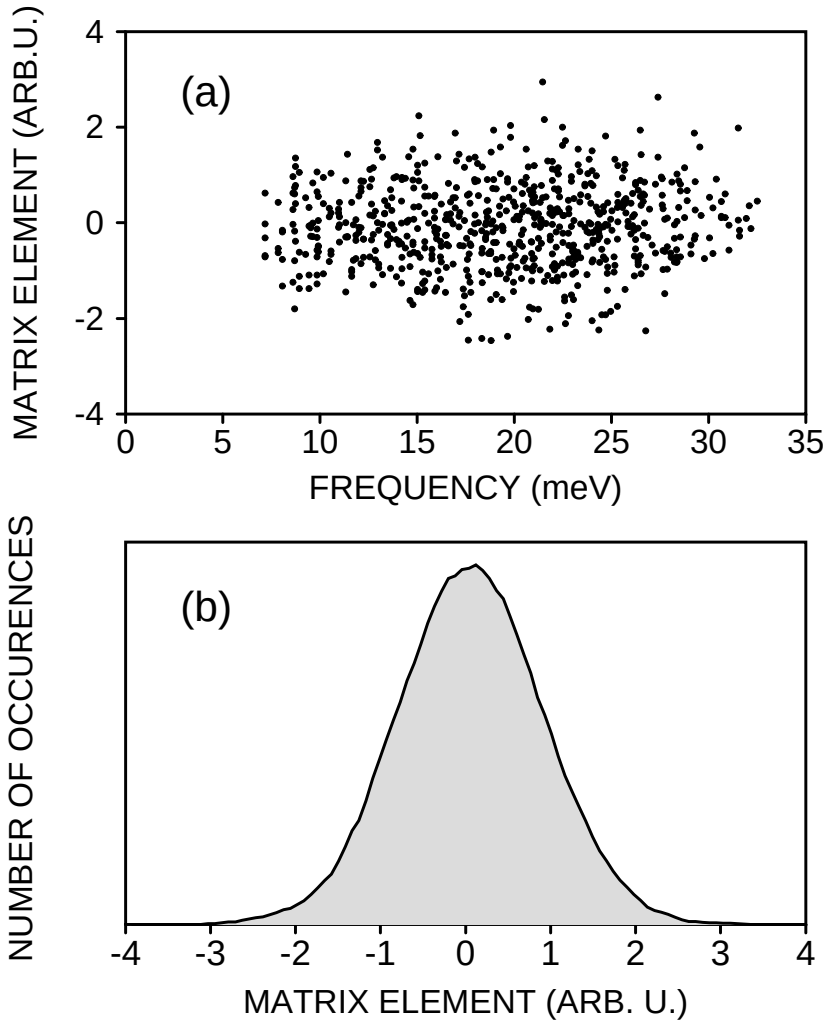

Figure 2.15: (a) Distribution of the anharmonic matrix elements $V(j,k,l)$ for the decay of a sample of three extendons j of $\omega(j)$ between 65 and 68 meV. The horizontal frequency axis is the lower frequency of the two final states k and l; the other frequency is given by the energy conservation $\omega(j) = \omega(k)+\omega(l)$. (b) The number of occurences of the anharmonic matrix elements from (a) shows their Gaussian random character due to lack of selection rules other than the energy conservation.

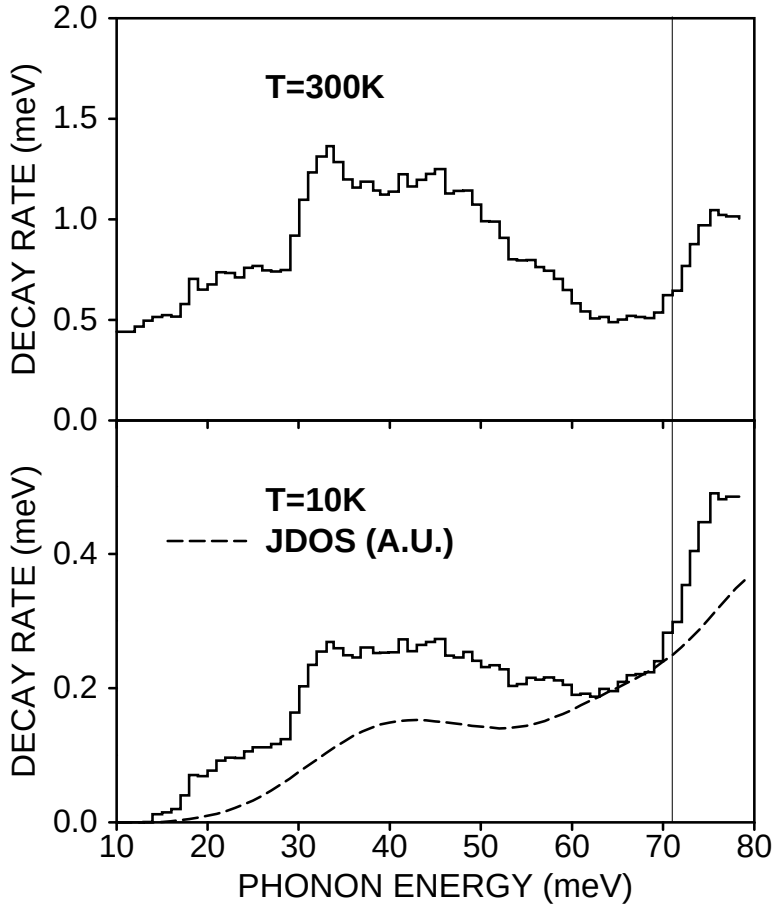

Figure 2.16: Anharmonic decay rate of VS in amorphous silicon as a frequency function for temperatures 10 and 300 K. The dashed line in the low temperature graph is the joint two-mode density of states in arbitrary units and the vertical line indicates the mobility edge $\omega_c \approx 71$ meV.

$e^j_{a\alpha} \sim 1/\sqrt{N_j}$, the terms containing N_j cancel and $|V(j,k,l)|^2 \sim 1/N^2$, as for the decay of diffusons. This explains our result that beyond ω_c no qualitative changes in 2Γ occur.

We now ask what changes would occur in decay rates if a greater proportion of the states were localized. To accomplish this we model a hypothetical alloy of silicon and heavy germanium (amorphous Si/Ge) by changing the masses of 50% of the atoms chosen at random, to twice the germanium mass. The interatomic potential is unchanged. Harmonic vibrational properties of this systems were studied [8], and it was shown that the mobility edge shifts down to 31 meV. The extrinsic mass disorder increases the portion of locons. Figure 2.17 shows the decay rate frequency functions at two temperatures, 10 and 300 K. The mobility edge is indicated by the vertical line at 31 meV. Again, there are no dramatic changes beyond the mobility edge, the curves basically follow the trends in the joint, and the joint plus the difference two-mode density of states. Modes with frequencies above 62 meV are like the modes of the fracton model (ii), as their decay to two extendons is kinematically forbidden. Calculations based on the "fracton" model with the assumption that the decay to two other locons is negligible lead to the exponential decrease of the decay rates in this frequency region. We do not find any evidence for such a behavior. On the contrary, the decay rates further increase. The following argument shows that the assumption of negligible three locon interaction (and the prediction of the decrease of the decay rates with increasing frequency) is not correct. A detailed version of it will be given elsewhere [27].

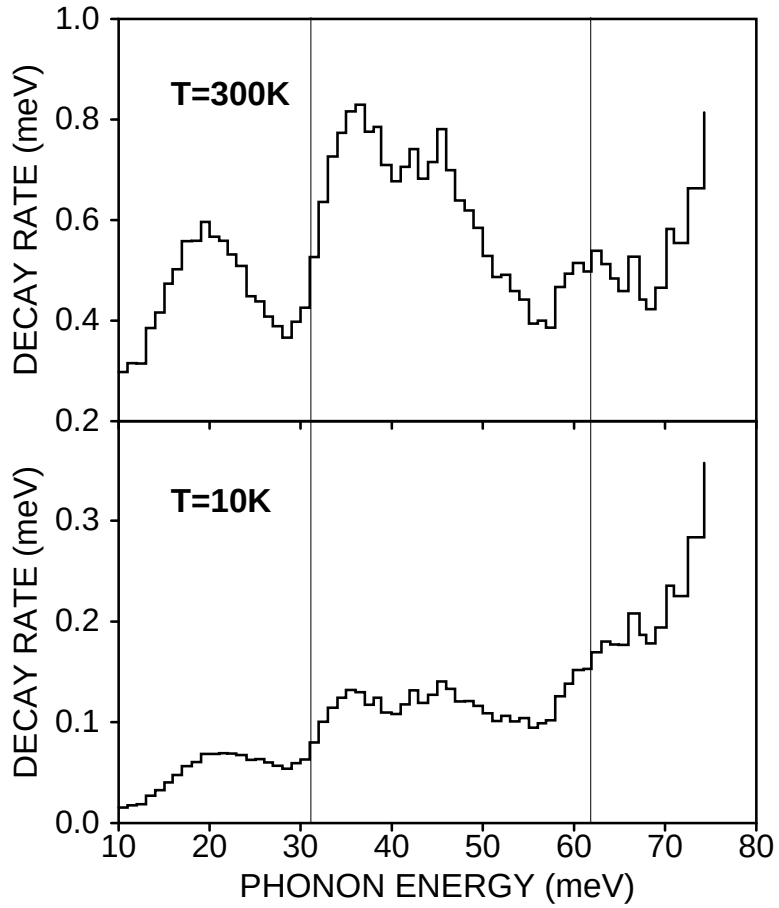

Figure 2.17: Anharmonic decay rate of VS in hypothetical (see text) amorphous Si/Ge as a frequency function for temperatures 10 and 300 K. The vertical line at 31 meV indicates the mobility edge ω_c. According to the calculations based on the fracton model, the modes with frequencies above 62 meV (second vertical line) would decay more slowly with increasing frequency.

A key observation is that when most states are localized, then locons are no longer dilute. Consider processes $l \rightarrow l'l''$, $ll' \rightarrow l''$. Let N_j atoms participate in the vibration of a locon j, similarly N_k and N_l for locons k and l. The matrix element Eq. 2.16 is nonzero only when the three locons overlap. Whenever the locon j lies within the overlap of the locons k and l, the scaling arguments give $|V(j,k,l)|^2 \sim 1/N_k N_l$. The overlap occurs with the probability $\sim N_k N_l/N^2$, since the modes come from different frequency regions and their localization centers are uncorrelated. The *average* value of $|V(j,k,l)|^2$ for these processes is then $\sim 1/N^2$, of the same order as for the processes $d \rightarrow d'd''$, $dd' \rightarrow d''$, and $l \rightarrow d'd''$. The same results can be deduced also for $l \rightarrow d'l''$, $ld' \rightarrow l''$ (one of the participation numbers is set to N), unless the two locons come from the same frequency region, where the localization centers repel. In the "fracton model" extendon frequencies are much smaller than those of locons, so $|\omega_l - \omega_{l''}|$ is small for states participating in $l \rightarrow e'l''$ or $le' \rightarrow l''$. Thus repulsion occurs and (if $l \rightarrow l'l''$ and $ll' \rightarrow l''$ are neglected) only long-range e-assisted hopping occurs. Estimates of the magnitudes of the hopping processes are given in Ref. [10], where it is shown that the hopping decay probabilities decrease with decreasing N_j.

In conclusion, we have found that the high-frequency VS in a realistic model of amorphous silicon decay on picosecond time scales, and at low temperatures their lifetimes decrease as frequency increases. This is in contrast to recent experimental claims that the modes decay on nanosecond scales and their lifetimes increase as frequency increases. We have also shown that contrary to previous ideas the interaction involving three localized modes is

important for the decay of these VS. We remark that in the experiment the average (nonequilibrium) population of the excited VS is $\overline{n}(j) \approx 0.2$ and the VS are excited over the whole spectrum [12]. However, decay rates $2\Gamma(j)$, Eq. 2.15, are defined for *small* deviations of *single-frequency* VS populations from equilibrium. It is not clear that the experiment measures the same rates.

2.4 Decay of Localized Modes in Low-Mobility-Edge Glasses [3]

In harmonic approximation the VS will never equilibrate, but anharmonic interactions are always present. What is the rate of equilibration in glasses? Experiment [11, 12] indicates that at a liquid He temperature in a-Si (a) high frequency ($\omega \geq 10$ meV) VS live longer as frequency increases, and (b) the VS live on nanosecond time scales. In contrast, phonons in crystals decay faster as frequency increases (the number of decay channels increases), and lifetimes are picoseconds. Model (i) seems to agree with the experiment in the following way. Locons l can decay via three processes: (1) $l \rightarrow p'p''$, (2) $l \rightarrow p'l''$ or $lp' \rightarrow l''$, and (3) $l \rightarrow l'l''$ or $ll' \rightarrow l''$. Process (1) is kinematically forbidden for high frequency locons with $\omega_l > 2\omega_{\rm IR}$. Processes (2) represent "propagon-assisted hopping" between locons l and l''. Because $\omega_{p'} \ll (\omega_l, \omega_{l''})$, $\omega_l \approx \omega_{l''}$, and the locons l and l'' spatially repel each other [28]. As the frequency and the inverse localization legth L^{-1} increases, the overlap between the locons

[3] J. Fabian, Phys. Rev. B **55**, R3328 (1997).

decreases and so does the hopping rate. Processes (3) have been neglected by model (i) on the grounds of a small probability of three-locon overlap. Hopping is therefore assumed to be the only locon decay process, and because it has property (a) and can be adjusted to fit (b), the experiment [11, 12] seems to be rationalized.

Recent numerical calculations on models (i) and (ii) ([27], see Sec. 2.3) have shown that decay properties of both diffusons and locons are similar to those of crystalline phonons. It has been argued [27] that the assumption of the negligibility of (3) is incorrect and is the reason behind the discrepancy between the numerical results and model (i) predictions. The experiment [11, 12] therefore remains to be explained. In this section we show, using a one-dimensional (1D) numerical realization of model (i), that extended and localized modes decay on the same time scale and that the three locon interaction is dominant in the decay of locons with $\omega \geq 2\omega_c$.

Consider a linear chain of N uniformly spaced atoms connected by random springs [29, 30]. Periodic boundary conditions are assumed. In terms of displacements u_a ($u_{N+1} \equiv u_1$) of atoms a from equilibrium, the potential energy of the system can be expressed as

$$V = \frac{1}{2}\sum_{a=1}^{N} K_a(u_a - u_{a+1})^2. \tag{2.17}$$

Here K_a=$K_0(1+\xi_a)$, where ξ_a are random numbers uniformly distributed in the interval $< -b, b >$, and K_0=10.6 eV/Å^2 is chosen to simulate a hypothetical linear silicon chain (the silicon atom mass M) with maximum vibrational frequency $\omega_{\max} = 2\sqrt{K_0/M} \approx 80$ meV in the case of no disorder ($b = 0$). The

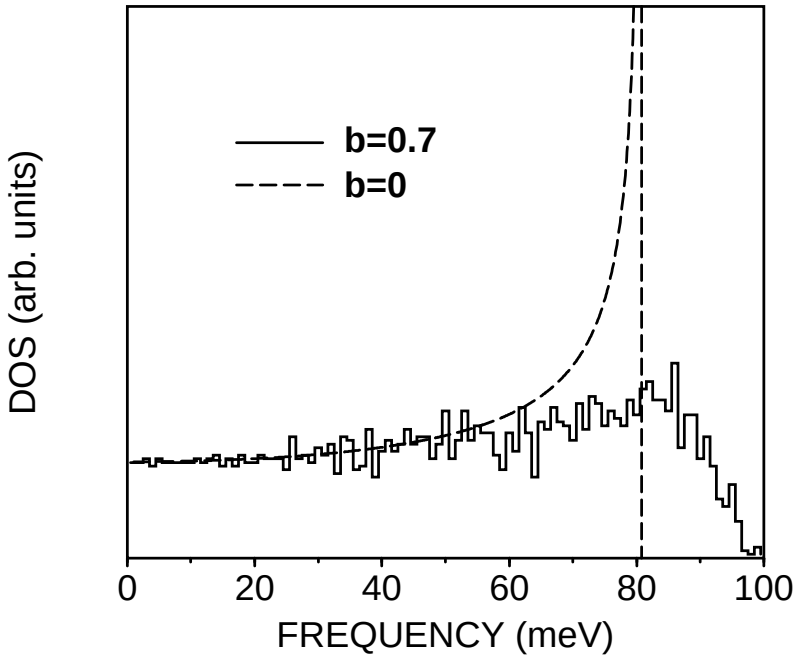

Figure 2.18: Calculated DOS for the 3000-atom linear chain with the spring constant disorder of $b = 0.7$ (solid line) and $b = 0$ (dashed line).

length scale is the interatomic spacing, the exact value of which is not important here. For the case $N = 3000$, vibrational eigenstates and frequencies were found by exact numerical diagonalization. This number is sufficiently large to ensure that the conclusions will not be affected by finite size effects. The goal is to numerically realize the "fracton model" scenario with a majority of VS localized. As shown later, the strong disorder value $b = 0.7$ suits this purpose and will be used from now on. The "clean" case, $b = 0$, will serve as a reference.

Figure 2.18 shows the vibrational density of states (DOS) for the above

model and for the case $b = 0$. The latter can be trivially solved by introducing wave vectors. Consequently its DOS has the $1/\sqrt{\omega_{\max}^2 - \omega^2}$ dependence and a van Hove singularity at $\omega_{\max}$. As the disorder increases, the description of VS in terms of wave vectors is less and less valid. For $b = 0.7$, the van Hove singularity is washed out and DOS becomes nearly flat.

In a 1D infinite system any disorder causes all VS to be localized [31], with a trivial exemption for the zero-frequency mode corresponding to a translation of the system as a whole. However, if N is finite there are always low-frequency modes with L larger than the system size. They appear to be extended, sound-wave-like modes, although on intermediate time scales they behave as diffusons [32]. Only after the system size is increased, they become manifestly localized. A good measure of the number of atoms participating in the vibration of mode i is the participation ratio P_i. Its inverse is defined as

$$1/P_i = \sum_{a=1}^{N} (e_a^i)^4, \tag{2.18}$$

where e_a^i are normalized $[\sum_a (e_a^i)^2 = 1]$ vibrational eigenstates with frequencies ω_i. we plot $1/P$ in Fig. 2.19. $1/P$ grows monotonously with frequency, the dependence being close to quadratic for $\omega \geq 10$ meV. At lower frequencies $1/P \approx 1/N$, since $L \geq$ system size (for infinite N it has been predicted [33] that $1/P \sim \omega^2$ as a result of 1D elastic sound-wave scattering). To accurately locate the mobility edge ω_c we use the Thouless criterion [34], that $\Delta\omega/\delta\omega$ should exhibit a sharp drop at ω_c. For a given mode, $\Delta\omega$ is the locally averaged change of the mode frequency under the change of boundary conditions from periodic to antiperiodic, and $\delta\omega$ is the local average level spacing. we find it

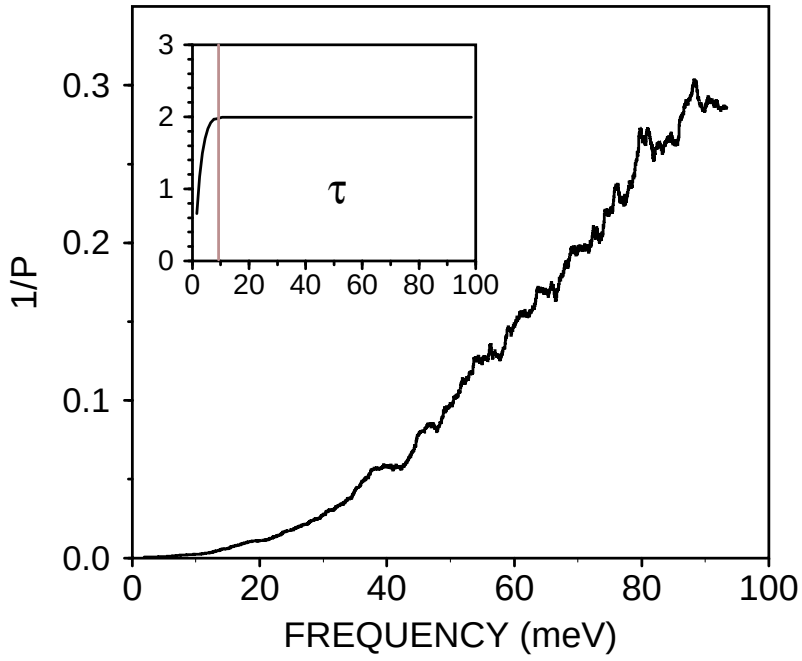

Figure 2.19: Inverse participation ratio $1/P$ and the cumulative Thouless number τ (inset) as a function of frequency. The vertical line in the inset is the mobility edge $\omega_c \approx 9$ meV.

convenient to consider the cumulative quantity $\tau(\omega) = \int_0^\omega d\omega' \Delta\omega(\omega')/\delta\omega(\omega')$, which is plotted in the inset of Fig. 2.19. The mobility edge (vertical line) is $\omega_c \approx 9$ meV and $\Delta\omega/\delta\omega$ at ω_c is less than 1%. Locons with $\omega \geq \omega_c$ form $\approx 90\%$ of the spectrum, enough to simulate model (i).

To get a qualitative understanding of how VS decay, consider a simplified version of zero-temperature decay rate formula (full formula see, e.g., Ref.

[23]),

$$\tilde{\Gamma}_i = \sum_{j,k} (J_{ijk})^2 \delta(\omega_i - \omega_j - \omega_k), \tag{2.19}$$

where the sum is over all modes j and k, and

$$J_{ijk} = \sum_a \eta_a e_a^i e_a^j e_a^k \tag{2.20}$$

measures the overlap between modes i, j, and k. η_a is a binary random variable having values 1 or -1. Only "fission" decay processes ($i \rightarrow jk$) are allowed at zero temperature. "Fusion" processes ($ij \rightarrow k$) appearing at finite temperatures will not be considered here, since they can be handled analogously. In 1D VS have a partial memory of a wave vector, and therefore a partial phase coherence. The reason is that the nth vibrational eigenstate has $n-1$ nodes (if the zero-frequency mode is $n = 1$) [29]. η_a is inserted into Eq. 2.20 to eliminate this coherence, so that the results will not be substantially affected by dimensionality (apart from the DOS effects). Imagine VS with amplitudes independent of frequency. Then an expression similar to Eq. 2.19 can be obtained for the decay of the VS caused by a set of nonlinear springs with potentials $\sim \eta_a u_a^3 + \mathrm{O}(u_a^4)$, externally attached to each atom.

The spectral dependence of $\tilde{\Gamma}$ is shown in Fig. 2.20. The case $b = 0$, plotted in (b), does not represent the decay of 1D crystalline phonons, since the phases of these are randomized by η_a in Eq. 2.20. It, however, shows the hypothetical behavior of random-phase *extended* modes, such as occur below the mobility edge in 3D. The ω variation of $\tilde{\Gamma}$ follows the joint density of states (JDOS), $\sum_{jk} \delta(\omega_i - \omega_j - \omega_k)$, and provides a benchmark when discussing the

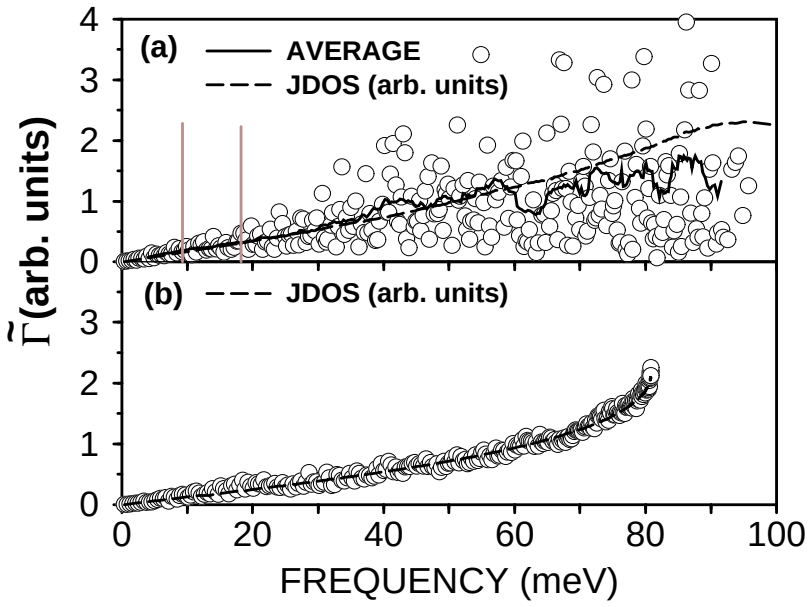

Figure 2.20: Calculated $\tilde{\Gamma}$ (circles represent uniformly sampled one-tenth of data) for $b = 0.7$ (a) and $b = 0$ (b). Scattered data in (a) are represented by their running averages (solid line). Vertical lines indicate ω_c and $2\omega_c$, and dashed lines are JDOS. Units are arbitrary, though the same in (a) and (b).

decay behavior of locons. Data in (a) at $\omega \geq \omega_c$ are much more scattered than in (b), since the locon decay involves some overlap statistics (explained below). Therefore, local averages are used to represent the data. $\tilde{\Gamma}$ in (a) increases with frequency and follows JDOS, having similar magnitudes as in (b). According to model (i) there would be a sharp decrease in $\tilde{\Gamma}$ beyond 2 ω_c. This certainly does not happen.

The reason why the behavior of $\tilde{\Gamma}$ differs from the one predicted by model (i) is that processes (3) can not be neglected. In fact they are dominant decay processes for high-frequency locons. Consider a decay $i \rightarrow jk$, where i, j, and k are locons with corresponding participation numbers P_i, P_j, and P_k. Eq. 2.19 can be rewritten as $\tilde{\Gamma}_i = \int\int d\omega_j d\omega_k N(\omega_j) N(\omega_k) J_i^2(\omega_j, \omega_k) \delta(\omega_i - \omega_j - \omega_k)$, where $N(\omega_j)$ is the total number of states at ω_j, and $J_i^2(\omega_j, \omega_k)$ is J_{ijk}^2 averaged over frequency shells of ω_j and ω_k. A simple scaling argument [27] shows that $J_i^2(\omega_j, \omega_k)$ does not explicitly depend on P_i, P_j, or P_k. It goes as follows. The maximum decay magnitude among J_{ijk}^2 is found when i lies entirely within an overlap of j and k, and scales as $1/P_j P_k$ ($e_a^i \sim 1/\sqrt{P_i}$, etc., and the sum in Eq. 2.20 is over P_i random-sign numbers and scales as $\sqrt{P_i}$). The probability for this overlap to occur scales as $P_j P_k / N^2$. An important assumption used here is that locons i, j, and k, having different frequencies, are spatially uncorrelated (illustrated below). The average $J_i^2(\omega_j, \omega_k)$ therefore scales as $1/N^2$ and $\tilde{\Gamma}_i$ is N independent (and follows the JDOS). The small probability of the three-locon overlap is exactly compensated by the large magnitudes of decay matrix elements, when the overlap occurs. As for hopping processes $l \rightarrow p'l''$, one has to distinguish between two cases. If $\omega_{p'} \ll \omega_l, \omega_{l''}$ [as in model (i) and this

paper], the two locons l and l'' spatially repel each other [28] and the decay rates decrease as L of l and l'' decreases. On the other hand, if $\omega_{p'}$ is not small, one can apply the above scaling arguments, since the majority of l and l'' are not spatially correlated. Decay rates of this "uncorrelated" hopping are therefore independent of the localization character of VS involved and follow the JDOS. When a low-frequency ($\omega_l \leq 2\omega_c$) locon decays into two propagons, $l \rightarrow p'p''$, the overlap probability is 1 ($P_j, P_k = N$) and the case is trivial, similar in behavior to three locon and uncorrelated hopping processes. These arguments do not depend on dimension and worked, as far as one could tell, in 3D also [27].

Figure 2.21 illustrates the foregoing discussion. Data are represented by running averages. Decay $l \rightarrow l'l''$ in (a), obtained by considering only j and k with ω_j, $\omega_k \geq \omega_c$ in Eq. 2.19, dominates the high frequency region and grows monotonously with frequency. When, on the other hand, restricting, say, modes j to be propagons ($\omega_j \leq \omega_c$), one gets hopping $l \rightarrow p'l''$ which decreases as frequency is increased. Since ω_c is large enough to allow hopping between locons from different spectral regions, the decrease is quite moderate. The graph (b) in Fig. 2.21 shows hopping when propagon frequency is restricted by $\omega_p \leq 1$ meV. Computed rates are scattered over several magnitudes. In a sample of decay rates of locons confined into a small frequency band (of the width, say, 1 meV), the majority have negligible values, but there are $\leq 10\%$ of large magnitude rates giving rise to large local averages (they come from a residual overlap between locons with similar frequencies). As the graph shows, local medians sharply decrease with increasing frequency and deviate strongly

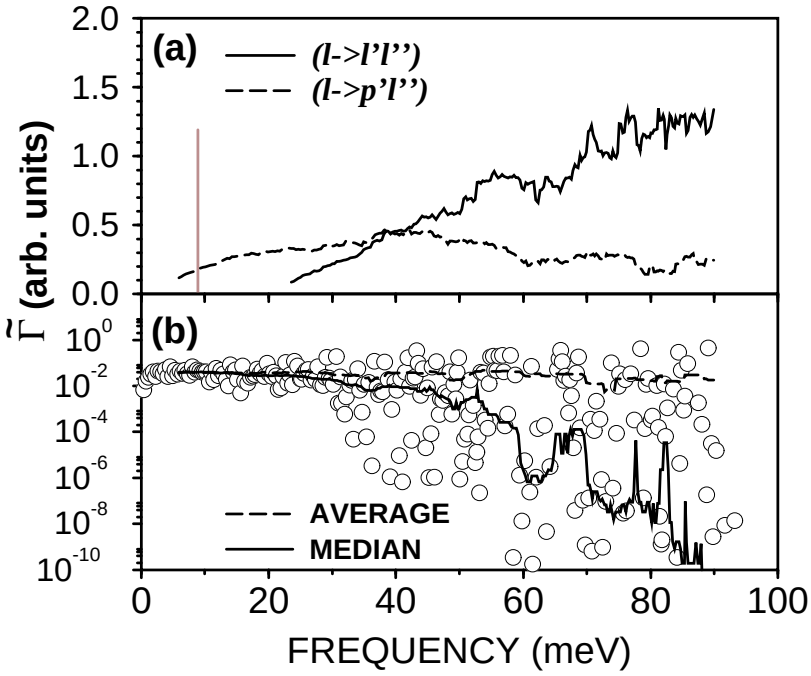

Figure 2.21: Calculated $\tilde{\Gamma}$ (a) for the three-locon (solid) and hopping (dashed) decay processes, and (b) for hopping between locons from the same frequency region (circles—see caption to Fig. 2.20). Vertical line in (a) indicates ω_c. Units are the same as in Fig. 2.20.

from local averages. Since the local distribution of decay rates is found to have a strong central tendency around small values (the area in the tails is small), the medians better represent computed data. For other decay types local medians and averages are similar.

Finally, we present figure 2.22 to support the argument that locons from different spectral regions are spatially uncorrelated, as opposed to locons with similar frequencies, which repel each other. $N = 1000$ is used for this purpose. The spectrum is divided into δ=1 meV wide bands, each band containing 10 VS on the average. For every mode i in a band only atoms a having $(e_a^i)^2 \geq 0.2\ (e_{\max}^i)^2$ are shown, $e_{\max}^i$ being the largest magnitude found among the coordinates of the vector $\mathbf{e}^i$. Localization starts somewhere beyond 15 meV, where fewer than P $\approx$ 200 atoms participate in the vibration. There is clearly no statistically relevant overlap between the locons lying within a frequency band. On the other hand, locons from different spectral regions show no sign of repulsion; their spatial positions are essentially uncorrelated.

One may ask how the above results depend on the degree of disorder. we have made calculations similar to those above, with different values of b (up to almost $b = 1$). we found the foregoing conclusions valid for all the studied cases, the only effect of the increase in b being the increase of the spread of the calculated $\tilde{\Gamma}$. This happens because by increasing b, L decreases, as does the number of the decay events, and the overlap statistics gets worse.

In summary, we have used a 1D random spring atomic model to demonstrate that the interaction including three locons is important for the locon decay processes. we have shown that extended mode and locon decay rates have

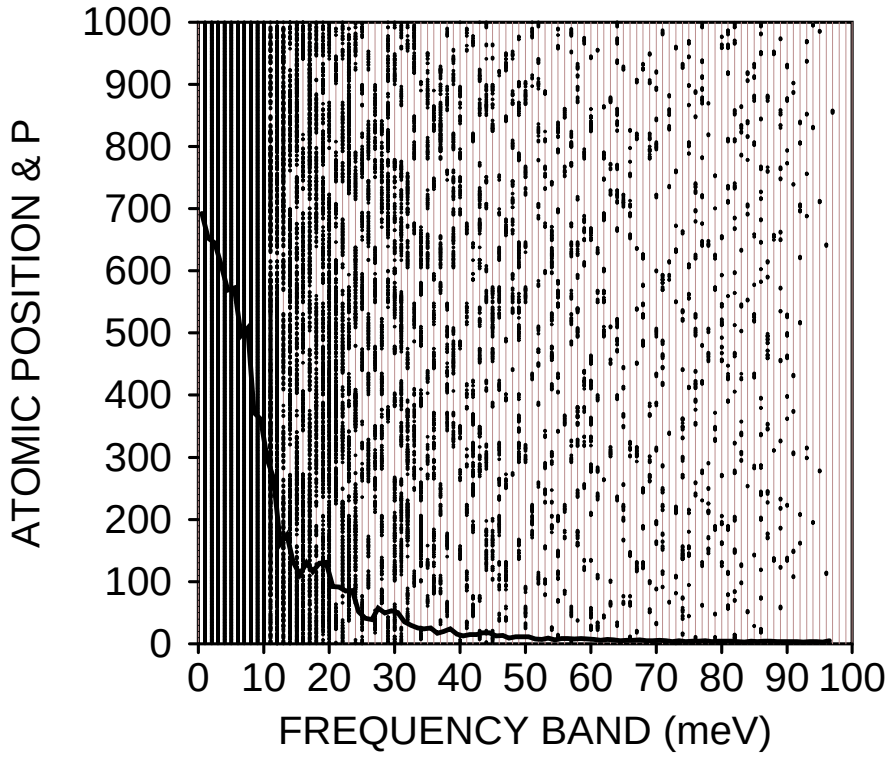

Figure 2.22: Localization of VS in the 1000-atom linear random spring model. For each mode only the atoms vibrating with amplitudes higher than a certain value (see text) are shown. The solid line is the particiation ratio P.

similar magnitudes, increasing with increasing frequency and closely following JDOS. Hopping decay rates decrease as frequency increases; the decrease is sharper as the frequency difference of hopping locons gets smaller.

2.5 Grüneisen Parameters and Thermal Expansion [4]

Unlike thermal conductivity and specific heat, which have "universal" features, thermal expansion is a special property of each glass. The coefficient of linear expansion α can be either positive or negative, with magnitude sensitive to sample preparation methods [35]. This is true even at very low temperatures ($T \leq 1$ K), where α is believed to be associated with tunneling modes [22, 36] and large dispersion of γ values is found [37].

Here we present an analysis of $\alpha(T)$ for an atomistic model of amorphous silicon, an important electronic material. The value of $\alpha(T)$ has been measured only at $T = 383$ K [38], making theoretical modeling particularly useful. Our calculation shows that the value of $\alpha(T)$ is lower than that of crystalline silicon. Deviations from the crystalline values are more dramatic at lower temperatures, and are caused by volume driven internal strain, which makes the thermal expansion sample dependent. The predicted Grüneisen parameters display a surprising simplicity, which we interpret as evidence for special, possibly generic, properties of vibrations in glasses. Specifically, we find that the

[4] J. Fabian and P. B. Allen, Phy. Rev. Lett. (in press)

majority of modes which are neither localized nor ballistically propagating (we call them "diffusons"), have a property of *global indistinguishability*, whereas high-frequency localized and low-frequency resonant modes are distinguished by the special structural imperfections at which they have largest amplitudes. In particular, the resonant modes have a considerable dispersion of γ values (from -31 to 4), consistent with our finding that internal strain is largest at the centers of these modes. Below 1 K, very large average magnitudes of γ ($|\gamma| \geq 10$) were measured in many glasses [37] ("normal" values are about one). Although the size of our model does not allow us to go as low as 1 K, we show that the resonant modes provide a likely origin of this anomaly. Finally, we establish a close link between the mode Grüneisen parameters and the mode bond-stretching character.

Insofar as a complete set of normal modes can be defined (i.e., the modes decay on time scales much larger than their periods), one expects vibrational entropy S to be well approximated by $S = k_B \sum_i [(n_i+1)\log(n_i+1) - n_i \log n_i]$, where $n_i = (\exp(\hbar\omega_i/k_BT) - 1)^{-1}$ is the average equilibrium occupation number of the mode of frequency ω_i, i being a counting label going from 1 to $3N$. N is the number of atoms and k_B is the Boltzmann constant. The frequency $\omega_i(V,T)$ may depend on both volume V and temperature. Using the standard thermodynamic relation $3\alpha = \kappa_{\rm T}(\partial S/\partial V)_T$, with isothermal compressibility $\kappa_{\rm T}$, we get (see, e.g., Ref. [39])

$$\alpha(T) = \frac{\kappa_{\rm T}}{3V} \sum_i c_i \gamma_i. \tag{2.21}$$

Here $c_i = k_B(\hbar\omega_i/k_BT)^2 n_i(n_i+1)$ is the specific heat of a harmonic oscillator,

and γ_i, given by $\gamma_i = -\partial \log \omega_i / \partial \log V$, are known as the "mode Grüneisen parameters"; they measure how sensitive the vibrational eigenfrequencies are to the change of volume. Their knowledge is essential not only for $\alpha(T)$, but also for the interpretation of the internal friction and sound attenuation experiments [40, 41] (see also Sec. 2.6).

Perturbation theory (see, e.g., Ref. [42]) gives the following formula for γ_i,

$$\gamma_i = -\frac{1}{6\omega_i^2} \sum_{abc} \sum_{\alpha\beta\gamma} \Phi^{abc}_{\alpha\beta\gamma} \frac{e^{i*}_{a\alpha} e^i_{b\beta}}{\sqrt{M_a M_b}} (r_{c\gamma} + \bar{r}_{c\gamma}), \tag{2.22}$$

$$\bar{r}_{a\alpha} = -\sum_i \frac{1}{\omega_i^2} \sum_{bc} \sum_{\beta\gamma} \Phi^{bc}_{\beta\gamma} \frac{e^{i*}_{a\alpha} e^a_{b\beta}}{\sqrt{M_a M_b}} r_{c\gamma}. \tag{2.23}$$

Here $\Phi^{ab}_{\alpha\beta}$ ($\Phi^{abc}_{\alpha\beta\gamma}$) are the coefficients of the quadratic (cubic) terms of the Taylor expansion of potential energy in terms of the displacements $u_{a\alpha}$ of atoms a from equilibrium in the direction $\alpha = (x, y, z)$, and $r_{a\alpha}$ is the position vector of the ath atom. The vibrational eigenvectors $e^i_{a\alpha}$ are normalized ($\sum_{a\alpha} |e^i_{a\alpha}|^2 = 1$), and M_a is the mass of atom a. The sums in Eq. 2.22 and 2.23 are over all atoms. Because of periodicity, in a crystal the label i can be written as ($\mathbf{Q}$,λ), denoting wave vector and polarization. The eigenvectors $e_{a\alpha}(\mathbf{Q}, \lambda)$ are proportional to $e^{i\mathbf{Q}\cdot\mathbf{r}_a}/\sqrt{N}$, and the resulting crystalline phase coherence allows a simplification of the sum in Eq. 2.22 to the neighborhood of a single small unit cell. By contrast, normal modes in a glass have no *a priori* quantum numbers, and quantitative insight is best achieved by numerical diagonalization for finite models.

If a solid is subject to an infinitesimal homogeneous isotropic strain ϵ, its atomic coordinates change to $r'_{a\alpha} = r_{a\alpha}(1 + \epsilon)$, and volume to $V' = V(1 + 3\epsilon)$.

Unless atoms in the solid are fixed by symmetry, $r'_{a\alpha}$ are not the equilibrium coordinates of the solid with volume V'. This happens in glasses. After the strain is applied, the atoms relax to new equilibrium positions $r'_{a\alpha} + \epsilon \bar{r}_{a\alpha}$. This is the origin of the *internal strain* (Eq. 2.23) occurring during the thermal expansion of glasses (and crystals with atoms not in centers of symmetry [35]). In silicon crystal $\bar{r}_{a\alpha} \equiv 0$.

To calculate $\alpha(T)$ we need the values for κ_{T}. The corresponding perturbation formulas for κ_{T}, which take into account internal strain, can be found in Ref. [43]. We obtain the value 1.13×10^{-12} cm^2/dyn for the present model of amorphous silicon. For crystalline silicon, the SW potential gives the value of 0.986×10^{-12} [44], agreeing well with the experimental value of 1.02×10^{-12} [44]. Also, for silicon crystal, we must sum over the $\mathbf{Q}$ points, which we do using the tetrahedron method with 1772 tetrahedra in the irreducible wedge of the Brillouin zone. The results are shown in Fig. 2.23, together with the measured data.

Compared with experiment [45], $\alpha(T)$ of silicon crystal is reproduced very well at $T \geq$200 K. At lower T the SW potential does not reproduce the observed negative values of α. Negative α has been successfully explained [46] by negative values of γ for the low energy transverse acoustic (TA) branch. As shown in Fig. 2.24, our γ values are too weakly negative in this regime. In Fig. 2.23 it is predicted that $\alpha(T)$ for amorphous silicon is somewhat lower than $\alpha(T)$ for the crystal. For comparison, Fig. 2.23 also shows $\alpha(T)$ without considering internal strain ($\bar{r}_{a\alpha}$ in Eq. 2.22 is set to zero), and the calculation based on a 216 atom model of amorphous silicon. Internal strain reduces the

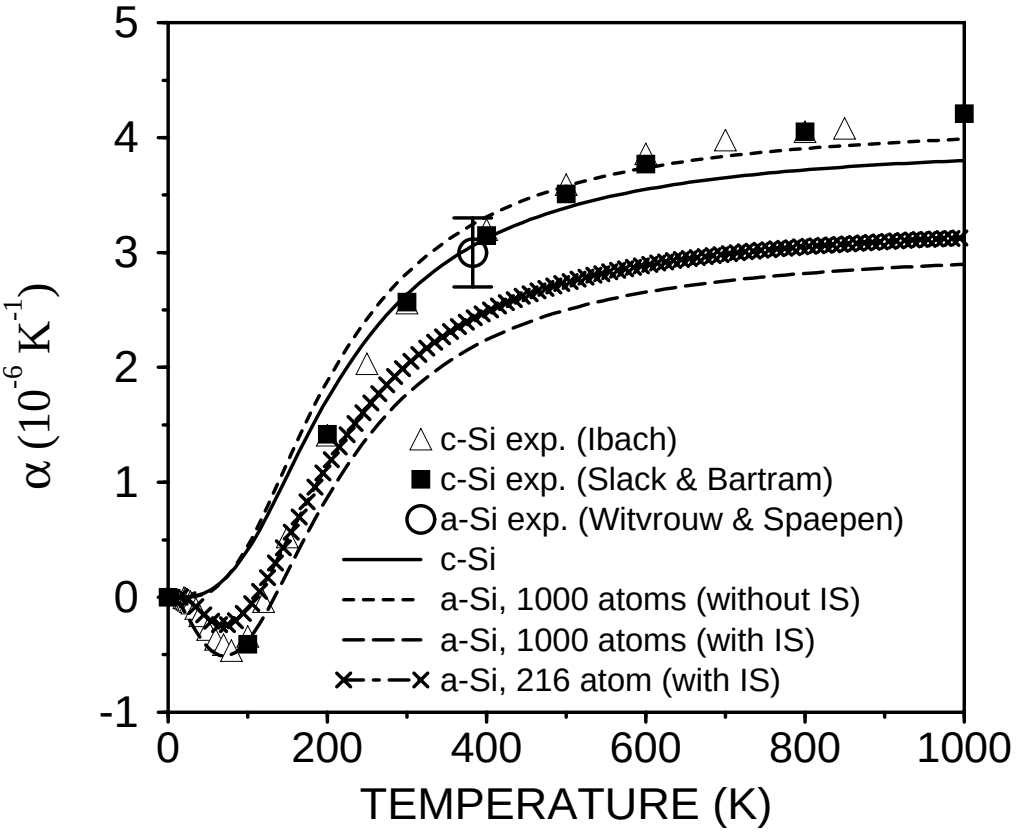

Figure 2.23: Calculated and measured linear thermal expansion $\alpha(T)$ for crystalline and amorphous silicon. IS: internal strain.

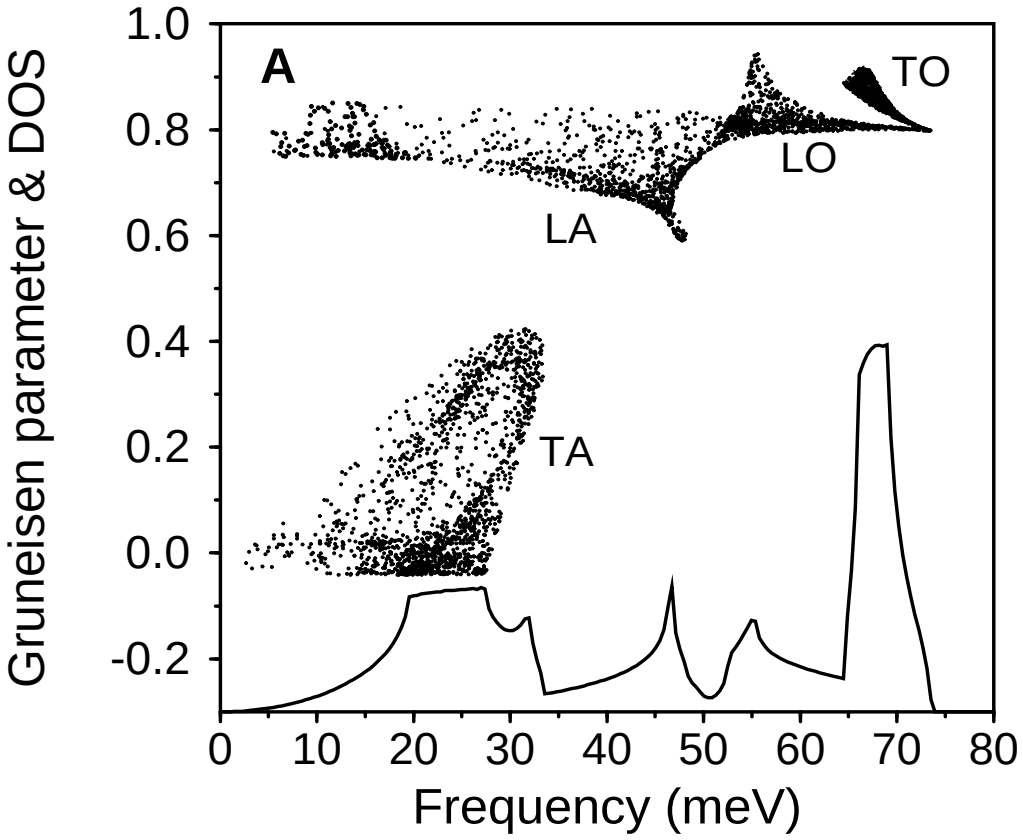

Figure 2.24: Calculated Grüneisen parameters γ_i for crystalline silicon as a function of frequency. The polarization labels are: TA−transverse acoustic, LA−longitudinal acoustic, LO−longitudinal optical, TO−transverse optical. The solid line is the vibrational density of states (DOS) in arbitrary units.

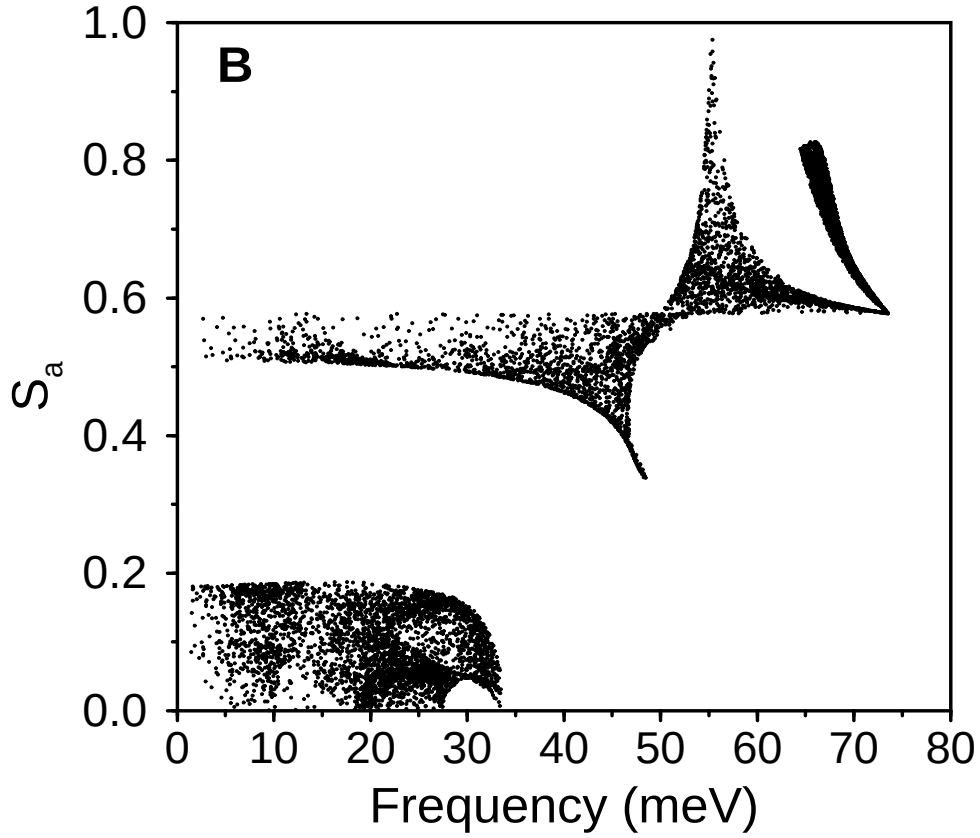

Figure 2.25: Calculated bond stretching parameters S_i for crystalline silicon as a function of frequency.

values of α by almost 30% at high T. At lower T the values become negative. The model dependence is also clear. The 216 atom model is based on the same WWW algorithm and SW potentials, but is more topologically constrained (e.g., no four-fold rings are allowed), and has lower energy/atom (by $\approx 0.5\%$) and higher density (by $\approx 3\%$) than the 1000 atom model. Its $\alpha(T)$ is higher and closer to the crystalline case and the measured value. This is not surprising. Measurements on silica [35, 47] showed that annealing history (or density) markedly changed its thermal expansion at all temperatures. For example, pure SiO_2 aged at 1400°C and quenched, has $\alpha(T)$ at high T lower by up to 50% than that slowly aged at 1000°C. Our calculation predicts that future experiments should see similar behavior in amorphous silicon as well.

To understand the behavior of $\alpha(T)$ one has to look at the frequency dependence of Grüneisen parameters. The values of γ for silicon crystal, for more than 1000 randomly chosen $\mathbf{Q}$ points from the irreducible wedge of the Brillouin zone, are in Fig. 2.24. Since there is a degenerate surface in $\mathbf{Q}$ space for a given ω, $\gamma(\mathbf{Q}, \lambda)$ has a distribution of values at each ω. These values are further split according to the branch λ of corresponding phonons. Particularly striking polarization effects appear at low ω, where TA phonons form a distinct broad band of γ_i.

It is instructive to compare Fig. 2.24 with Fig. 2.25, where we plot the mode bond-stretching parameter S_i,

$$S_i = \left[\frac{\sum_{<a,b>} |(\mathbf{u}_a^i - \mathbf{u}_b^i) \cdot \mathbf{n}_{ab}|^2}{\sum_{<a,b>} |\mathbf{u}_a^i - \mathbf{u}_b^i|^2} \right]^{\frac{1}{2}}, \tag{2.24}$$

introduced in Ref. [48] (we modified slightly the original formula which did

not yield the same S_i for different but degenerate i). The summation is over all atom pairs $< a, b >$, where b is within 2.8 Å (the distance where the first nearest neighbor peak in the pair correlation function of amorphous silicon ends [14]) from b, and $\mathbf{n}_{ab}$ is the unit vector in the direction of the bond $< a, b >$. When S_i is close to one, mode i is mostly bond-stretching, while values closer to zero indicate bond-bending modes. The similarity between the two figures is striking. Except at very low ω, one is tempted to write "$\gamma_i \approx$ const $\times$ S_i." The reason for such close relation is that anharmonicity, reflected in γ_i, is much greater in the bond-stretching part of the interatomic interaction than in the bond-bending part.

We now discuss the behavior of γ_i in amorphous silicon, whose vibrational states were discussed earlier [8, 27]. At low frequencies ($\leq$ 15 meV) the modes are *propagons*, acoustic-phonon-like vibrations propagating ballistically for distances greater than their wavelength. Some of the propagons are resonantly trapped at certain places in the sample, with reduced amplitude elsewhere (but not exponential decay as in a localized state); but at high ω there is no continuum of extended states to decay into, and vibrational amplitudes decay exponentially with distance. Properties of these resonant modes were studied in different glassy systems [17, 49], and for our model will be reported elsewhere [50]. Modes between 15 meV and 71 meV are *diffusons*, extended states carrying energy diffusively. Since they form the majority of the spectrum, diffusons dominate the thermal properties of amorphous silicon at temperatures from several kelvins up to the melting point. Above $\omega_c \approx 71$ meV, the mobility edge, the modes are *locons*, localized states.

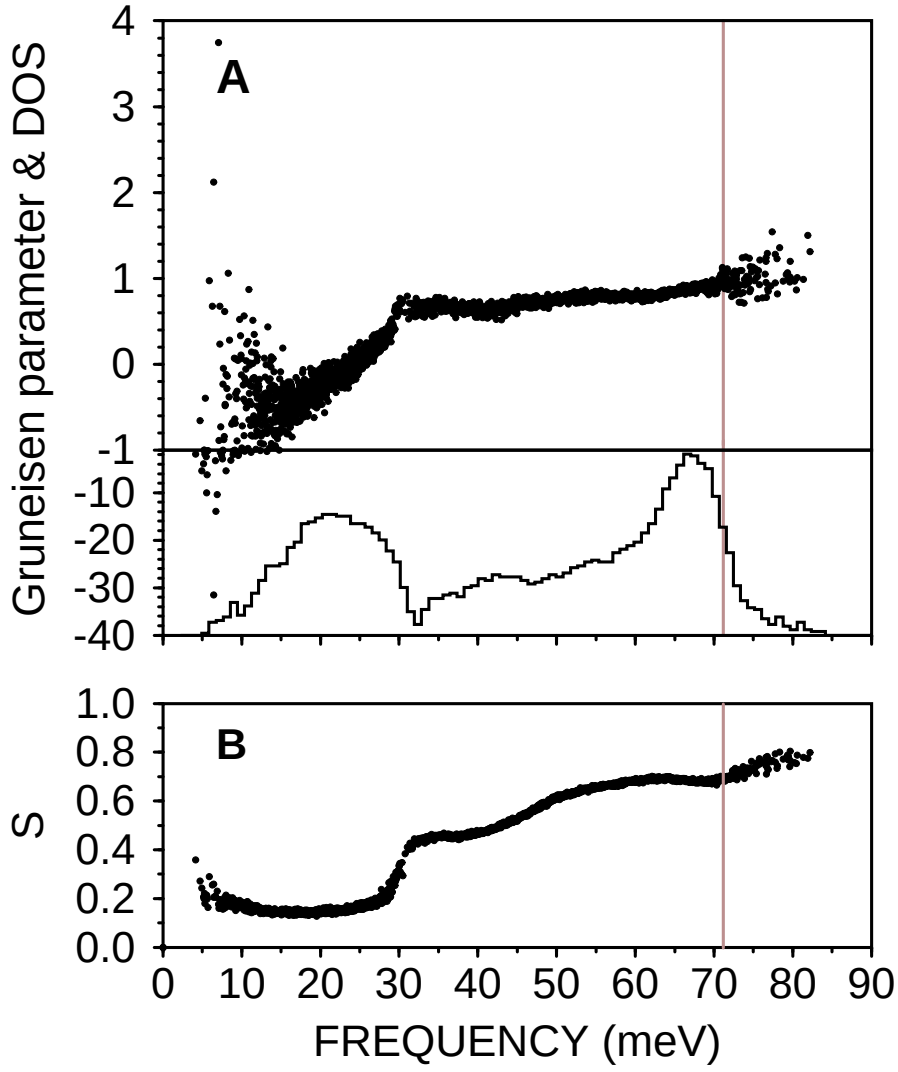

Figure 2.26: Calculated Grüneisen parameters γ_i (A) and bond-stretching character S_i (B) of amorphous silicon as a function of frequency. The vertical line at $\omega_c \approx 71$ meV is the mobility edge. The scale in (A) is split by the horizontal line at -1 to emphasize the large negative values of γ at low ω. The solid line is DOS in arbitrary units.

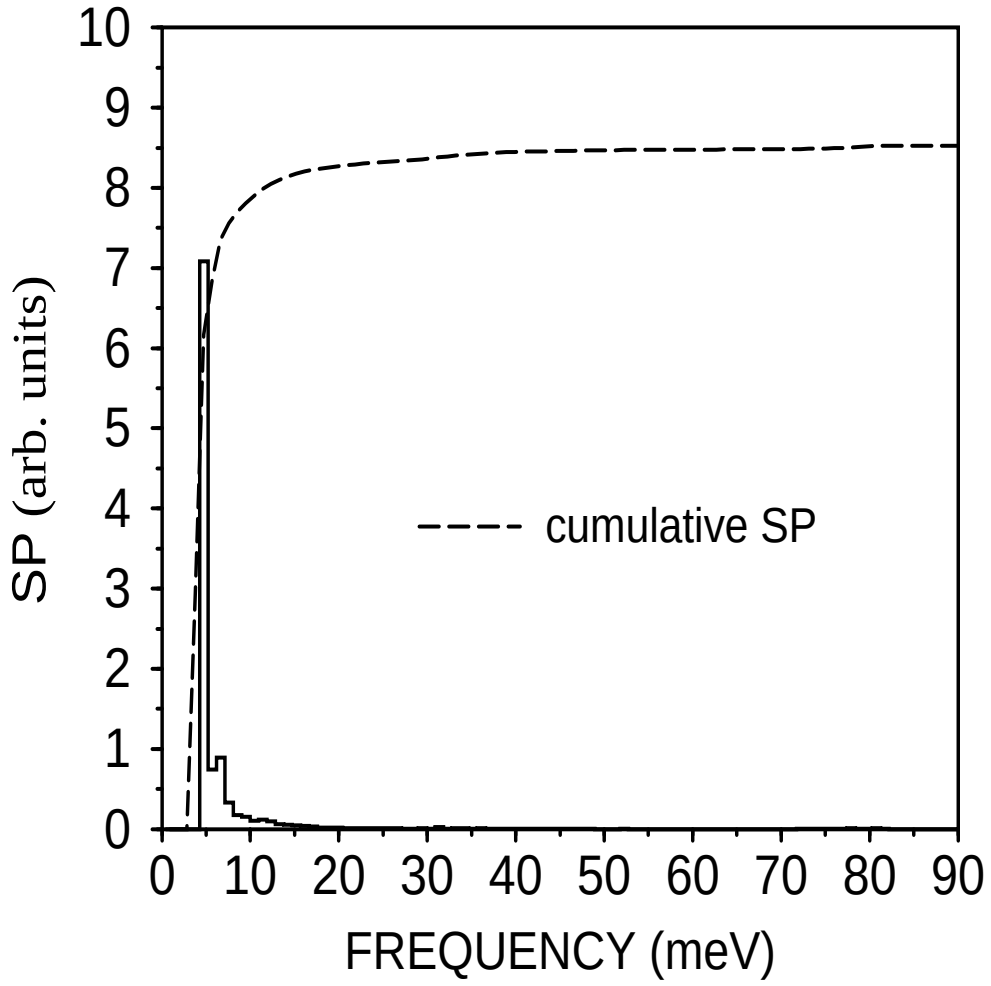

Figure 2.27: Spectral power SP_i of internal strain $\bar{r}$. Almost all the spectral weight is in the region of small-frequency resonance modes.

The calculated γ_i are shown in Fig. 2.26(A). Three regions can be clearly distinguished. (i) At low frequencies the values are very scattered, unusually large, and mostly negative. (ii) In the region of diffusons, after a monotonous increase, γ_i becomes almost constant at $\approx$30 meV, and its values collapse into a very narrow region. (iii) At locon frequencies γ_i spreads out again, but much less than at low ω.

Why are the low frequency values of γ so large? At most one would expect the data to be scattered between 0 and 1 due to a partial presence of $\mathbf{Q}$ and λ for propagons. We find that the cause of this anomalous behavior is the resonant modes. As already shown [17, 49] (see also Sec. 2.2), these modes have very large amplitudes at groups of undercoordinated atoms. Similar groups of overcoordinated atoms are responsible for locons. Since undercoordination implies "softness", it is natural that the internal strain $r_{i\alpha}$ is also largest at these sites. (Figure 2.27 shows the spectral power $SP_i = |\sum_a \bar{\mathbf{r}} \cdot \mathbf{e}_a^i|^2$, confirming the above assertion that internal strain is correlated with resonance modes.) This is why the magnitudes of γ are large for the resonant modes. The dispersion of values, also seen for locons, is explained by different nature of topological defects where the modes have largest amplitudes.

The bands seen in $\gamma(\mathbf{Q}, \lambda)$, Fig. 2.24, of crystalline silicon, are suppressed in the "diffuson" portion of the spectrum of amorphous silicon. This has the following interpretation. In a crystal, knowledge of the pattern of a normal mode in a few adjacent unit cells allows one to predict the pattern in distant regions. In a glass, such a prediction is not possible without a very large computer calculation. More surprising, different normal modes in the "diffuson"

part of the spectrum are not globally distinguishable. If one knows the pattern of displacement of two modes ($i1$ and $i2$) of similar frequencies in one spatial region, one could not recognize which pattern was $i1$ and which $i2$ in a distant region. There seem not to be properties other than ω_i which can classify these modes.

Finally, Fig. 2.26(B) shows S_i for amorphous silicon. Note the surprising uniformity of bond-stretching character (see also Ref. [48]), even in the region of propagons where memory of polarization character might have been expected. As in the crystalline case, S_i closely follows γ_i, except at low frequencies where the values of γ are much more influenced by dynamics than by vibrational pattern.

2.6 Work In Progress

This section is an eclectic selection of topics that are still under investigation, but are already in the stage of yielding some results. The first topic deals with the possibility of describing diffusons ("the most random" vibrational modes as for their displacement pattern) by random matrix theory. In a sense such a study is overdue. Random matrix theory is a developed subject and is manifested to be useful in many areas of physics. Vibrational states in models of glasses have been studied for many years. And to make the connection, one needs to know only the frequencies of the modes! Many other properties of disordered systems have been scrutinized. In particular the behavior of electrons in random media have been a playground for random

matrix theorists for long time. In short, our study indicates that diffusons are indeed random-matrix-like eigenstates, although at large (spectral) scales the random matrix theory predictions deviate from our observations. In addition, we show that locons have a completely different spectral statistics—the Poisson one. Their neighboring frequencies are uncorrelated as one expects for modes with very small spatial overlap.

Another interesting subject treated here is the sensitivity of the vibrational frequencies to boundary conditions. Originally this sensitivity was used to determine the mobility edge (localized wavefunctions are insensitive to what happens at the boundaries). Thouless pointed out that the knowledge of $\Delta\epsilon_i$, the change of electronic energies ϵ_i under the change of periodic to antiperiodic boundary conditions, suffices for the evaluation of diffusivities of electronic wavefunctions in random media. This feature is attractive since one does not need to know the actual wavefunctions to establish properties like conductivity! We show that similar ideas apply in glasses. Diffusivity, originally calculated within the framework of the Allen-Feldman theory with the need of all the vibrational eigenmodes, can be quite reasonably reproduced by using the Thouless simple scheme.

The last topic we treat is internal friction and sound attenuation. Many experimental data are available on this subject, but there is no theory to explain them satisfactorily. Some progress has been made at low temperatures $T < 1$ K, where the standard tunneling model accounts for many observations. At higher temperatures the situation is much more complicated. Tunneling modes can still contribute, but the largest contributions come from both struc-

tural relaxation and coupling of thermal vibrons to sound waves. The latter is expected to dominate at very high frequencies (≥ 100 GHz). Here we develop a basic theory of the vibrational contribution, starting from a Kubo formula. Momentum current operator is found from Hamiltonian and connection with Grüneisen parameters is made. Formally the result is in agreement with a formula obtained by a Boltzmann-like treatment of a phonon gas.

2.6.1 Random Matrices and Vibrations in Glasses [5]

Random matrix theory (RMT) sounds as a natural tool to study glasses. Glassy structures have some degree of randomness (in amorphous silicon it is the bond-length fluctuations) which should be reflected in the properties of their structural dynamics (e. g., the force-constant matrix $F_{a\alpha,b\beta}$, Eq. 2.7, is "random" as it reflects the random distribution of bond angles). So far the focus of random-matrix theorists was in the properties of electronic wavefunctions in disordered systems. Many original results were obtained, in particular in the region of metal-insulator (localization-delocalization) transition [51]. One can study vibrational dynamics, elaborate on the still mysterious two-level systems, which are thought to have randomly distributed parameters, or investigate the distribution of local or global structural configurations (a nice attempt to study various structural effects in glasses at low temperatures by using RMT has been made recently by Kühn and Horstmann [52]). The established (in this section) connection between RMT and vibrations in glasses

[5] J. Fabian and J. L. Feldman (unpublished).

shows a possibility of an analytical model for the latter.

Amongst different vibrons in glasses, diffusons are most likely to be associated with RMT. Diffusons have no wave vector, i. e., no phase coherence connects vibrational displacements at distinct spatial regions (global indistinguishability, see Sec. 2.5) as it is for phonons. Moreover, the atomic displacements are in random directions. The only property that distinguishes between different diffusons is their frequency, reflected in the preserved *local* correlations between atomic displacements (see Sec. 2.2).

In order to see whether or not diffusons can be described by RMT, we only need an ordered set of their frequencies (note that the case of vibrations is not typical; diagonalizing $F_{a\alpha,b\beta}$ results in ω_i^2 not in ω_i). RMT states that spacings S between neighboring frequencies (level-spacing distribution, LSD) are distributed according to the Wigner surmise (see, e. g., Ref. [53]) [6]

$$\rho_W = \frac{\pi}{2} S \exp(-\frac{\pi S^2}{4}). \tag{2.25}$$

The Wigner distribution ρ_W reflects level repulsion in spectra: small spacings have a small probability of occurrence. We have to note that the spacings S are *not* the spacings one obtains from the "raw" set of frequencies. Instead, S result from the procedure known as *unfolding* [53]. If DOS is not constant, level spacings are smaller in the regions of larger DOS, and vice versa. By unfolding, one maps the original spectrum onto an ordered set of numbers with constant DOS.

[6] The Wigner surmise holds for the Gaussian Orthogonal Ensemble (GOE) of real symmetric matrices, such as $F_{a\alpha,b\beta}$.

Figure 2.28 shows the calculated LSD for the 4096-atom model. Only the diffusons from 45 to 65 meV were analyzed. The solid line is the prediction of GOE: the Wigner surmise ρ_W. Agreement between model calculation and RMT is excellent. The level repulsion reflected in the small probability of finding two diffusons very close to each other now means a small probability of degeneracy. It is not surprising that degeneracy is inhibited in the region of diffusons: there is no symmetry (like discreet translations in crystals) in glasses. Locons, on the other hand, show no signs of level repulsion. Figure 2.29 plots LSD for the locons of the 4096-atom model. The result agrees very well with the Poisson distribution

$$\rho_P = \exp(-S). \tag{2.26}$$

This means that neighboring levels of locons are uncorrelated, and there is a large probability of finding two locons with similar frequencies. The reason is that locons with similar frequencies repel each other spatially. If they would overlap, a small perturbation would mix them together to form a more extended state. Since spatially repelling locons share different regions in space, their energies are hardly correlated.

Another useful property of a set of eigenvalues is $\Sigma_2(L)$, measuring deviations from average, of the number of levels $n(L)$ in a spectral interval L (not to be confused with the system size):

$$\Sigma_2(L) = \langle n^2(L) \rangle - \langle n(L) \rangle^2. \tag{2.27}$$

The averaging $\langle ... \rangle$ is over the selected set of unfolded frequencies. The GOE

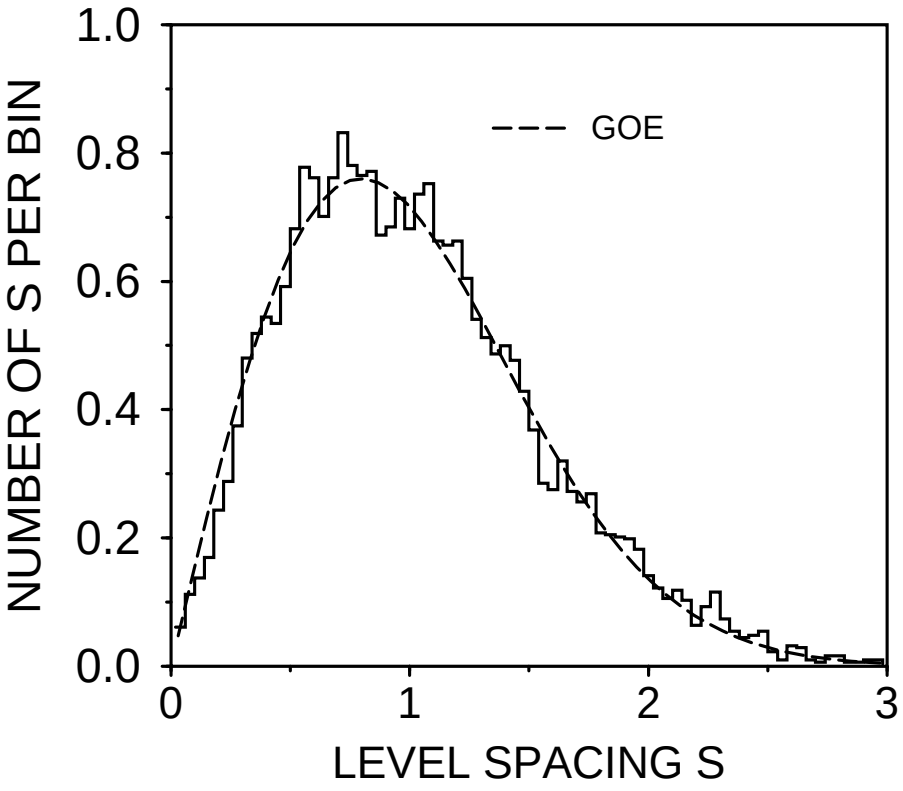

Figure 2.28: The level-spacing distribution for the 4096-atom-model diffusons with ω between 45 and 65 meV. The dashed line is the Wigner surmise ρ_W.

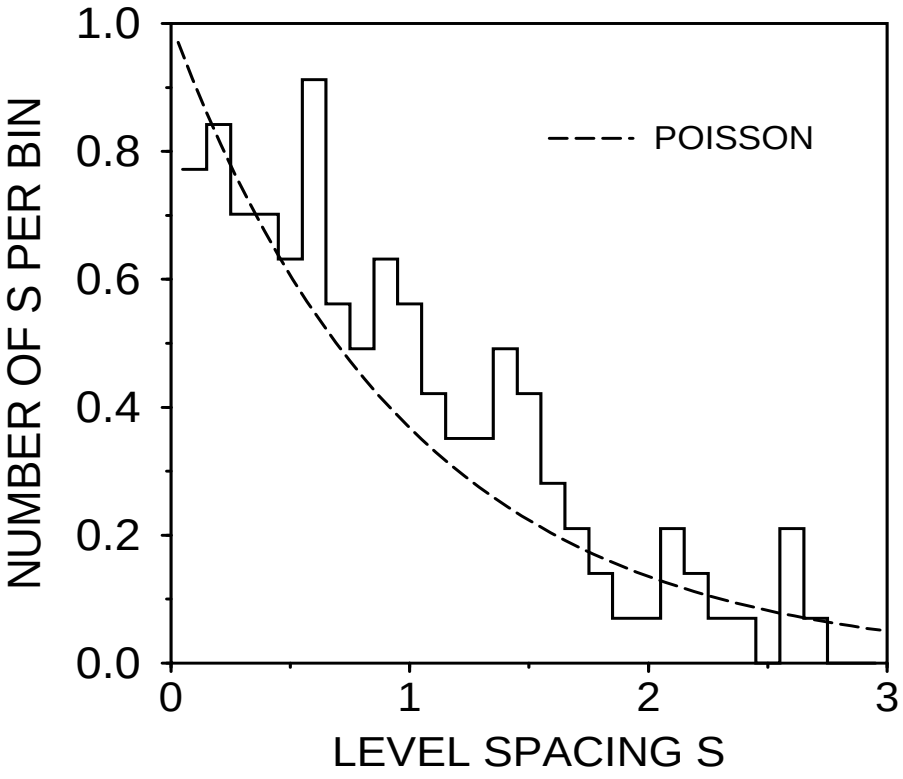

Figure 2.29: The level-spacing distribution for the 4096-atom-model locons with ω between 73 and 88 meV. The dashed line is the Poisson distribution ρ_P.

prediction is [54]

$$\begin{aligned}\Sigma_2^{GOE}(L) &= \frac{2}{\pi^2}\{\ln(2\pi L)+\gamma+1+\frac{1}{2}\left[Si(\pi L)\right]^2-\frac{\pi}{2}Si(\pi L)-\cos(2\pi L)\\ &- Ci(2\pi L)+\pi^2 L\left[1-\frac{2}{\pi}Si(2\pi L)\right]\},\end{aligned} \tag{2.28}$$

where $\gamma \approx 0.577$ is the Euler constant, and Si and Ci are the sine and cosine integrals. Figure 2.30 compares the calculated Σ_2 for diffusons with Σ_2^{GOE}. An agreement is up to about 10 level spacings L. At larger L the calculated values do not rise (as they would do according to RMT) but rather oscillate around an almost fixed value of 1. This indicates a failure of RMT. Similar observations have been made for ensembles of nuclear data [54] and the zeta function zeros [54]. A clear understanding of the failure is still lacking.

For the locons obeying the Poisson statistics one predicts $\Sigma_2^P(L)$ to be given simply as L (for uncorrelated levels in the interval of length L one expects to find $L \pm \sqrt{L}$ levels). A comparison of the Poisson distribution prediction with the calculation is in Fig. 2.31. Locons from 73 to 88 meV were analyzed. The maximum calculated L was 4 level spacings due to a small number of locons available. The agreement with the prediction is good, although the values of $\Sigma_2(L)$ are systematically lower than L. Finite size effects and small (on-shell) locon-locon overlap may account for this discrepancy.

More correlation functions remain to be computed before authoritative conclusions can be made. In any case, the above results indicate that diffusons are indeed describable (at least at short spectral scales) by RMT. Locons obey Poisson statistics.

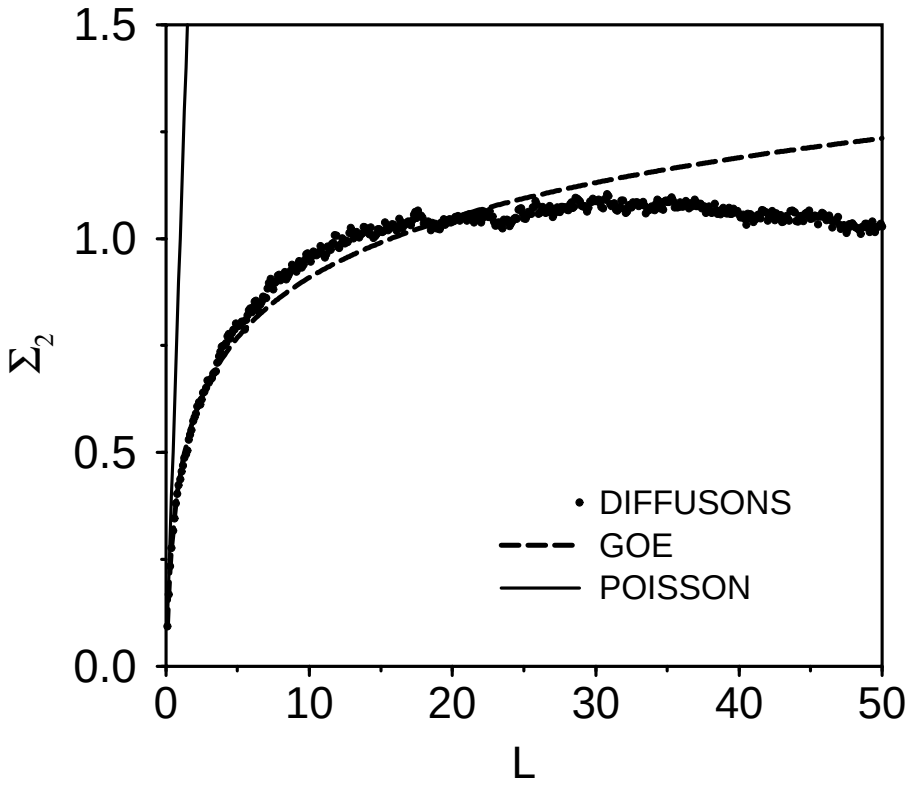

Figure 2.30: Calculated Σ_2 for the 4096-atom-model diffusons with ω between 45 and 65 meV. The dashed line is the GOE prediction Σ_2^{GOE} and the solid line is $\Sigma_2^P = L$ as predicted from the Poisson distribution.

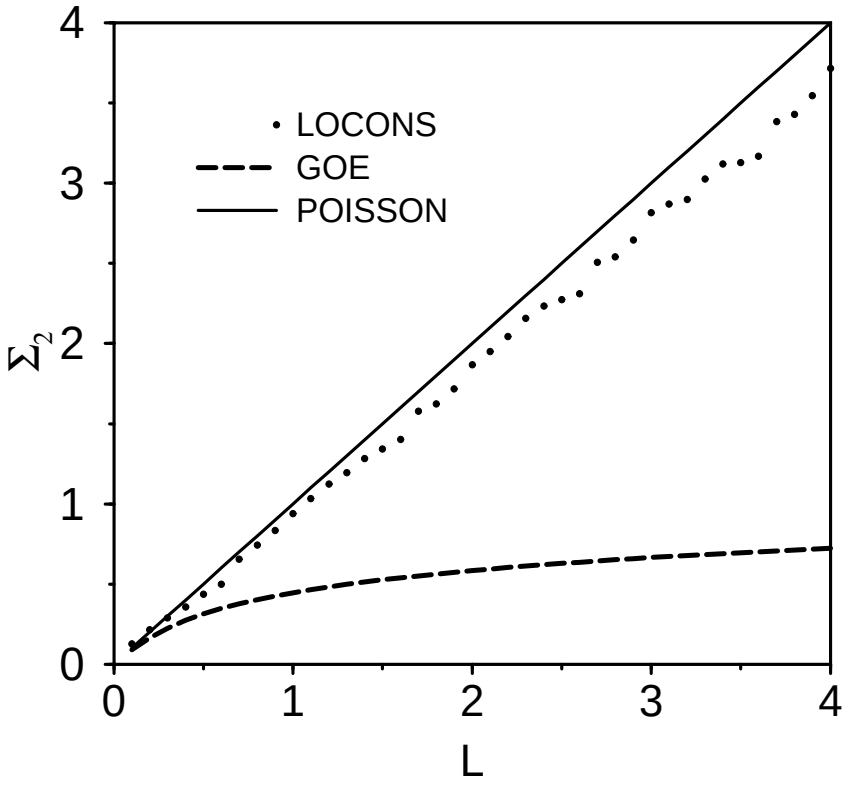

Figure 2.31: Calculated Σ_2 for the 4096-atom model locons with ω between 73 and 88 meV. The curve now resembles the Poisson-distribution prediction $\Sigma_2^P = L$.

2.6.2 Diffusivity and Sensitivity to Boundary Conditions [7]

In their work on diffusive transport of energy by vibrations in glasses, Allen and Feldman [7, 8] introduced the concept of *mode diffusivity* D_i, as

$$D_i = \frac{\pi V^2}{3\hbar^2 \omega_i^2} \sum_{j \neq i} |S_{ij}|^2 \, \delta(\omega_i - \omega_j). \tag{2.29}$$

Here S_{ij} is the heat current operator (see [7, 8] for details). In glasses the heat current operator has vanishing diagonal elements (the majority of vibrons are nonpropagating). The off-diagonal terms can carry heat since the thermal averaging of S_{ij} uses nonstationary states like wave packets, rather than vibrational eigenstates. The application of formula 2.29 to the WWW models of amorphous silicon with the SW interatomic potentials has lead to a successful explanation of the heat conductivity measurement. (Heat conductivity $\kappa = \sum_i C_i D_i$, where C_i is the mode specific heat.) In particular, the universally observed plateau at $T \approx 10$ K and subsequent rise of κ was explained using the above concepts and an assumption of tunneling modes.

In order to calculate diffusivity D_i according to Eq. 2.29, one needs to know the eigenmodes of the large system. However, it seems that there is another way to evaluate the mode diffusivities. Thouless, in connection with Anderson electronic localization, studied diffusivity of electrons in disordered media. The question was how to know whether a mode is localized or not. One way was to calculate conductivity at a given energy using the Kubo-

[7] J. Fabian and J. L. Feldman (unpublished).

Greenwood formula. If conductivity is zero, modes are localized. Thouless found a connection between conductivity and changes of eigenenergies when periodic boundary conditions are changed to antiperiodic. If, for a state i, the energy shift is $\Delta\epsilon_i$, the diffusivity is [55]

$$D_i = L^2 \Delta\epsilon_i / \hbar. \tag{2.30}$$

Equation 2.30 was derived from a Kubo formula. Does it also apply for vibrations in glasses (with $\epsilon_i = \hbar\omega_i$)? Since the heat current operator is different from the electrical current operator, the answer is not obvious. Figure 2.32 compares the Allen-Feldman calculation with the 1000-atom model and the calculation with the same model but with Eq. 2.30. Formula 2.29 involves the summation over spectral neighbors, while Eq. 2.30 involves only the mode in question. This might explain the large dispersion of the values of D_i calculated by using the Thouless method. The agreement between the two methods is very good, except at very low and middle frequencies.

The closeness of the two methods further supports the idea of intrinsic harmonic diffusivity of vibrons in glasses. Indeed, a qualitative way to see why Eq. 2.30 should hold is to consider wave packets superposed by modes of similar frequencies. In order for a wave packet to "feel" the boundary conditions, it has to spread out to the boundaries. The time it takes is D_i/L^2 and is connected to the energy uncertainty $\Delta\epsilon_i$ through Eq. 2.30.

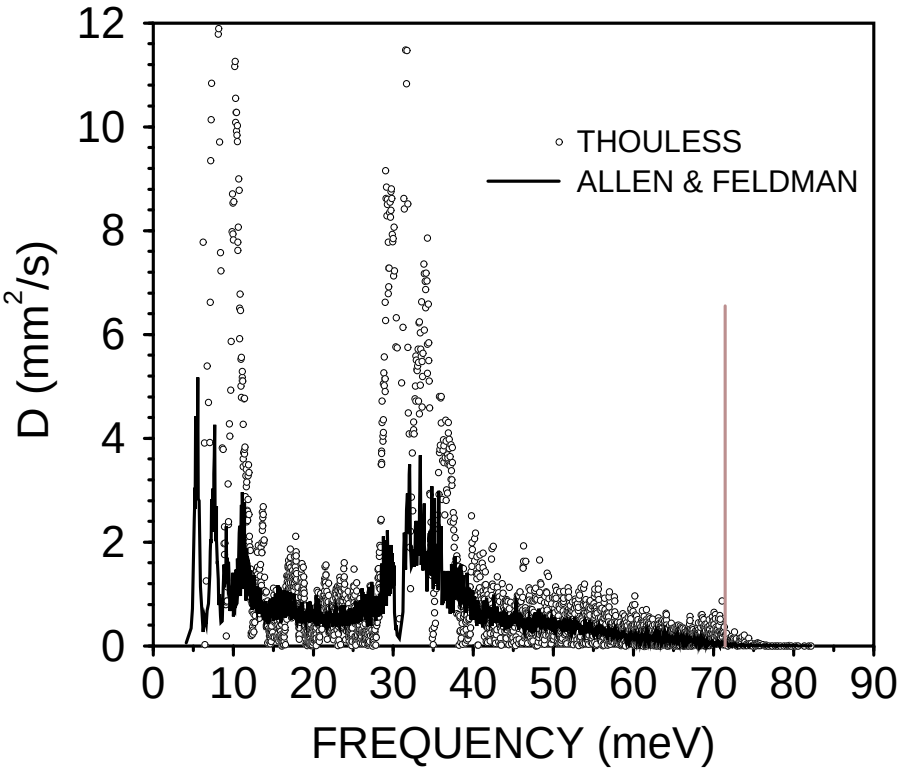

Figure 2.32: Mode diffusivity D_i of the 1000-atom model of amorphous silicon, calculated by using the method developed by Thouless (open circles) and the Allen-Feldman formula 2.29 (solid line).

2.6.3 Internal Friction and Sound Attenuation [8]

Introduction

Sound attenuation is arguably the least understood subject in glasses. This is because there are many competing factors that lead to sound wave damping. Most important are thermally activated relaxation, hypothetical tunneling states, topological defects, and thermal vibrations (in metals at low temperatures also conduction electrons). It is difficult to sort out different contributions for a given frequency and temperature range. In addition, if the attenuation is caused by interaction of sound waves with thermal vibrons, the corresponding physics depends on the quantity $\Omega\tau_{th}$, where Ω is the sound wave frequency and τ_{th} is the relaxation time of the thermal vibrons. For $\Omega\tau_{th} \ll 1$ (Akhiezer regime, [56, 57, 58])) the sound wave is attenuated by a dissipative process where a gas of vibrons tries to reach a local equilibrium characterized by a local (sound-wave given) strain. If $\Omega\tau_{th} \gg 1$ (Landau-Rumer regime, [56, 57, 58]), the attenuation is an elementary decay of the sound wave as a stationary mode of a corresponding harmonic lattice. Since the relaxation times in glasses are generally not known (see, however, Sec. 2.3), it is difficult to establish to which regime given data belong. Thermally activated relaxations are believed to dominate up to sound wave frequencies of order 1GHz. At higher frequencies thermal vibrons become more important. Recently Liu et al. [59] reported a discovery of a glass (amorphous silicon with 1 at. % H) without low energy excitations (like tunneling states). If this

[8] J. Fabian and P. B. Allen (unpublished).

would also imply inhibition of structural relaxations, such materials would be excellent to use for sorting out different contributions to sound attenuation.

The situation looks better on the experimental side. The most studied glass, silica (amorphous SiO_2), will serve as an example (sound attenuation in amorphous silicon has not been measured). The following observations are of interest here. (1) Zhu et al. [60] found a quadratic dependence of the attenuation coefficient on frequency from 76 to 440 GHz, and no significant temperature dependence from 80 to 300 K. Similar observations were found by Morath and Maris [61] for various polymers, except that the attenuation increased by a factor between two and three with increasing temperature. (2) Vacher et al. [62] subtracted the contributions of tunneling processes and thermally activated relaxations. The resulting attenuation, which should be mostly due to thermal vibrons, was still 2.5 times the observed attenuation in crystalline quartz. (3) Low temperature measurements are satisfactorily explained by the standard tunneling model [63].

Here we present a draft of a theory of the vibrational contribution to sound attenuation in glasses. Thermal vibrons attenuate sound via either thermal expansion or internal friction (viscosity). A longitudinal sound wave causes local contractions and dilations of density. Temperature changes accordingly and heat flows between regions of different temperatures. The wave is attenuated by energy dissipation during the heat transfer. Since thermal conductivity in glasses is much smaller than in crystals (while attenuation is greater), we do not expect this mechanism to be relevant. In addition, this way of energy dissipation is not present for transverse sound waves. In the following we

therefore concentrate on the internal friction mechanism. A sound wave can be considered as an adiabatic perturbation to the vibron system that leaves the occupation numbers of the vibrons unchanged. Vibrons suddenly find themselves in a nonequilibrium state characterized by old occupation numbers with new frequencies. It takes time of the order of the relaxation time τ_{th} for the vibrons to reach the new equilibrium. This new equilibrium always lags behind the sound wave and energy is dissipated. The condition $\Omega\tau \ll 1$ must hold for the vibrons to equilibrate before the sound wave completes its cycle. The Landau-Rumer regime $\Omega\tau \gg 1$ is more trivial, but cannot be explored by a finite model with $N \approx 1000$ due to the existence of a minimum frequency ω_{min} of the order of 1 THz.

In kinetic theory internal friction $\eta_{\alpha\beta\gamma\delta}(t)$ measures the response of the momentum flux density of a system to a homogeneous rate of change of strain $v_{\gamma\delta} = \frac{1}{2}(\partial_\delta \dot{u}_\gamma + \partial_\gamma \dot{u}_\delta)$. Linear response theory gives for the Fourier transformation

$$\eta_{\alpha\beta\gamma\delta}(\omega) = -\frac{1}{V\hbar\omega} Im\{D^R_{\alpha\beta\gamma\delta}(\omega)\}, \tag{2.31}$$

where $D^R_{\alpha\beta\gamma\delta}(\omega)$ is the Fourier transformation of the retarded momentum flux autocorrelation function. It can be expressed as an analytical continuation $D^R_{\alpha\beta\gamma\delta}(\omega) = \mathcal{D}_{\alpha\beta\gamma\delta}(i\nu_l)|_{i\nu_l=\omega+i0}$ of the Matsubara correlation function

$$\mathcal{D}_{\alpha\beta\gamma\delta}(i\nu_l) = -\int_0^{\hbar/k_BT} d\tau e^{i\nu_l\tau} \langle T_\tau(S_{\alpha\beta}(\tau)S_{\gamma\delta}(0))\rangle. \tag{2.32}$$

Here $S_{\alpha\beta}$ is the momentum flux operator (see below) and T_τ orders the operators according to imaginary time $i\tau$. The angle brackets denote averaging

over a canonical ensemble. Once the coefficient of internal friction is known, the sound attenuation coefficient Γ can be calculated:

$$\Gamma = \frac{\Omega^2}{\rho v_s^3} \sum_{\alpha\beta\gamma\delta} \eta_{\alpha\beta\gamma\delta} u_\alpha u_\gamma \frac{K_\beta K_\delta}{K^2}. \tag{2.33}$$

We denoted as v_s the sound velocity, ρ density, $\mathbf{u}$ unit polarization vector and $\mathbf{K}$ wave vector of the sound wave. The coefficient of internal friction is only weakly Ω dependent, so the Ω^2 dependence of Γ is characteristic for the Akhiezer regime. We note that η itself is a useful quantity that has been measured for many glasses (including amorphous silicon) [64, 65].

Momentum flux operator for a lattice

We need a microscopic expression for the momentum flux. Let a crystal have N unit cells each containing n atoms (a glass is a special case with $N = 1$ and n very large). Denote α-coordinates of positions and momenta of kth atom (with mass m_k) in the lth cell as $x_\alpha^k(l)$ and $p_\alpha^k(l)$, respectively. The local momentum conservation

$$\frac{\partial p_\alpha(\mathbf{x})}{\partial t} + \frac{\partial S_{\alpha\beta}(\mathbf{x})}{\partial x_\beta} = 0, \tag{2.34}$$

$$S_{\alpha\beta} = \int d^3x S_{\alpha\beta}(\mathbf{x}), \tag{2.35}$$

with the local momentum $p_\alpha(\mathbf{x}) = \sum_{kl} p_\alpha^k(l)\delta(\mathbf{x} - \mathbf{x}^k(l))$ current density, leads to the following choice for the momentum flux tensor $S_{\alpha\beta}$

$$S_{\alpha\beta} = \sum_{k,l} \left(\frac{p_\alpha^k(l) p_\beta^k(l)}{m_k} + \frac{1}{2} \left[x_\alpha^k(l) F_\beta^k(l) + x_\beta^k(l) F_\beta^k(l) \right] \right). \tag{2.36}$$

Here $\mathbf{F}^k(l)$ is the force acting on the atom at $\mathbf{x}^k(l)$. The flux is made explicitly symmetric. The first part in Eq. 2.36 is kinematic and corresponds to a

momentum transfer by the atomic motion itself. This carries nearly all the momentum in a gas, but very little in a solid. The second part is potential and represents a momentum transfer due to interatomic forces. This term carries essentially all the momentum in a solid (either crystalline or glassy).

The vibrational force up to the quadratic terms in the displacements $\mathbf{u}^k(l) = \mathbf{x}^k(l) - \bar{\mathbf{x}}^k(l)$, where $\bar{\mathbf{x}}^k(l)$ are equilibrium atomic coordinates, is

$$\begin{aligned} F^k_\alpha(l) &= \sum_\beta \sum_{k'} \sum_{l'} \Phi^{kk'}_{\alpha\beta}(ll') u^{k'}_\beta(l') \\ &+ \frac{1}{2} \sum_{\beta\gamma} \sum_{k'k''} \sum_{l'l''} \Phi^{kk'k''}_{\alpha\beta\gamma}(ll'l'') u^{k'}_\beta(l') u^{k''}_\gamma(l''). \end{aligned} \tag{2.37}$$

Here we substitute normal coordinates Q for the displacements $\mathbf{u}^k(l)$:

$$u^k_\alpha(l) = \frac{1}{\sqrt{N m_k}} \sum_{\mathbf{q}j} e^k_\alpha(\mathbf{q}j) e^{i\mathbf{q}\mathbf{R}(l)} Q_{\mathbf{q}j}, \tag{2.38}$$

where the sum is over wave vectors $\mathbf{q}$ from the first Brillouin zone (for glasses $\mathbf{q} \equiv 0$), and j is a band index from 1 to $3n$. Substituting the normal coordinates into Eq. 2.36 with the use of Eq. 2.37 one obtains the following for the momentum flux operator $S_{\alpha\beta} = S^1_{\alpha\beta} + S^2_{\alpha\beta}$:

$$S^1_{\alpha\beta} = \sum_{\mathbf{q}j} V^{(2)}_{\alpha\beta}(\mathbf{q}j) Q_{\mathbf{q}j}, \tag{2.39}$$

$$S^2_{\alpha\beta} = \frac{1}{2} \sum_{\mathbf{q}j, \mathbf{q}'j'} V^{(3)}_{\alpha\beta}(\mathbf{q}j, \mathbf{q}'j') Q_{\mathbf{q}j} Q_{\mathbf{q}'j'}. \tag{2.40}$$

The coefficients $V_{\alpha\beta\ldots}(\mathbf{q}j\ldots)$ can be deduced from the following example:

$$V^{(2)}_{\alpha\beta}(\mathbf{q}j) = \sum_{ll'} \sum_{kk'\gamma} \Phi^{kk'}_{\alpha\gamma}(ll') \bar{x}^k_\beta(l) \frac{e^{k'}_\gamma(\mathbf{q}j)}{\sqrt{N m_{k'}}} e^{i\mathbf{q}\cdot\mathbf{R}(l')}. \tag{2.41}$$

The pattern should be clear. (i) For each pair $\alpha\beta$ we sum over the atoms kl in the corresponding coefficient $\Phi^{(\ldots k\ldots)}_{\ldots\alpha\ldots}(\ldots l\ldots)$ multiplied by $\bar{x}^k_\beta(l)$. (ii) For

each mode $\mathbf{q}j$ we sum over atoms kl and coordinates γ in the corresponding coefficient $\Phi^{(\ldots k\ldots)}_{\ldots\gamma\ldots}(\ldots l\ldots)$ multiplied by $e^k_\gamma(\mathbf{q}j)\exp(i\mathbf{R}(l)\cdot\mathbf{q})/\sqrt{Nm_k}$. There are no numerical factors here. Moreover, there is the wavevector conservation "hidden" in the coefficients $V^{(i)}$. For instance, the $V_{\alpha\beta}(\mathbf{q}j)$ is nonzero only for $\mathbf{q}$ being a reciprocal lattice vector.

We will see below that the linear term $S^1_{\alpha\beta}$ has its origin in internal strain phenomenon (see Sec. 2.5).

Internal friction

Finally we evaluate the Matsubara correlation function $\mathcal{D}_{\alpha\beta\gamma\delta}(i\nu_l)$. Using perturbation theory one has to consider terms of the form

$$\langle T_\tau \left(S^1_{\alpha\beta}(\tau_1) S^1_{\gamma\delta}(\tau_2) H'(\tau_3) H'(\tau_4) \right) \rangle, \tag{2.42}$$

$$\langle T_\tau \left(S^1_{\alpha\beta}(\tau_1) S^2_{\gamma\delta}(\tau_2) H'(\tau_3) \right) \rangle, \tag{2.43}$$

$$\langle T_\tau \left(S^2_{\alpha\beta}(\tau_1) S^2_{\gamma\delta}(\tau_2) \right) \rangle, \tag{2.44}$$

contributing in Eq. 2.32 in the same order. Perturbation H' is the cubic term of an interatomic potential conveniently expressed in normal mode coordinates:

$$H' = \frac{1}{6} \sum_{\mathbf{q}\mathbf{q}'\mathbf{q}''} \sum_{jj'j''} V^{(3)}(\mathbf{q}j, \mathbf{q}'j', \mathbf{q}''j'') Q_{\mathbf{q}j} Q_{\mathbf{q}'j'} Q_{\mathbf{q}''j''}. \tag{2.45}$$

The evaluation is straightforward and the final formula (in the limit $\omega \ll \omega_i$) is

$$\eta_{\alpha\beta\gamma\delta} = \sum_{\mathbf{q}jj'} \gamma^{\alpha\beta}_{\mathbf{q}jj'} \gamma^{\gamma\delta}_{\mathbf{q}jj'} C_{\mathbf{q}j} T \delta(\omega_{\mathbf{q}j} - \omega_{\mathbf{q}j'}). \tag{2.46}$$

We denoted as $\gamma^{\alpha\beta}_{\mathbf{q}jj'}$ the generalized mode Gruüneisen parameters

$$\gamma^{\alpha\beta}_{\mathbf{q}jj'} = -\frac{1}{2\omega_{\mathbf{q}j}\omega_{\mathbf{q}j'}}\left[V^{(3)}_{\alpha\beta}(\mathbf{q}j,-\mathbf{q}j') - \sum_J \frac{V^{(2)}_{\alpha\beta}(\mathbf{0}J)}{\omega^2_{\mathbf{0}J}} V^{(3)}(\mathbf{q}j,-\mathbf{q}j',\mathbf{0}J)\right]. \quad (2.47)$$

When $j = j'$ this equation reduces to what is introduced in Sec. 2.5 as a measure of sensitivity of vibrational frequencies to volume changes. The second term in Eq. 2.47 has its origin in internal strain.

Surprising in Eq. 2.46 is the fact that dominant contribution to internal friction comes from diagonal elements ($j = j'$) even for glasses, where group velocity of the majority of modes is zero. Similar formula for heat conductivity [7] has diagonal elements that vanish for vanishing group velocity. Heat is then carried by off-diagonal elements. Here we see that momentum is carried by diagonal elements and momentum transfer is limited by anharmonic interactions that broaden the delta function in Eq. 2.46. Indeed, in order to use Eq. 2.46 in numerical calculations, one has to introduce finite relaxation times $\tau_{\mathbf{q}j}$ (as calculated for amorphous silicon in Sec. 2.3) instead of delta functions:

$$\eta_{\alpha\beta\gamma\delta} = \sum_{\mathbf{q}j} \gamma^{\alpha\beta}_{\mathbf{q}jj}\gamma^{\gamma\delta}_{\mathbf{q}jj} C_{\mathbf{q}j} T \tau_{\mathbf{q}j}. \quad (2.48)$$

This expression is in formal agreement with the result of kinetic theory of a phonon gas [66].

The numerical evaluation of Eq. 2.48 for our models of amorphous silicon is a task for the future.

Bibliography

[1] F. Wooten, K. Winer, and D. Weaire, Phys. Rev. Lett. **54**, 1392 (1985).

[2] F. H. Stillinger and T. A. Weber, Phys. Rev. B **31**, 5262 (1985).

[3] J. Q. Broughton and X. P. Li, Phys. Rev. B **35**, 9120 (1987).

[4] X. P. Li, G. Chen, P. B. Allen, and J. Q. Broughton, Phys. Rev. B **38**, 3331 (1988).

[5] J. L. Feldman, J. Q. Broughton, and F. Wooten, Phys. Rev. B **43**, 2152 (1991).

[6] A. F. Ioffe and A. R. Regel, Prog. Semicond. **4**, 237 (1960).

[7] P. B. Allen and J. L. Feldman, Phys. Rev. Lett. **62**, 645 (1989); P. B. Allen and J. L. Feldman, Phys. Rev. B **48**, 12 581 (1993).

[8] J. L. Feldman, M. Kluge, P. B. Allen, and F. Wooten, Phys. Rev. B **48**, 12 589 (1993).

[9] P. Sheng and M. Y. Zhou, Science **253**, 539 (1991); P. Sheng, M. Zhou, and Z. Zhang, Phys. Rev. Lett. **72**, 234 (1994).

[10] S. Alexander, C. Laermans, R. Orbach, and H. M. Rosenberg, Phys. Rev. B **28**, 4615 (1983); A. Jagannathan, R. Orbach, and O. Entin-Wohlman, Phys. Rev. B **39**, 13 465 (1989); R. Orbach, Phil. Mag. B **65**, 289 (1992); R. Orbach and A. Jagannathan, J. Phys. Chem. **98**, 7411 (1994).

[11] A. J. Scholten and J. I. Dijkhuis, Phys. Rev. B **53**, 3837 (1996).

[12] A. J. Scholten, A. V. Akimov, and J. I. Dijkhuis, Phys. Rev. B **47**, 13 910 (1993); A. J. Scholten, A. V. Akimov, P. A. W. E. Verleg, J. I. Dijkhuis, and R. S. Meltzer, J. Non-Cryst. Sol. **164-166**, 923 (1993).

[13] J. L. Feldman, S. R. Bickham, G. E. Engel, and B. N. Davidson (unpublished).

[14] S. Kugler, L. Pusztai, L. Rosta, P. Chieux, and R. Bellissent, Phys. Rev. B **48**, 7685 (1993).

[15] P. W. Anderson, Phys. Rev. **109**, 1492 (1958).

[16] J. Hafner and M. Krajci, J. Phys. : Condens. Matter **6**, 4631 (1994).

[17] H. R. Schober and B. Liard, Phys. Rev. B **44**, 6746 (1991); H. R. Schober and C. Oligschleger, Phys. Rev. B **53**, 11 469 (1996).

[18] Yu. Kagan and Ya. A. Iosilevskii, JETP **15**, 182 (1962).

[19] R. Brout and W. Visscher, Phys. Rev. Lett. **9**, 54 (1962).

[20] S. Takeno, Prog. Theor. Phys. **29**, 191 (1963).

[21] R. J. Bell and D. C. Hibbins-Butler, J. Phys. C **8**, 787 (1975).

[22] Yu. M. Galperin, V. G. Karpov, and V. I. Kozub, Adv. Phys. **38**, 669 (1989), and references therein.

[23] A. A. Maradudin and A. E. Fein, Phys. Rev. **128**, 2589 (1962); R. A. Cowley, Adv. Phys. **12**, 421 (1963).

[24] J. Menéndez and M. Cardona, Phys. Rev. B **29**, 2051 (1984).

[25] S. Narasimhan and D. Vanderbilt, Phys. Rev. B **43**, 4541 (1991).

[26] A. Debernardi, S. Baroni, and E. Molinari, Phys. Rev. Lett. **75**, 1819 (1995).

[27] J. Fabian and P. B. Allen, Phys. Rev. Lett. **77**, 3839 (1996).

[28] V. Ambegaokar, B. I. Halperin, and J. S. Langer, Phys. Rev. B **4**, 2612 (1971).

[29] E. H. Lieb and D. C. Mattis, *Mathematical Physics in One Dimension* (Academic Press, New York, 1966).

[30] J. Kori, *Spectral Properties of Disordered Chains and Lattices* (Pergamon, New York, 1981); S. Alexander, J. Bernasconi, R. Orbach, and W. R. Schneider, Rev. Mod. Phys. **53**, 175 (1981).

[31] Mott N. F. and W. D. Twose, Adv. Phys. **10**, 107 (1961).

[32] P. B. Allen, J. Kelner, and J. Fabian (unpublished).

[33] M. Ya. Azbel, Phys. Rev. B **27**, 3901 (1983); *ibid.* **28**, 4106 (1983).

[34] J. T. Edwards and D. J. Thouless, J. Phys. C **5**, 807 (1972).

[35] T. H. K. Barron, J. G. Collins, and G. K. White, Adv. Phys. **29**, 609 (1980).

[36] Yu. M. Galperin, V. L. Gurevich, and D. A. Parshin, Phys. Rev. B **32**, 6873 (1985).

[37] G. K. White, Phys. Rev. Lett. **34**, 204 (1975); K. G. Lyon, G. L. Salinger, and C. A. Swenson, Phys. Rev. B **19**, 4231 (1979); G. J. Morgan, G. K. White, and J. G. Collins, Phil. Mag. B **43**, 1039 (1981); D. A. Ackerman, A. C. Anderson, E. J. Cotts, J. N. Dobbs, W. M. MacDonald, and F. J. Walker, Phys. Rev. B **29**, 966 (1984); G. K. White, S. J. Collocott, and J. S. Cook, Phys. Rev. B **29**, 4778 (1984); G. A. Saunders, R. D. Metcalfe, M. Cutroni, M. Frederico, and A. Piccolo, Phys. Rev. B **53**, 5287 (1996)

[38] A. Witvrouw and F. Spaepen, J. Appl. Phys. **74**, 7154 (1993).

[39] G. Dolling and R. A. Cowley, Proc. Phys. Soc. **88**, 463 (1966).

[40] R. Vacher, J. Pelous, F. Plicque, and A. Zarembowitch, J. Non-Crys. Sol. **45**, 397 (1981); C. J. Morath and H. J. Maris, Phys. Rev. B **54**, 203 (1996); B. E. White and R. O. Pohl, Z. Phys. B **100**, 401 (1996).

[41] J. Fabian and P. B. Allen (unpublished).

[42] T. H. K. Barron and M. L. Klein, in *Dynamical Properties of Solids*, edited by G. K. Horton and A. A. Maradudin (North-Holland, Amsterdam, 1974) Vol. I, p. 391.

[43] A. A. Maradudin, E. W. Montroll, G. H. Weiss, and I. P. Ipatova, *Theory of Lattice Dynamics in the Harmonic Approximation*, Solid State Physics, Supplement 3 (Academic Press, New York, 1971).

[44] R. E. Cowley, Phys. Rev. Lett. **60**, 2379 (1988).

[45] H. Ibach, Phys. Stat. Sol. **31**, 625 (1969); G. A. Slack and S. F. Bartram, J. Appl. Phys. **46**, 89 (1975).

[46] S. Biernacki and M. Scheffler, Phys. Rev. Lett. **63**, 290 (1989); C. Z. Wang, C. T. Chan, and K. M. Ho, Phys. Rev. B **42**, 11 276 (1990); G. K. White, Contemp. Phys. **34**, 193 (1993).

[47] G. K. White, J. Phys. D **6**, 2070 (1973).

[48] M. Marinov and N. Zotov, Phys. Rev. B **55**, 2938 (1997).

[49] R. Biswas, A. M. Bouchard, W. A. Kamikatahara, G. S. Grest, and C. M. Soukolis, Phys. Rev. Lett. **60**, 2280 (1988).

[50] J. Fabian, J. L. Feldman, and P. B. Allen (unpublished).

[51] B. I. Shklovskii, B. Shapiro, B. R. Sears, P. Lambrianides, and H. B. Shore, Phys. Rev. Lett. **47**, 11 487 (1993); V. E. Kravtsov, I. V. Lerner, B. L. Altshuler, and A. G. Aronov, Phys. Rev. Lett. **72** 888 (1994); K. Müller, B. Mehlig, F. Milde, and M. Schreiber, Phys. Rev. Lett. **78**, 215 (1997).

[52] R. Kühn and U. Horstmann, Phys. Rev. Lett. **78**, 4067 (1997).

[53] T. A. Brody, J. Flores, J. B. French, P. A. Mello, A. Pandey, and S. S. M. Wong, Rev. Mod. Phys. **53**, 385 (1981).

[54] M. L. Mehta, *Random Matrices* (Academic Press, New York, 1991).

[55] D. J. Thouless, in *Ill-Condensed Matter*, edited by R. Balian, R. Maynard, and G. Toulouse (North-Holland, Amsterdam, 1979).

[56] H. E. Bömmel and K. Dransfeld, Phys. Rev. **117**, 1245 (1960).

[57] T. O. Woodruff and H. Ehrenreich, Phys. Rev. **123**, 1553 (1961).

[58] H. Maris, in *Physical Acoustics*, vol. VIII, edited by W. P. Mason and R. N. Thurston, (Academic Press, New York, 1971).

[59] X. Liu, B. E. White, R. O. Pohl, E. Iwanizcko, K. M. Jones, A. H. Mahan, B. N. Nelson, R. S. Crandall, and S. Veprek, Phys. Rev. Lett. **78**, 4418 (1997).

[60] T. C. Zhu, H. J. Maris, and J. Tauc, Phys. Rev. B **44**, 4281 (1991); H.-N. Lin, R. J. Stoner, H. J. Maris, and J. Tauc, J. Appl. Phys. **69**, 3816 (1991).

[61] C. J. Morath and H. J. Maris, Phys. Rev. B **54**, 203 (1996).

[62] R. Vacher, J. Pelous, F. Plicque, and A. Zarembovitch, J. Non-Crysitalline Solids **45**, 397 (1981).

[63] S. Hunklinger and W. Arnold, in *Physical Acoustics*, vol XII, edited by W. P. Mason and R. N. Thurston (Academic Press, New York, 1976).

[64] K. A. Topp and D. G. Cahill, Z. Physik B **101**, 235 (1996).

[65] B. E. White and R. O. Pohl, Z. Phys. B **100**, 401 (1996).

[66] E. M. Lifshitz and L. P. Pitaevskii, *Physical Kinetics* (Pergamon, New York, 1981).